LIGERS INTERFEROMETRIC SURVEY OF M DWARF DIAMETERS

A Dissertation

Submitted to the Graduate Faculty of the
Louisiana State University and
Agricultural and Mechanical College
in partial fulfillment of the
requirements for the degree of
Doctor of Philosophy

in

The Department of Physics and Astronomy

by
Tyler Gregory Ellis
A.A. Spokane Falls Community College, 2011
B.S. University of Wyoming, 2015
August 2022

This dissertation is dedicated to my late grandmother Judith. Thank you for answering my phone calls and for all of the almond roca. I wish I could have shared finishing this challenge with you.

The reward for digging holes is a bigger shovel.
–Terry Pratchett
I Shall Wear Midnight

Acknowledgements

Science is inherently a community endeavor — the citations in this thesis with 100+ authors go to show that! This goes beyond the collaborations we work in. Behind every scientist are friends and colleagues propping them up. Without a doubt, I would not be writing these words down if it weren't for the assistance, guidance, pushing, shoving, loving and caring from my family, friends, and colleagues.

To my family, Schooner, Robert, Karla, Derek, Mark, Pam, and Judith thank you for keeping me sane and encouraging me along. Thank you for answering the phone and video chats, the care packages, weekend pirates, dwarves, eldritch monsters, and all the precious coffee. I don't know what the future holds, but I am confident and happy to brave it with you.

I would like to offer my most sincere gratitude to my supportive and nigh omniscient advisor Tabetha Boyajian. We started together studying a star doing a weird thing and are wrapping things up here studying weird things being done about stars — a humorous bookend, if you ask me. I will remember our research trips, Pokémon hunting, group pottery nights, and your absolute insistence I mind my mental and physical well-being.

Without my friends, I would be a much duller and sadder person. Thank you Aaron (times two), Ali, Allie, Brad, Eklavya, Courtney, Graeme, John/Ross, Karunya, LeAnne, Liz/Syrissa, Luke, Rachel, Rachael, Sam, Shannon, Sudarsan, Thomas, Tim, and Vishal. To Stardew, video game soundtracks, vegan ciabatta, Divinity, Steven Universe, Fortran, French teachers, D&D, Iowa pit stops, dancing puppets, tech support, trips to the Walmart for tea, and hummus!

Finally, to those who helped me along just doing their job with candor and care. To our dear collaborators Andrew Mann and Kaspar von Braun, thank you for your spectra, beer, and guidance. To the CHARA scientists and staff, I could not be here if it were not for your decades of dedication and late nights. Thank you Gail, Theo, Norm, Olli, Chris, Jeremy, Matt, and Stella. I offer my appreciation to the faculty and staff in the Department of Physics and Astronomy and the Louisiana State University. I want to thank Carol, Claire, Mimi, Shemeka, Arnell, and Paige. Nothing would move in the department without your efforts. I give thanks to the authors who've lately made me turn pages, laugh, think, and feel, Le Guin, Roach, Gaiman, and Pratchett.

I think that's about it. Now, let's get to work.

Table of Contents

Acknowledgements v

Abstract xi

1 The LIGERS Survey Overview 1

2 Light, Interference, and Interferometry 3
2.1 Resolution and the Need for Long Baseline Optical Interferometers 3
2.2 Quantum Nature of Light 4
2.3 Interferometric Observables and the Relation to Stellar Diameter 8

3 Astronomical Interferometers 12
3.1 A Few Historically Significant Interferometers 12
3.2 The CHARA Array 13

4 HD 97658: A Prelude to the Survey 16
4.1 Introduction 16
4.2 Interferometric Observations 17
4.3 Directly Determined Stellar Properties 20
4.4 Derived Stellar and Planetary Properties 22

5 LIGERS Survey Methods 31
5.1 Observational Methods 31
5.2 Data Reduction and Calibration 32

6 LIGERS Survey Results 35
6.1 Angular Diameter Fitting 35
6.2 An Anomalous Detection 39
6.3 Applications of Measured M Dwarf Diameters 42

7 Surface Brightness Relations 48
7.1 Introduction 48
7.2 Results 50

8 Conclusion 63

A Summary of Baselines Available at the CHARA Array 64

B LIGERS Survey Observation Log and Calibrator Stars 65

C Copyright Information 69

D Stellar Properties of Literature Stars 71

E Surface Brightness Relation Data 72

Works Cited 75

Vita 85

List of Tables

4.1 HD 97658 Observing Log 19
4.2 Calibrators Used with HD 97658 19
4.3 Summarized Properties of the HD 97658 System 30
6.1 Summary of Survey Results 38
7.1 Summary of Photometric Filters 51
7.2 Coefficients to Polynomial Surface Brightness Relations 56
A.1 CHARA Array Baselines 64
B.1 Observation Log 65
B.3 Summary of Calibrator Properties 67
D.1 Summary of Stellar Properties for Literature Stars 71
E.1 Surface Brightness Photometry 73

List of Figures

2.1 Young Two-Slit Experiment 5

2.2 The Michelson Interferometer 6

2.3 A Simplified Astronomical Interferometer 7

2.4 Brightness Distributions and Their Fourier Pairs 10

4.1 Visibility Curve of HD 97658 22

4.2 Spectral Energy Distribution of HD 97658 23

4.3 HD 97658 Isochrone Posterior Distributions 25

4.4 HD 97658 TESS High Cadence Lightcurve 26

4.5 HD 97658 TESS Box Least-Squares Periodogram 27

4.6 HD 97658 TESS Phase-Folded Lightcurve 28

5.1 Comparison of Visibility Estimators 33

6.1 Visibility Curves of Surveyed Stars 37

6.2 LIGERS Stars Comparison 40

6.3 A Sample Binary Star Visibility Curve 41

6.4 Visibility Curve of GJ 49 and GJ 169, Suspected Binary Stars 42

6.5 MIST HR-Diagram 44

6.6 Parsec HR-Diagram 45

6.7 YaPSI HR-Diagram 46

6.8 Solar Iron Abundance Isochrone Comparison 47

7.1 Surface Brightness Relation - V Reference Mag 53

7.2 Surface Brightness Relation - R_C Reference Mag 54

7.3 Surface Brightness Relation - G Reference Mag 55

7.4 $(V - I_C)$ Model Comparison 58

7.5 $(V - J)$ Model Comparison 59

7.6 $(V - H)$ Model Comparison 60

7.7 $(V - K_S)$ Model Comparison 61

7.8 Comparison of Surface Brightness Relations for Dwarfs and Giants 62

Abstract

In this thesis, I present the largest single collection of M dwarf stellar radii in over a decade and contextualize these measurements with the systematic model discrepancies. The measurements of stellar angular diameters are also important in the quantification of the properties of exoplanets. In order to estimate the property of the exoplanet, it is first necessary to quantify the properties of the planet's host star. Using the survey results complemented with previous direct observations of the angular diameters of low mass stars, I develop updated updated surface brightness relationships. These relationships allow predictions of angular diameters using easy to obtain photometry.

Chapter 1.
The LIGERS Survey Overview

There is a problem with current evolutionary models of low mass stars: the models overestimate the radius of the stars by about 5% [18, 113]. The radius of a star is one of its most basic parameters and influences estimations of other parameters such as the temperature and habitability of planetary companions. The issue with the evolutionary models in part arises from the relative lack of high accuracy stellar radii to benchmark evolutionary models. Stellar radii are difficult to measure as all stars outside of the solar system cannot be resolved by standard ground based observatories and only a select few can be resolved by space telescopes. Contrarily, other properties of a star such as its luminosity is readily measurable at the percent level of accuracy.

One of the reasons the evolutionary models may fail to predict the stellar radius accurately is due to oversimplifications of the energy transport from the core of the star out through the stellar atmosphere. This is especially problematic for low mass stars which have convective regions reaching nearly, if not entirely, to their core. The whole of a star's life is the interplay of inward gravitational pressure versus outward forces in a delicate balance of hydrostatic equilibrium.

The issue at play here is that the magnetic force affects the efficiency of convection inside the star. Though a full theoretical framework of magnetic fields and diffusion in stellar interiors is not available, there are several treatments which show magnetic fields can have an appreciable effect on convective energy transport. If convection is impeded, more of the fusion energy must be transported outward by radiation instead, which has the consequence of lowering the effective temperature of the star [42, 24]. As the star's luminosity is unchanged, the radius of the star increases to compensate. The results of this survey will allow constraining evolutionary models for the smallest and strongly magnetically active stars.

In this survey, I measured the diameters of a 14 new low mass stars. Low mass is broken into two categories: the K stars, which have masses between ~ 0.5–0.8 $M_\odot$ and the M stars, which have masses between ~ 0.1–0.5 $M_\odot$. This thesis focuses on the M dwarfs, but future works will expand the survey sample into K dwarfs as well.

I measure the stellar angular diameters using the Georgia State University Center for High Angular Resolution Astronomy (CHARA) Array. The CHARA Array is an astronomical interferometer which is capable of measuring angular diameters down to 0.2 milli-arcseconds (mas), which is much smaller than the resolution limit of standard space or ground based telescopes. I pair these observations of angular diameters with Gaia parallaxes to compute the physical diameters of the stars [44]. This survey of angular diameters has been titled the LSU Interferometry Group for Excellent Radii Survey (LIGERS). The full catalog of observed targets is in Table 6.1.

With the diameter measurements from this survey and literature photometry measurements, I have updated surface brightness relationships for M dwarfs. Surface brightness relations are a tool for estimating angular diameter using only photometric magnitudes of stars. As colors are unique to stars based on their mass and age, surface brightness relationships allow easy estimation of stellar sizes for distant and faint targets.

As part of the survey, we studied a special exoplanet host star HD 97658. This star is

orbited by a super-Earth planet, a type of planet not present in our Solar System. Our study of the host star allowed us to characterize the fundamental properties of the planet. Interferometry has given much to the field of exoplanet science throughout its history. Our study of HD 97658 is another example of how the measurement of the fundamental properties of stars influences many sub-fields of astronomy.

In § 2, I introduce the resolution power of telescopes and the need for high resolution observations. I also describe the historical development of a quantum theory of light and interferometry. In § 3, I give an overview of historically significant developments in interferometry and astronomical interferometers. In § 4 and its subsections, I have reproduced an original work on fitting the diameter of HD 97658, a testbed for the fitting procedure used in the LIGERS survey. In § 5, I describe the methods used for the interferometric observations and data analysis. In § 6, I show and discuss the results of the LIGERS survey. In § 7, I derive and fit surface brightness relations to an extended sample of M dwarfs and compare to previous results. Finally, in § 8, I conclude the LIGERS survey and the results of this thesis.

Chapter 2.
Light, Interference, and Interferometry

2.1 Resolution and the Need for Long Baseline Optical Interferometers

The radius of a star is one of its most intrinsic parameters and is also one of the most difficult to quantitatively measure. This is because even though stars can grow quite large, space is unfathomably larger. The vast divide in the relative sizes of stars and the space is apparent in our local neighborhood. The Sun is approximately 100 times the size of the Earth, but the Solar System is 6,500 times the size of the Sun. The effect is that to all standard telescopes, stars appear as point sources. Taking a picture of even the closest star to Earth, Proxima Centauri with a radius of 0.15 $R_\odot$ located 4.2 ly away, is equivalent to taking a picture of a grain of salt in New Orleans from the Baton Rouge.

Astronomical interferometry produces images and measurements at resolutions which are technically, financially, and practically impossible to achieve otherwise. The resolution of a telescope is its ability to produce fine details in the images taken with it. Resolution is a highly desirable quality in astronomy that may be confused with image size. Computers can change the dimension of an image easily by stretching and scaling, but it does not suffice to zoom in on an image to find a stellar diameter. Zooming as a process does not reveal any extra information about the target. Another analog from technology which readily demonstrates the desire for the highest resolution is development of 4K and 8K resolution screens. Though the size of the screen is changeable, the level of detail the screens show is fixed at manufacturing.

Likewise, the finest detail that a telescope can reveal remains fixed at the time that it is manufactured. The resolution of a telescope, which is represented with the symbol θ, depends on two factors: the wavelength, or color, of the light observed λ and the diameter of the telescope D:

$$\theta = 1.22 \cdot \frac{\lambda}{\mathrm{D}} \tag{2.1}$$

This expression is called the diffraction limit or the Rayleigh criterion. The diffraction limit of the telescope given by the Rayleigh criterion has better physical interpretation when expressed in degrees, or more commonly subdivisions of a degree called an arcsecond, which is $\frac{1}{3600}^{\text{th}}$ of a degree and is given the symbol $''$.

Applying Eq. 2.1 to a 20 cm amateur telescope looking in visible light, $\lambda = 650$ nm, has a resolution of $0.8''$. Taken at first glance, this is an impressive number, but considering that the star with one of the largest angular diameters aside from the sun, Betelgeuse, has an angular diameter of $0.04''$. Even worse, this limit is not truly reflective of the resolution power of that telescope, as the atmosphere smears out the image. The quality and behavior of the atmosphere is referred to as the seeing and limits the telescope's resolution in average conditions to 1–$2''$. These constraints demand a different approach to resolve the angular diameters of stars.

Astronomical interferometry is an observational technique which utilizes the wave nature of light to achieve greater resolution than the standard telescopes which comprise the interferometer. Interferometry allows us to overcome the diffraction and seeing limitations. This technique uses the light from two or more telescopes to achieve resolutions that cannot be

obtained by standard ground based observatories.

2.2 Quantum Nature of Light

In order to discuss astronomical interferometry and the design of interferometers, or most of all astronomical observing, it is necessary to have some understanding of the nature of light. Light, or electromagnetic radiation, can be approached in two ways: as a particle or as a wave. It is convenient to treat light as a particle streaming through space when observing with a normal telescope and camera. It is easy to imagine a particle zipping through the space and into telescope and landing on the camera. However, the simplicity of the particle theory fails to explain many phenomena of light. Most importantly for this work, it fails to explain interference.

Interference is an interaction where two waves are superposed changing the amplitude of the combined wave. The wave's amplitude has a simple physical interpretation: for standing waves, such as waves on water it is just the height; for light waves it is the amplitude of the electric field which oscillates. In order for the waves to combine and increase the amplitude, which is called constructive interference, the waves must be in phase. In phase means the electric fields are spatially oriented such that their peaks are aligned. Deconstructive interference is the opposite and occurs when the peaks of one wave are aligned with the troughs of another, cancelling each other out.

Thomas Young demonstrated the wave nature of light in the early 1800s with his quintessential two-slit experiment. A light source illuminates a screen, which has two rectangular slits cut into it, and the light from the slits falls on the background. As per the particle theory of light, it is expected two rectangular beams would emerge onto the background. Rather, when the light emerges from the slits, it interferes with itself and forms a fringe pattern on the background. The two-slit experiment and resultant fringe pattern are shown in Figure 2.1.

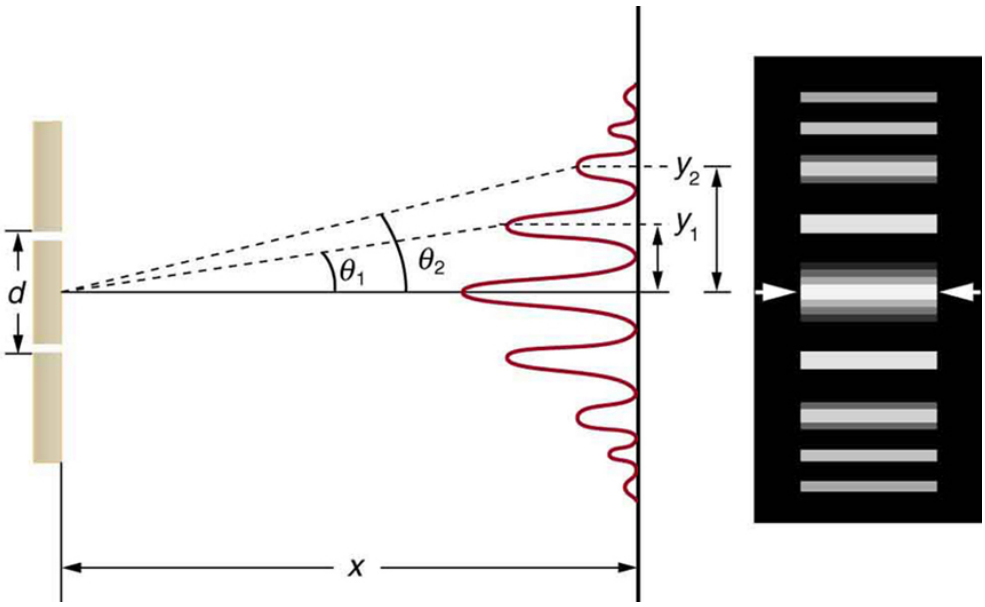

Figure 2.1. The Young Two-Slit experiment demonstrates the necessity to treat light as a wave. Coherent light travels from left to right and encounters the two slits. Two spherical waves are created at the slits and propagate to the screen. The observed power of the fringe packet made by the resultant combination of the two spherical waves is shown as the red line. A detector integrating the power of the fringes placed where the screen is would see the pattern on the right. The angular separation between the central peak and further peaks depends on the wavelength of the light and the separation of the slit, as shown in Eq. 2.11. See § 2.3 for more details on phase and optical path equalization. This figure has been accessed from the the OpenStax free textbook and is licensed under the Creative Commons v. 4 license.

A similar experiment demonstrating the interference of light is the Michelson interferometer, which bears the name of one of the fathers of astronomical interferometry: Albert Michelson. A schematic of a Michelson interferometer is shown in Figure 2.2.

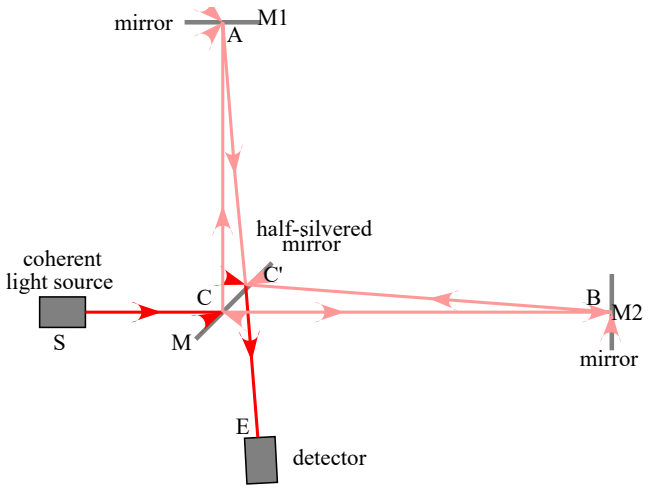

Figure 2.2. A Michelson interferometer. Light from a coherent source on the left travels to the right and encounters a partially transparent mirror. Some of the light is reflected up and the remainder is transmitted through the mirror. Both partitions of the light encounter another mirror and are reflected back to the splitting mirror. The orientation of the mirror causes the two beams to recombine at a detector at the bottom; however, the beams are now out of phase. This produces an interference fringe pattern on the detector. This figure has been accessed from the English Wikipedia page for the Michelson Interferometer and is used under the Creative Commons (CC) by SA license with the following attribution: Michelson Interferometer.svg: User:Krishnavedala [CC BY-SA 4.0 (`http://creativecommons.org/licenses/by-sa/4.0/`)]

The fundamental design of the Georgia State University Center for High Angular Resolution Astronomy Array is similar to that of the Michelson interferometer and the two slit experiment, with a few modifications. First, the slits need to be replaced with telescopes. Second, the separation between the slits is replaced with the separation between the telescopes. Third, and last, the path length traveled by either wave must be adjustable such that the total path length for both waves is equal. These changes are all present in the simplified diagram of CHARA Array as shown in Figure 2.3.

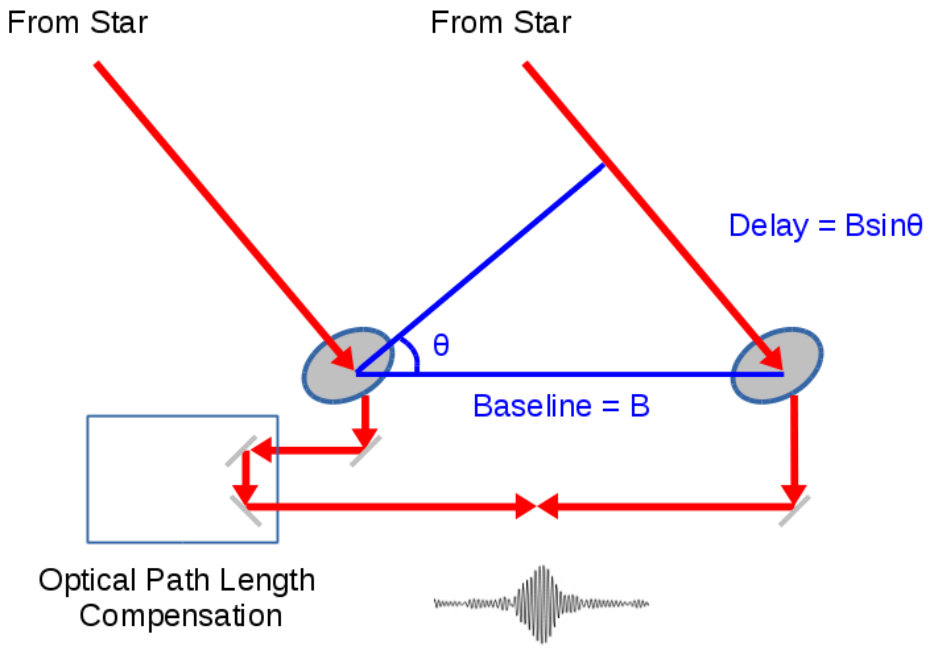

Figure 2.3. A simplified schematic of a typical astronomical interferometer. Two, or more, telescopes collect light from a star. These telescopes have a separation, or baseline, on the ground of B. However, relative to the sky, the telescopes are separated by $B \sin\theta$, the projected baseline. The light from the two telescopes must have their light travel distance, the optical path length, equalized before combination. The combination produces a fringe packet as shown at the bottom. This image was accessed from the CHARA website and is available at `http://www.chara.gsu.edu/public/basics-of-interferometry`.

The astronomical interferometer allows observations at extremely small angular resolutions. Whereas the resolution of a typical ground based observatory is restricted by the atmosphere, an interferometer avoids atmospheric smearing by using information encoded in the resulting fringes when the telescopes' light is combined. The resolution of the interferometer is shown in Figure 2.1 as the angular separation of the fringe packets. The distance between the screen differs for each slit at all points. Where the difference is equal to an integer number of the wavelength of the light the light from the two slits constructively interfere. By requiring that the optical path difference puts the two waves one wavelength out phase, it is a matter of geometry to show that the resulting angular separation depends only on the wavelength and separation between the slits:

$$\theta = \frac{\lambda}{2B} \tag{2.2}$$

Using the longest baseline that CHARA can provide at visible wavelengths gives a limiting resolution of approximately 0.0002 ″or 0.2 mas (milli-arcseconds). This beats the diffraction limit of the Hubble Space Telescope by a factor of about 300. An interesting peculiarity of the limit on the interferometer is that it does not depend on the size of the telescopes used, but

only on the wavelength of observed light and separation of the telescopes. Contrarily, for a standard telescope, improvements in resolution demand an increase in the size of the primary optic. A refracting telescope rapidly becomes too large and too expensive to manufacture lenses, and a reflecting telescope will bend under the weight of a massive single mirror.

2.3 Interferometric Observables and the Relation to Stellar Diameter

Even amongst astronomers, interferometry has an air of obtuseness that is worth demystifying. The following derivation of interferometric fringe patterns largely summarizes Hanbury Brown et al. [54] and the review article Lawson [75]. First, I will derive the interferometric visibilites, which is the quantity measured by the interferometer. Then, I will discuss its relationship to physical parameters.

Considering only a monochromatic source which is observed by a two telescope interferometer, the electric field of the light at the first telescopes as a function of time is:

$$\psi_1 \sim e^{i\mathbf{k}\cdot\mathbf{x}_1 - i\omega t} \tag{2.3}$$

Where $\mathbf{k}$ is the wavevector, which describes the propogation direction and wavelength, $\mathbf{x}_1$ is the spatial coordinate of the first telescope, and ω is the frequency of the wave. The baseline can be expressed as $\mathbf{B} = \mathbf{x}_2 - \mathbf{x}_1$. This allows expressing the second wave without the second spatial coordinate:

$$\psi_2 \sim e^{i\mathbf{k}\cdot\mathbf{x}_2 - i\omega t} = e^{i\mathbf{k}\cdot(\mathbf{B}+\mathbf{x}_1) - i\omega t} \tag{2.4}$$

It is possible to rewrite these two waves in terms of only the magnitude of the wavevector, k, and the direction of the object in the sky, $\hat{\mathbf{s}}$. Simplifying the equation in this way is attractive because it pulls out the shared delay. Applying this and separating the spatial and temporal components:

$$\psi_1 \sim e^{-ik\hat{\mathbf{s}}\cdot\mathbf{x}_1} e^{-iwt} \tag{2.5}$$

$$\psi_2 \sim e^{-ik\hat{\mathbf{s}}\cdot\mathbf{x}_1} e^{-ik\hat{\mathbf{s}}\cdot\mathbf{B}} e^{-iwt} \tag{2.6}$$

As the magnitude of the electric field has already been ignored, the shared term of $e^{-ik\hat{\mathbf{s}}\cdot\mathbf{x}_1}$ can also be absorbed into the normalization of the waves. An additional factor of e^{ikd_i} is needed for each wave to account for the delay needed in each telescope. For example, the first wave becomes:

$$\psi_1 \sim e^{ikd_1} e^{-iwt} \tag{2.7}$$

With all the major components of light collection and delay correction handled, what remains is the interference of the two waves. The combination is just the linear superimposition of the two:

$$\psi_{\text{tot}} = \psi_1 + \psi_2 \tag{2.8}$$
$$\sim e^{-iwt}e^{ikd_1} + e^{-ik\hat{\mathbf{s}}\cdot\mathbf{B}}e^{-iwt}e^{ikd_2} \tag{2.9}$$
$$= e^{-iwt}(e^{ikd_1} + e^{ikd_2}e^{-ik\hat{\mathbf{s}}\cdot\mathbf{B}}) \tag{2.10}$$

This expression is tantalizingly close to an actual observable. All that remains is finding the magnitude of the combined wave, which is the power, P, and taking the time average:

$$\begin{aligned} P \sim |\psi_{tot}|^2 &= 2(1 + \cos(k(\hat{\mathbf{s}} \cdot \mathbf{B} + d_1 - d_2))) \\ &\sim 2(1 + \cos(kD)) \end{aligned} \tag{2.11}$$

The above Eq. 2.11 is the equation of interference fringes. The equation is currently unitless, but can readily be scaled to account for the total power absorbed, which is simply the product of the incident flux on the telescope and the area of the telescope.

Observing the power of the fringes is not enough to glean any information about the targets. The interferometer is capable of reverting the power of the fringes back into a brightness distribution of the target. The Michelson visibility, V, is defined from Eq. 2.11 as the contrast:

$$V = \frac{P_{\max} - P_{\min}}{P_{\max} + P_{\min}} \tag{2.12}$$

This same visibility can be found by expressing the power as an integral over a solid angle on the sky:

$$V(k, \mathbf{B}) = \int A(\alpha, \beta)F(\alpha, \beta)e^{-k\hat{\mathbf{s}}\cdot\mathbf{B}}d\Omega \tag{2.13}$$

Where α and β are the angular sky coordinates, A is the area of the telescopes, and F is the flux. A final transformation allows the visibility to be expressed in terms of spatial frequencies, u and v, which can be determined from the orientation of the telescopes and the target on the sky. These are the coordinates of the Fourier transform of the angular sky coordinate visibility:

$$V(u, v) = \int A(\alpha, \beta)F(\alpha, \beta)e^{-2\pi i(\alpha u + \beta v)}d\alpha d\beta \tag{2.14}$$

As was mentioned, the visibility is connected to the brightness distribution of the source. The van Cittert-Zernike theorem is the crux of astronomical interferometry [75]. The theorem allows the construction of arbitrary brightness distribution and to determine the observed visibilities as a function of the baseline (i.e. spatial frequency).

For this project there are three relevant brightness distributions: point source, uniform disk, and limb darkened disk. These distributions are shown in the first column of Figure 2.4. A point source is any object which is not resolved for the baseline and wavelength

used. At all points in the u-v plane, the point source has the same visibility $V = 1$. The uniform disk is simply a disk of light against the background sky, with all points in the disk at the same brightness. Approximating a star as a uniform disk falls short when treating the opacity of the stellar atmosphere. That is to say, when looking at the center of the star, the observer sees deeper into the star where it is brighter. When looking at the edges, or limbs, of the star, the observer does not see deeply or into brighter matter. Limb darkening is well modeled with polynomial fits of low degrees.

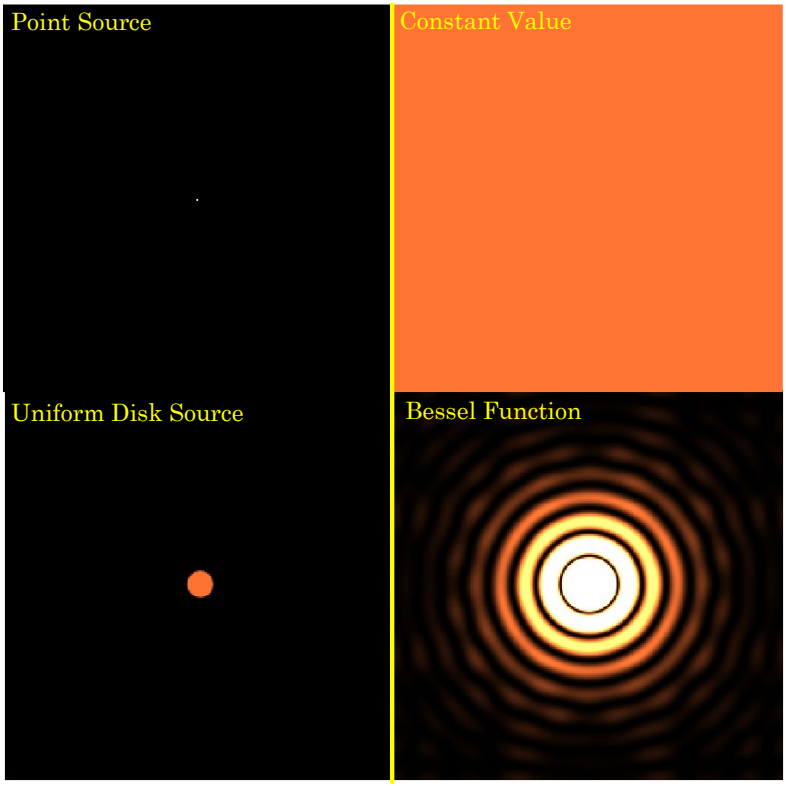

Figure 2.4. Relevant brightness distributions and their corresponding Fourier transforms. Top-left shows a point source which transforms to top-right, a constant plane. Bottom-left shows a uniform disk which transforms to bottom-right, a Bessel function. The bottom-right figure shares many similarities with the limb darkened disk solution.

One can model two dimensional images of arbitary brightness distributions and apply a 2D Fourier transform to predict what the visibility distribution is in the u-v plane. The Fourier transform is reversible, allowing observers to glean information about the brightness distribution of the target on the sky. The Fourier transform of the point source is simply a constant value at all points. The uniform and limb darkened disk have similar transformations on the u-v plane and can be written in the same expression:

$$V^2 = \left[\left(\frac{1-\mu}{2} + \frac{\mu}{3} \right)^{-1} \cdot \left((1-\mu) \cdot \frac{J_1(x)}{x} + \mu \sqrt{\frac{\pi}{2}} \cdot \frac{J_{3/2}(x)}{x^{3/2}} \right) \right]^2 \tag{2.15}$$

where μ is the wavelength dependent limb darkening coefficient, $x = \dfrac{\pi B \theta}{\lambda}$, and $J_n(x)$ is the Bessel function of the first kind. Eq. 2.15 can be used for both the uniform and limb darkened model by changing the limb darkening coefficient. If no limb darkening is desired, the coefficient is set to 0.

The preceding theory describes a simple finite bandwidth interferometer which uses only a single baseline. It also only describes one bit of information that interferometry gives, the visibility. Instruments using multiple baselines can yield more information about the source such as the closure phase and polarization. However, these techniques will not be utilized in this work and are only mentioned for completeness.

The interference of light is more than a quirky behavior of a ghostly particle, or wave, or both. Interference provides a means to transform the contrast of fringes into information about the source. Further, interferometry allows astronomers to observe at resolutions financially and technically impossible with standard telescopes.

Chapter 3.
Astronomical Interferometers

3.1 A Few Historically Significant Interferometers

Astronomy has benefited from a century of astronomical interferometry. Though the original goal of interferometry was to measure the diameters of stars, it has contributed in the fields of binary stars, debris disks, exoplanets, and stellar evolution.

The first functioning interferometer was of Michelson's own design. The device consisted of a 6 m metal beam which was mounted on the top of the Hooker 100 inch telescope at Mount Wilson, CA. Michelson's stellar interferometer used two mirrors at the extremes of the metal beam and combined the light using the 100 inch primary mirror. The first fringes were observed from the supergiant star Betelgeuse, $\theta = 40$ mas [89]. Michelson's studies were carried out in collaboration with the other father of astronomical interferometry, Francis Pease.

Due to the design, the Michelson stellar interferometer had a fixed baseline throughout an observation and required manually adjusting the on axis mirrors to change the resolution. Michelson was unable to manufacture larger beams to increase the angular resolution. Radio interferometry became the champion of astronomical interferometry twenty years following the experiments of Michelson. Radio interferometry was a more attractive target as radio dishes are generally cheaper to develop and the data can be recorded and analyzed later. It would not be until the advent of the computer age before interferometry could actively track fringes in the visible or optical wavelengths and probe the sub milli-arcsecond domain.

The next major endeavor in interferometry was the Narrabri Stellar Intensity Interferometer. This was an optical interferometer located in Australia whose observations concluded in 1974. The Narrabri interferometer utilized a technique dissimilar to a Michelson's. The technique of intensity interferometry (not to be confused with Michelson's *amplitude* interferometry) used by Narrabri was based on the work of Brown & Twiss [20] and measures correlations in the light received at the two telescopes rather than the interference pattern. Narrabri was used in the measurement of the stellar diameters of the brightest (B magnitude < 2.5) stars with its ~ 180 m baseline including the brightest star in the night sky Sirius [52, 53].

A decade later, the Mark III interferometer was constructed on Mount Wilson [110]. The Mark III surpassed the Michelson stellar interferometer's baseline with its 32 m span. The baseline was configurable and was capable of going as small as 3 m. Further improvements included broadband observations in the visible spectrum. The Mark III greatly contributed to the study and resolution of spectroscopic binary stars, stars which orbit each other and whose gravitational effects are observed in the Doppler shifting of the starlight, and the angular diameters of stars in general [109]. Mount Wilson was the home of the Mark III interferometer until the early 90s when it was decommissioned. The Mark III was eventually replaced with the primary instrument used in this work, the CHARA Array.

The 1990s saw an explosion in the development of long baseline optical and infrared interferometers. The Navy Precision Optical Interferometer (NPOI), which began its observations in 1992, currently boasts the world's largest single baseline of 437 m, though originally operated at 10s of meters. NPOI measured diameters of dozens of giant and supergiant stars [96].

After decades of continual upgrades, NPOI currently is capable of cophasing six telescopes simultaneously for high precision astrometry and image synthesis.

Around the same time as NPOI began its work, the Palomar Testbed Interferometer (PTI) was built as a prototyping and development ground for the Keck Interferometer. PTI developed many of the techniques used in interferometry today such as laser guided metrology for automated fringe tracking. An interesting first result from PTI that highlights interferometry's continual contribution to the field of exoplanets is exploring 51 Peg for an unresolved companion [14]. 51 Peg is the first solar type star which was found to have a planet orbiting it which arguable was the beginning of the era of exoplanets [86]. The Keck Interferometer leverages the 10 m Keck telescopes on a $\sim$ 90 m baseline for a resolution of 5 mas in its shortest operational wavelength. The Keck Interferometer utilized the massive collecting power of its telescopes to resolve the first extra-galactic object with an interferometer [114]. Experiments with the Keck Nuller measured dozens of stellar diameters in the K-band [29].

A final interferometer that I would like to mention here is the Very Large Telescope Interferometer (VLTI), not only for its creative name, but for the impressive power and technological developments spearheaded at this instrument. The VLTI can be fed from the four 8.2 m Unit Telescopes or the 1.8 m Auxiliary Telescopes. At peak performance, the VLTI has a limiting magnitude of 14. The VLTI has also probed the angular diameters of M dwarfs [108, 34, 100]. The VLTI is a powerhouse of imaging and astrometry with the recent GRAVITY instrument [49]. In 2019, the GRAVITY was used to measure the first spectrum of an exoplanet observed with interferometry [50], further demonstrating interferometry's important role in exoplanet science. The GRAVITY instrument has also measured the diameters of the faint M dwarf binary system GJ 65AB, which are used later in this thesis [9].

3.2 The CHARA Array

The CHARA Array is an optical and infrared astronomical interferometer which began construction in 1984 [117]. The array consists of six 1 m telescopes arranged in Y-shaped spokes. The telescopes are named after the cardinal direction in which they are located relative to the central lab (E-East, S-South, and W-West) and numbered 1 or 2, where 1 is the further out telescope. The smallest separation between any two telescopes is approximately 30 m and the largest 330 m. There are 15 different combinations for single baseline observing modes, with baselines ranging between those two extremes. The full set of available baselines and smallest resolution available are shown in Table A.1

The light from the primary mirror of a telescope is kicked off the side of the telescope where it splits. A small portion of the light is sent to an adaptive optics system which uses deformable mirrors to mitigate atmospheric turbulence. The remainder of the light goes down through a hole in the base of the telescope where it enters an evacuated pipe connecting each telescope to the central lab.

Once in the central building the light enters the Optical Path Length Equalization (OPLE) lab. As the interferometer requires the light from the two telescopes be in phase, one of the telescopes beams, and path length, is fixed at a certain distance. The other beam is allowed to vary its OPL by reflecting off movable carts traveling on high precision rails

inside a 100 m long building. The length of the OPLE lab is necessitated by the requirement to correct the OPLs by an amount as great as the interferometer's baseline. The OPLE lab uses highly precise measurements of a system of mirrors to correct the OPL by an amount as little as 1 μm. When the OPL has been corrected, the light then leaves the OPLE lab and is sent to the desired beam combiner.

There are currently four beam combiners that are actively in use on the CHARA array: Classic/CLIMB; PAVO; MIRC-X; and SPICA. The main distinction between the instruments are the operational bandpasses, the number of simultaneous spectral channels, and the number of beams combined. There are other important distinctions such as the optical design, camera specifications, and sensitivity, but for now it suffices to cover the previous distinctions.

Classic is the original instrument at Mount Wilson and saw CHARA's first sky fringes [116]. The Classic instrument observes in one of two infrared bandpasses, H centered at 1.673 μm and K' centered at 2.133 μm. The smallest resolution with Classic is approximately 0.5 mas. Classic is a single spectral channel instrument, which translates to only one visibility measurement per object integration. Classic can also take input from a third telescope, at which point it is no longer Classic, but CLassic Interferometry with Multiple Baselines or CLIMB.

PAVO differs from Classic in that it is an optical instrument and observes in the Johnson R filter centered at 635 nm. PAVO is also an integral field unit and records a spectrum of interference fringes instead of just a single spectral channel [61]. The resolution of PAVO, 0.2 mas, is an impressive improvement upon Classic. PAVO is designed to combine light from three telescopes, for three distinct combinations, though most frequently it is used on only a single baseline.

The Michigan Infrared Camera (MIRC/MIRC-X)[1] is a 6 telescope infrared combiner [90, 6]. MIRC-X differs from Classic in two significant ways: 1) it can uses all six telescopes simultaneously; 2) MIRC-X disperses the light before integration to measure a spectrum of fringes rather than a single channel. While the primary science cases of MIRC-X are imaging and astrometry, which leverage the ability to measure a different interferometric property called closure phase, MIRC-X has a powerful use case in measuring stellar diameters. MIRC-X, when operating all 6 telescopes, provides 15 baselines in 8 spectral channels simultaneously measuring 120 visibility samples — two orders of magnitude more data than a single observation with Classic. Though powerful, these measurements are correlated and the observational constraints discussed in § 5.1 still apply.

Finally, there is the SPICA 6 telescope optical beam combiner [94]. SPICA, which is the upgrade and replacement to CHARA's previous multi-telescope optical combiner VEGA [91], is the newest beam combiner on the mountain and is the visible light analog to the MIRC-X instrument. SPICA is assisted by near-infrared fringe tracking in the H band. This allows SPICA to quickly find fringe offsets and maintain OPL equalization. SPICA aims to characterize over 1,000 stars over a wide range of spectral types. One result from VEGA somewhat relevant to this thesis is constraining surface brightness relations for late-type red giants [95]. As will be discussed in Chapter 4, I have utilized VEGA data to characterize a

[1]The "X" is for the University of Exeter, who has been collaborating with the MIRC team in recent instrument developments.

unique K dwarf star.

There are approximately 30 reflections and several beam splittings in the CHARA optical path between the primary telescope and the beam combiner's camera. Treating just the reflections, which typically are ∼97% efficient at best when averaged over the visible spectrum, the final throughput is at best 2% of the original gathered light. The throughput does depend on wavelength, as the mirror coatings perform better for infrared light, but the sensitivity of the infrared and optical instruments is about the same. The sensitivity limit is also determined by the readout noise from the instrument's beam combiner. For this survey, CHARA's design limits targets to brighter than ∼8.5 mag in the H or K' bands.

Chapter 4.
HD 97658: A Prelude to the Survey

Before the LIGERS survey was undertaken, I measured the diameter of HD 97658 using the Classic and PAVO beam combiners (with additional data from collaborators using the VEGA beam combiner). I then characterized its exoplanet HD 97658 b, a super-Earth, using the *TESS* lightcurve and literature radial velocity measurements. This was a useful exercise in developing a reduction pipeline and showing the consistency of three different beam combiners at the CHARA array. The original publication of my work on HD 97658 is reproduced here.

4.1 Introduction

Interferometric observations of stars provide a unique opportunity to directly measure one of the most fundamental parameters of the star: its radius. Interferometry achieves the resolution of an extremely large telescope by combining the light from one or multiple pairs of telescopes across a variety of separations, or baselines. In particular, optical/near-infrared interferometry requires baselines of only tens of meters to achieve resolutions of milli-arcseconds (mas). Direct measurements of stellar radii at great precision will in turn reduce uncertainty in other derived stellar parameters (e.g. effective temperature, surface gravity, or density). Direct observations of stellar radii have highlighted a systematic discrepancy between evolutionary models and reality. Boyajian et al. [18] has shown that stellar evolutionary models underestimate radii by $\sim 5\%$ and overestimate temperatures by $\sim 3\%$ for K and M dwarfs.

Observations with interferometric arrays play an important role in understanding as well as refining exoplanet system properties. In order to understand the properties of the exoplanet, the properties of the star must first be well constrained. In particular, transiting exoplanets provide a measure of the planet's radius, but this measurement is in units of the host star's radius. Any uncertainty or bias in stellar radius will propagate into estimates of the planet's equilibrium temperature, density, habitability, and composition. Interferometry gives a direct measurement of the stellar radius with little or no dependence on stellar models. This technique has been used in the literature to refine the properties of several important systems, such as 55 Cancri which hosts five radial velocity exoplanets including another transiting super-Earth [124] and transiting exoplanet host star GJ 436 where evolutionary models underestimated the stellar radius by $\sim 11\%$ [125]. There have also been multiple interferometric surveys of large numbers of exoplanet host stars such as Baines et al. [8]. The field of interferometry has also seen incredible developments in the field of imaging and astrometry with the ESO GRAVITY project [49]. In 2019, the GRAVITY collaboration announced the first spectrum of an exoplanet observed with interferometry and refined the astrometric position with 100μas precision [50].

This chapter was previously published as Tyler G Ellis, Tabetha S Boyajian, Kaspar von Braun, Roxanne Ligi, Dénis Mourard, Diana Dragomir, Gail H Schaefer, and Christopher D Farrington "Directly Determined Properties of HD 97658 from Interferometric Observations" 2021 *Astronomical Journal* AJ 162 118. The article can be accessed at `https://doi.org/10.3847/1538-3881/ac141a`

The exoplanet host star HD 97658 is of particular interest in this regard as it is the home of a transiting super-Earth [36, 56]. HD 97658 is a bright, m_V=7.78 mag K1 dwarf with a moderately low iron content of [Fe/H]= −0.23 dex, which was discovered to have a Neptunian mass exoplanet by the NASA Eta-Earth Keck-HIRES radial velocity survey [56]. Follow-up time series observations with the *Spitzer* and *MOST* space telescopes detected a transit whose depth indicated an estimated planetary radius of a few Earth radii [36, 121]. These properties together make HD 97658b a so-called super-Earth (planets with radii of 1–4 $R_\oplus$ and masses of 1–10 $M_\oplus$; Bryan et al. 21). Super-Earths can take the form of water worlds with a smothering dense atmosphere or rocky behemoths with minimal atmospheres, both often consistent within the uncertainties of planetary mass and radius [36]. Super-Earths captivate planetary scientists as they are the most populous of observed exoplanets (30–50% of Sun-like stars host one or more super-Earths [21]), however they do not exist within our own solar system and must be studied solely as exoplanets.

We are interested in refining the properties of HD 97658b by directly measuring the host star's properties. In §4.2, we describe the interferometric observations of HD 97658. In §4.3, we report the resulting directly measured angular diameter, bolometric flux. In §4.4, we model and measure the mass of the star. We then derive updated properties of HD 97658 and its planet using the TESS lightcurve and our measured results. Lastly, in §4.4.4 we summarize and conclude this work.

4.2 Interferometric Observations

We observed HD 97658 over the course of several nights using the Georgia State University Center for High Angular Resolution Astronomy (CHARA) Array at the Mount Wilson Observatory using the Classic (near-IR), VEGA (optical), and PAVO (optical) beam combiners [117, 92, 61]. A summary of the observations is found in Table 4.1.

An interferometer measures visibilities (V), which quantifies the contrast of the dark and bright parts of the interference fringe pattern. In practice, this is the contrast of the time-averaged minimum and maximum power of the fringe pattern (see Lawson [75] for a full description of what an interferometer measures in Chapter 2.6).

As the visibilities measured at the time of observing include instrumental and atmospheric effects, it is necessary to observe stars with predictable visibilities to calibrate the data. These calibrator stars are observed in sequence with a science star and allow a measure of the combined systematic effects. Calibrators stars are of a known, and ideally unresolved, size.

Each observation consists of bracketed sequences of the form calibrator 1 - science target - calibrator 2 (or calibrator 1 again), and then reverse. One bracket is one observation of the target sandwiched by the calibrators.

As the beam combiners used in this work observe in different bandpasses, it is sometimes necessary to use different calibrators for each instrument. Wherever possible, we calibrated the raw square visibilities of the calibrators against each other [123]. This provides insight into previously unknown duplicity, activity, or other anomalous behaviors in a calibrator. No stars were expunged from our list of acceptable calibrators for any reason. The limb darkened angular size of the calibrators and magnitudes are summarized in Table 4.2.

We chose calibrators for this work using the JMMC Stellar Diameter Catalog (JSDC) version 2 [25, 38][1]. Ideally, we restrict our search for calibrators that are not resolved on the baselines used with beam combiner's bandpass. Unresolved sources have predicted squared visibilities $V^2 \gtrapprox 0.9$. Further, we discard potential calibrators that have known duplicity and/or have rapid rotation driving equatorial distention. Lastly, preference is given to calibrators of comparable brightness and with a minimal angular separation in the sky from the science target.

Calibrator selection is a nontrivial process which can affect the uncertainties in final calibrated data. van Belle & van Belle [120] demonstrated that a 5% uncertainty in the calibrator diameter can propagate up to a $\sigma_{V^2} \sim 0.04$ uncertainty in the calibrated visibilities, though the amount depends on interferometer configuration, instrument, and calibrator size. Oftentimes, for small, faint targets such as HD 97658, most calibrators which are sufficiently smaller so as to be unresolved are often too faint to be observed. As such, it is sometimes necessary to compromise for partially resolved calibrators. The caveat with such a compromise is that the target's diameter will only be known as well as the calibrators. In this work, the calibrators HD 101688 and HD 96738 are slightly resolved using the PAVO/VEGA beam combiner and S1-W1 baseline, $V^2 \simeq 0.6$. Thus, the predicted angular size of these calibrators are of concern to the error budget. However, within this size regime, $\theta < 0.45$ mas, the dominant source of error is in the measurement of the visibilities rather than assumptions of calibrator size [120].

We used the *isoclassify*[2] program to estimate the angular diameters of these calibrators independently of the JMMC's surface brightness relationship method [57, 12]. We find the *isoclassify* and JMMC diameters to be consistent, though the adopted *isoclassify* diameters had larger, more conservative uncertainties (an average of 1.9× larger). All of differences in size are less than 1σ, with the average statistical tension $Avg\left((|\theta_{\rm iso} - \theta_{\rm JMMC}|)/\sqrt{\sigma^2_{\rm iso} + \sigma^2_{\rm JMMC}}\right) = 0.33$.

As previously mentioned, the greater uncertainty in the calibrated visibilities from using resolved calibrators is propagated forward into the uncertainty of the fitted angular diameter. We also note that data taken with the VEGA on several nights are calibrated with only a single star. However, our analysis finds consistency in the calibrated results from night to night and between PAVO and VEGA, assuring confidence in our choice of calibrators and calibration methods [77, 7, 74].

In order to complete an observation, the interferometric fringes must be found by equalizing the optical path length from the stars to the beam combiner through the two telescopes. The fringes are found by scanning the additional path length up and down for one of the telescopes until fringes are detected. In good conditions, scanning initially takes about 5–15 minutes per star and about twice that in difficult observational conditions. Finding the fringe packet for subsequent observations of the same star typically goes much faster, at most a few minutes.

Observations with the Classic beam combiner consist of approximately 2.5 minutes of integration in the H band. Shutter sequences proceed and follow integration. Classic data are reduced using the `REDFLUOR` package to produce raw squared visibilities which are then

[1] `http://www.jmmc.fr/catalogue_jsdc.htm`

[2] `https://github.com/danxhuber/isoclassify`

calibrated using the `CALIBIR` package — both of these software routines are provided as binary executables from CHARA [3]. Classic observes in a single spectral channel at a time and gathers a single data point per bracket.

Observations with the PAVO beam combiner consist of around 2 minutes integration followed by approximately 3 minutes of shutter sequences and dark integration for reduction and calibration. PAVO data are reduced and calibrated using IDL routines which are also provided by CHARA [61][4]. As PAVO is an integral field unit, it collects a spectra of fringes with each bracket between 630-950 nm bandwidth (resolution R = 30) [61].

Observations with VEGA require more time. Calibrators are observed during ∼15 min while the science star is generally observed during ∼30 min to ensure enough signal. The data are then reduced using the `vegadrs` pipeline [92, 93]. VEGA's bandpass is broken into 20 nm bins and creates two data points per baseline at a time.

Table 4.1. Summary of observations of HD 97658. Both PAVO and Classic instruments were used in the single baseline mode of the CHARA array, while VEGA uses multiple baselines simultaneously. See ten Brummelaar et al. [117, Table 1] for a complete description of the available baselines. Each bracket corresponds to one observation of the target. See § 4.2 for further details

Date [UT]	Baseline	Combiner	Brackets	Calibrators
2015-02-04	S1/W1	Classic	5	HD 93152, HD 99267
2015-02-05	S1/W1	Classic	7	HD 95804, HD 99267
2015-02-11	S1/W1	PAVO	4	HD 101688, HD 96738
2017-03-13	W1/W2	VEGA	2	HD 89239
2017-03-17	S2/W2	VEGA	2	HD 107168
2018-04-28	E2/W2	VEGA	2	HD 97638
2019-05-05	S1/W2	VEGA	3	HD 96738
2020-03-05	S2/E2	VEGA	4	HD 96738, HD 107168

Table 4.2. Summary of calibrator stars used in all observing campaigns. All photometry data are taken from the JMMC Stellar Diameters Catalog v2. The cited angular diameters are limb darkened and estimated using *isoclassify*.

Calibrator	V mag	H mag	θ_{UD}[mas]
HD 89239	6.530	6.599	0.159±0.008
HD 93152	5.285	5.384	0.279±0.012
HD 95804	6.766	6.288	0.208±0.005
HD 96738	5.593	5.442	0.269±0.033
HD 99267	6.606	6.091	0.241±0.006
HD 101688	6.291	5.730	0.281±0.011
HD 107168	6.220	5.969	0.241±0.011

[3] `http://www.astro.gsu.edu/~theo/chara_reduction/index.html`

[4] `https://gitlab.chara.gsu.edu/fabien/pavo.git`

4.3 Directly Determined Stellar Properties

4.3.1 Stellar Diameter

The calibrated squared visibilities V^2 can be fit to the radial profile of the 2D Fourier pair of a uniformly illuminated disk or a limb darkened disk, $\theta_{\rm UD}$ and $\theta_{\rm LD}$, respectively. The resulting profile is a function of the projected baseline B, observational wavelength λ, and most importantly the angular size of the object [54]. The functional form, shown in Eq. 4.1 is a combination of Bessel functions of the first kind, $J_\alpha(x)$, scaled with the linear limb darkening coefficient μ.

$$V^2 = \left[\left(\frac{1-\mu}{2} + \frac{\mu}{3} \right)^{-1} \cdot \left((1-\mu) \cdot \frac{J_1(x)}{x} + \mu \sqrt{\frac{\pi}{2}} \cdot \frac{J_{3/2}(x)}{x^{3/2}} \right) \right]^2 \tag{4.1}$$

where $x = \dfrac{\pi B \theta}{\lambda}$.

We fit the uniform disk model, Eq. 4.1 with $\mu = 0$, for the combined datasets using the *Scipy curve_fit* nonlinear least-squares minimization routine [65]. As part of the fitting process, we find the optimized fit for many realizations of the dataset by sampling the wavelength solution uncertainty. The resulting distribution of fits for the uniform disk is $\theta_{\rm UD} = 0.296 \pm 0.004$ mas. We performed the fitting routine for the VEGA and PAVO datasets separately as a check for consistency and found the best fit uniform disk angular diameters of $\theta_{\rm UD,VEGA} = 0.282 \pm 0.024$ mas and $\theta_{\rm UD,PAVO} = 0.296 \pm 0.004$ mas. As seen in Fig. 4.1, there is more internal spread amongst the VEGA data than the Classic or PAVO data, which drives the uncertainty up slightly. The enlarged uncertainties are likely caused by dividing the starlight of this faint target amongst the multiple simultaneous baselines of VEGA. We opt not to perform this same fit with the Classic data as HD 97658 is not well resolved by the instrument, but can still act as a sanity check for the other instruments. The uniform disk angular diameter and other stellar properties are summarized in Table 4.3.

We fit the limb darkened disk model using the same technique as above, adding in Monte Carlo realizations of the limb darkening parameter μ as part of the fitting process. As all visibility curves are near unity at low spatial frequencies, it is safe to combine the Classic data with the VEGA/PAVO data. We estimated the limb darkening parameter μ using the Limb Darkening Toolkit (LDTK) [97, 58]. Throughout this work we find the limb darkening coefficient and associated limb darkened diameter in the Bessel R filter. We provide the LDTK module with estimates of $T_{\rm eff}$, $\log(g) = 4.5 \pm 0.1$, $Z = 0.03 \pm 0.01$. We iterate the fitting process twice to reflect our refined measurements in $T_{\rm eff}$ which goes into the estimation of the limb darkening coefficient. The first run uses the fit of $\theta_{\rm UD}$with our measurement of the bolometric flux to estimate $T_{\rm eff}$, as is discussed in the following section § 4.3.2. Then we use the results from the first fit of $\theta_{\rm LD}$to estimate $T_{\rm eff}$ and find our new estimation of μ. With the final estimation of μ, we then find our final fit of $\theta_{\rm LD}$. We scale the uncertainties in μ by a factor of 5 during each iteration of the fitting process as the LDTK distribution seems unrealistically tight when compared to Claret & Bloemen [28], though this does not significantly contribute to the final error budget. Our final estimation of the linear limb darkening coefficient in the Bessel R filter is $\mu_{\rm R} = 0.629 \pm 0.014$.

The iteration process resulted in a best fit limb darkened angular diameter of $\theta_{\rm LD} = 0.314 \pm$ 0.004 mas. The reduced chi-square for the linear limb darkened model is $\chi^2_{\nu=113} = 0.934$ ($p = 0.68$), indicating good agreement between theory and observation. This fit and the calibrated squared visibilities are shown in Figure 4.1 with the uncertainties scaled to fix χ^2_ν at unity.

We calculate the physical radius of HD 97658 as 0.728 ± 0.008 $R_\odot$ using the Gaia EDR3, zero-point corrected parallax measurement (Table 4.3). Applying the zero-point correction, the Gaia parallax of 46.412±0.022 mas yields a corresponding distance of $d = 21.546 \pm 0.011$ pc [46, 78]. Previously published radius estimates include Dragomir et al. [36] who obtained an estimate of $0.703^{+0.035}_{-0.030}$ $R_\odot$ from evolutionary models fit within `EXOFAST` (Eastman et al. [41]) and van Grootel et al. [121] who derived $0.741^{+0.024}_{-0.023}$ $R_\odot$ from the spectroscopic temperature, bolometric correction, and Hipparcos parallax. It is of interest that the estimation of the radius using the evolutionary models in `EXOFAST` is lower than the spectroscopic radius and the directly measured radius in this paper. As has been explored in Boyajian et al. [18], evolutionary models systematically underestimate the radius by a few percent. The high resolution capabilities of the interferometer complemented with the exquisite parallax measurements from Gaia allow us to report a physical radius with about 1/3 the uncertainty of prior works. The uncertainty in our physical radius predominantly comes from the fit of the angular diameter, with the parallax contribution essentially negligible.

4.3.2 Bolometric Flux and Temperature

We fit an interpolated K0.5 Pickles [99] template spectrum to collected literature measurements of broadband photometry to measure the bolometric flux. Photometry used in this fit include measurements in Johnson *UBV*, Cousins R_c, I_C, 2Mass *JHK*. The photometric measurements are from van Leeuwen [122], Skrutskie et al. [111], Kotoneva et al. [71], Koen et al. [70], Bessell [13], Kharchenko [69], Droege et al. [37], Mermilliod [88].

Interstellar extinction was fixed at 0 in the fitting routine as the proximity of the star should render any extinction effects negligible. The fit was also performed with A_V as a free parameter. This modification found a value of $A_V = 0.027 \pm 0.015$, so we accept our original assumption of no extinction for this work.

The template spectra was then scaled to fit to the photometric measurements and integrated to obtain a bolometric flux $F_{\rm bol}$=$2.42 \pm 0.05 \times 10^{-8}$ erg s^{-1} cm^{-2} . We use the updated filter profiles and zero-point corrections as discussed in Mann & von Braun [84]. Further, we account for unknown systematics by applying a 2% addition in quadrature to the bolometric flux uncertainty as is suggested in Bohlin et al. [15]. Our flux measurement and the parallax distance gives a stellar luminosity of L=0.351 ± 0.007 $L_\odot$. The assembled photometry and spectral fit are shown in Figure 4.2. This model has a goodness of fit of $\chi^2_{\nu=29} = 0.79$ ($p = 0.78$). Further details of this technique are available in van Belle et al. [119], von Braun & Boyajian [123]. We extended the infrared portion of the Spectral Energy Distribution (SED) ($\lambda > 12.5$ μm) with the WISE W 1–4 data to check for an infrared excess, but did not observe any such excess [129]. We note that HD 97658 is saturated in W1 and W2, so we opted to exclude all of these data from the SED fit.

The Stefan-Boltzmann equation can be rewritten to express the temperature in terms of

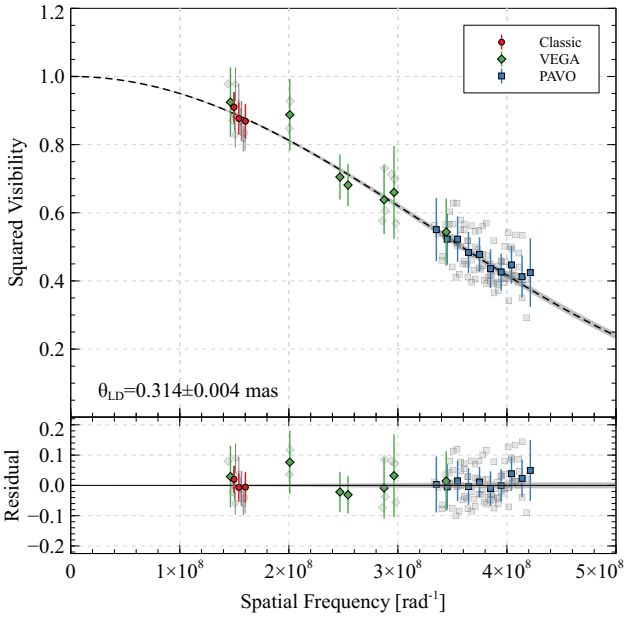

Figure 4.1. Top panel shows the calibrated squared visibilities and uncertainties from CHARA observations of HD 97658. We binned and averaged the data by equal spacing in of 10^7 rad^{-1} for clarity, and plot these points over all of the calibrated data shown in transparent grey. Classic observations are shown as red circles grouped on the left at lower spatial frequencies, VEGA observations are green diamonds in the middle, and PAVO observations are blue squares grouped on the right at higher spatial frequencies. The fitted visibility curve for a limb darkened disk is shown as a dashed line with the parameters found in §4.3.1. We show the uncertainty in the angular diameter as the grey region around the best fit curve. The residuals for the fit are shown in the bottom panel. See § 4.3.1 for details.

the observables — bolometric flux and angular diameter:

$$T_{\rm eff} = 2341 \cdot \left(\frac{F_{\rm bol}}{\theta_{\rm LD}^2} \right)^{1/4} \ {\rm K}, \tag{4.2}$$

where the bolometric flux is in units of 10^{-8} erg s^{-1} cm^{-2} and the angular diameter is in mas. We determined an effective temperature of $T_{\rm eff}$=5212 $\pm$ 43 K given the limb darkened diameter and above bolometric flux. Howard et al. [56] measured the effective temperature of HD 97658 as 5170 $\pm$ 44 K which was determined from spectroscopy. This temperature is lower than what we found, but consistent with our result at the 1σ level.

4.4 Derived Stellar and Planetary Properties

Using the measured properties above, we compute here other properties of the star and its planet. As the host star plays an important role in determining many of the properties of the planet, we can also update several of the estimated properties of the planet with our

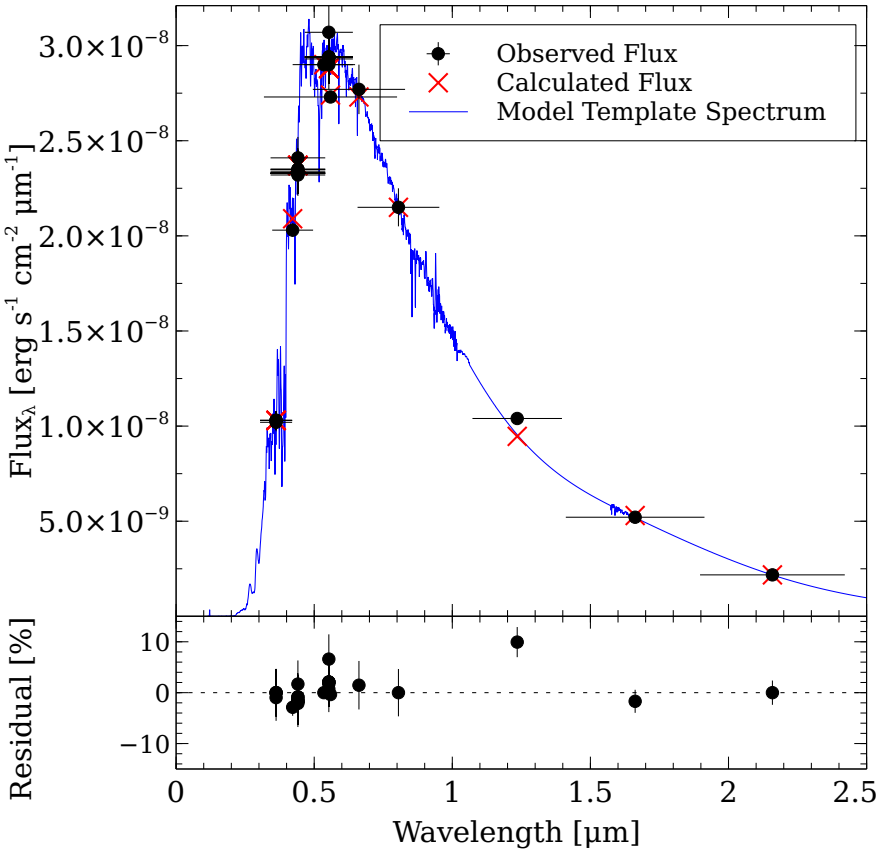

Figure 4.2. The template spectrum shown in blue is an interpolated Pickles K0.5V stellar spectrum with nominal metallicity. We used literature broadband photometry and associated uncertainties and bandpass widths to scale the spectrum. The photometry is shown as the black points. The horizontal bars on the photometry data points represent the width of the filter bandpass. This scaled spectrum was then integrated to yield the bolometric flux. We calculate the scaled model flux values at the center of the bandpasses and show them as red crosses here. The bottom panel shows the percent residual of this fit. See § 4.3.2 for discussion.

improved stellar parameters. We also include new observations of the planet's transit with TESS. A summary of all the following results is shown in Table 4.3.

4.4.1 Age and Mass Estimation with Isochrones

We use two stellar evolutionary models to estimate the stellar age and mass. The Garstec and YaPSI stellar evolutionary models [113, 127] were fit using the `bagemass` Fortran program [85]. These models use our directly measured temperature, the luminosity inferred from the parallax and bolometric flux, the spectroscopically determined [Fe/H] from Howard et al. [56], and the density inferred from the transit discussed later in this section as predictors of goodness of fit. We assumed uniform priors on age, mass, and surface [Fe/H]. One of the issues with estimating age using isochrones for this range of stellar masses is a lower mass

star afforded a longer time to evolve can have the same observable properties as a higher mass star that is younger. This bias is reflected as the elongated distribution in age and mass. We show the posterior distribution for the YaPSI and Garstec models in Figure 4.3.

We then checked the consistency of the two model's predicted age and mass using a χ^2-test. We first combined (i.e. summed) the two posterior distributions for the ages/masses and computed the resultant median age and mass. We then compute:

$$\chi^2 = \sum_{i=1}^{2} \frac{x_i - \bar{x}^2}{\sigma_i^2} \tag{4.3}$$

where x_i is the median mass/age from the two models, $\bar{x}$ is the median from the combined distribution, and σ is their associated uncertainties. Assuming that these are drawn from a χ^2 distribution, the confidence in the agreement of the two posterior distributions can be computed with:

$$p = \int_{\chi^2}^{\infty} f(\chi^2) d\chi^2 \tag{4.4}$$

The χ^2 distribution, $f(\chi^2)$, for this case has $2 - 1 = 1$ degrees of freedom, for the two samples of the age/mass. The computed p-value for the ages is p=0.62 and p=0.27 for the masses. Both the mass and age distributions agree within 95% confidence, so we conclude that the median and 1σ confidence interval of the combined distribution is representative of both. The combined isochrone models estimated the age of HD 97658 as $3.9^{+2.6}_{-2.03}$ Gyr and the mass as $0.773^{+0.015}_{-0.018}$ $M_\odot$.

HD 97658 has a chromospheric Ca II H and K activity index of $\log(R'_{HK}) = -4.971$ [62]. Isaacson & Fischer [62] then used the relationship from Mamajek & Hillenbrand [82, Eq. 3] to estimate an age of 6.06 ± 0.91 Gyr[5]. Using the Gaia $G_{BP} - G_{RP} = 0.843$ and the rotation period of 34±2 days from Guo et al. [51], we find another estimate of the age of HD 97658 of 6.25 ± 0.56 Gyr using gyrochronology with `stardate` [5]. Both of these techniques agree within $\sim 1\sigma$ of the combined isochrone model age from this work.

4.4.2 Exoplanet Modeling with *TESS*

The *TESS* mission [101] observed HD 97658 during Sector 22 for a total duration of approximately 23 days (the full Sector duration of $\sim$ 27 days, minus $\sim$ 4 day gap from d13 to d17). The normalized PDCSAP lightcurve is presented in Figure 4.4. We first use the short cadence (2 minute) mission processed PDCSAP time series data to look for signs of rotation due to starspots rotating in and out of view on the surface of the star. We find that the average brightness of HD 97658 is stable with a RMS (root mean square) of 385 ppm, having no evidence of long-term variability due to spots during this observation period. This conclusion is consistent with *TESS* observation period being shorter than the derived rotation period $P_{\rm rot} = 34 \pm 2$ d from the spectroscopic analysis of the Calcium H and K lines ($S_{\rm HK}$) [51].

Next, we search for transits in the *TESS* data by computing a Box Least-Squares (BLS) periodogram [72], shown in Figure 4.5, using the `astropy` package [6]. We identify the known

[5]In order to estimate uncertainty on this age, we applied the suggested RMS of 0.07 dex on $\log \tau$ from Mamajek & Hillenbrand [82]

[6]`https://docs.astropy.org/en/stable/timeseries/bls.html`

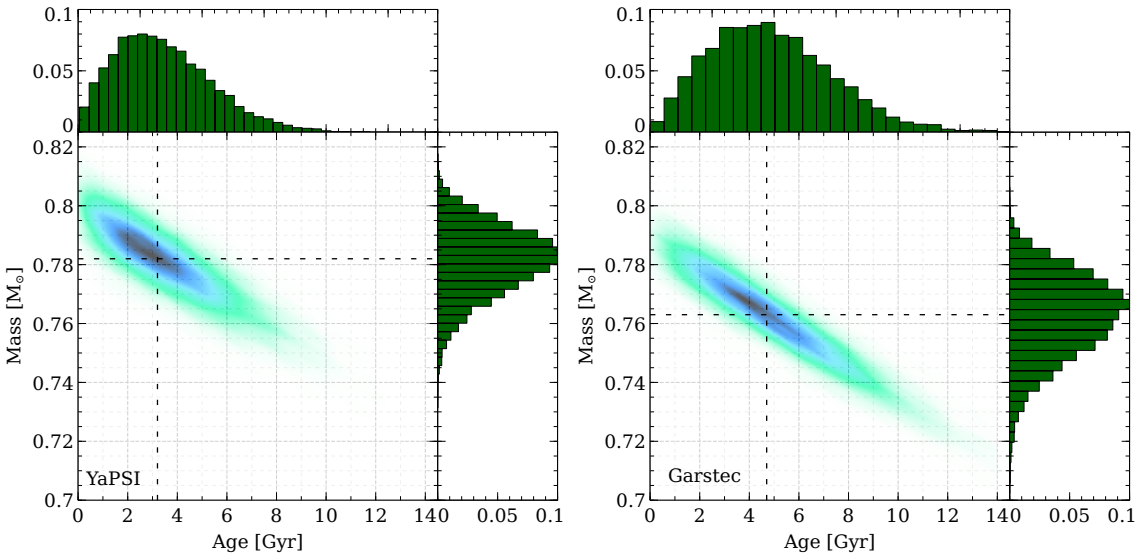

Figure 4.3. Posterior distribution of age and mass from the *bagemass* Bayesian evolutionary track fitting program as discussed in § 4.4. The YaPSI model output is shown on the left and the Garstec model on right. Higher posterior density is shown as the darker regions in the bottom left plot. The posterior population distribution for the ages is shown on the top and the posterior population distribution for the mass is shown on the right. Black dashed vertical/horizontal lines indicate the median for the age (3.2±1.9 Gyr, 4.7±2.5 Gyr) and mass (0.782 ± 0.011 $M_\odot$, 0.763 ± 0.011 $M_\odot$) for the YaPSI and Garstec models, respectively. We combine the solutions to derive a final estimated age $3.9^{+2.6}_{-2.03}$ Gyr and mass $0.773^{+0.015}_{-0.018}$ $M_\odot$ as described in § 4.4.

transiting planet HD 97658 b, with an approximate period of 9.474 d. We note that only two transits of HD 97658b are detected in TESS data, while the third falls within the data gap. We use `EXOFASTv2` [40] to simultaneously fit the orbital parameters to the *TESS* time series along with the full radial velocity (RV) data series from Dragomir et al. [36]. The program also simultaneously fit the MIST evolutionary models to estimate stellar properties [26].

`EXOFASTv2` reported a transit depth of HD 97658b of 712 ± 38 ppm with a duration of 2.80 ± 0.04 hours, centered at BJD 2458904.9366 ± 0.0008. With our measurement of the stellar radius and the transit depth, we compute a planet radius of 2.12 ± 0.06 $R_\oplus$. The resultant temperature of HD 97658b can then be found as $T_{\rm eq} = T_\star \sqrt{R_\star / 2a}$, neglecting albedo. We find the equilibrium temperature for planet b of 750±13 K. Our estimation of the equilibrium temperature is in line with the estimate from van Grootel et al. [121]. Using the planetary mass found with `EXOFASTv2`, 7.5±0.9 $M_\oplus$, and the planetary radius derived from our direct measurement of the stellar radius and the TESS transit depth, we determine a density of $\rho_{\rm p} = 3.7 \pm 0.5$ g cm^{-3}. The density is consistent within 1 σ of Dragomir et al. [36] and van Grootel et al. [121]. This fitting of the RV and transit data yielded a semi-amplitude of 2.8 ± 0.3 m/s, which is also within 1- σ of Dragomir et al. [36]. The low amplitude RV signal largely limits the uncertainty in the measurements of planet b's density and any improvements are due to the decreased uncertainty in the transit depth and stellar radius.

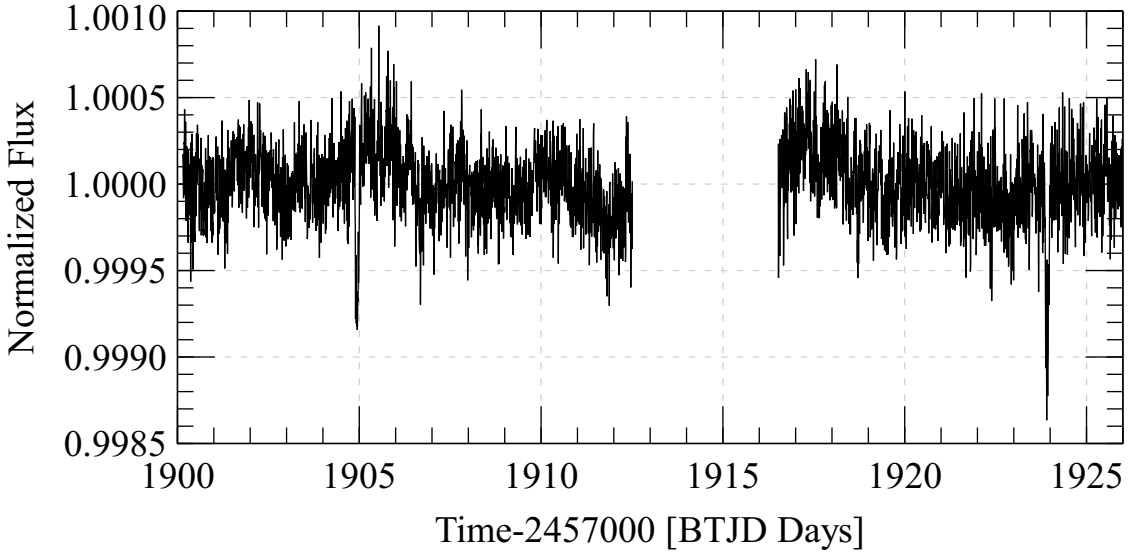

Figure 4.4. The TESS PSCSAP 2 min lightcurve binned into 10 minute bins. The known planet HD 97658b has transits at days 1905 and 1924, as well as a third transit during the gap.

Finally, we use the *TESS* time series to look for any additional transiting planets. Interestingly enough, the BLS periodogram analysis comes up with a signal at 1.054 d. We use `EXOFASTv2` to model this candidate signal as an additional planet in the system at the same time as planet b. If such a planet candidate exists, `EXOFASTv2` indicates it would have a period of $1.05443179+^{+0.00000011}_{-0.00000018}$ days and cause a transit depth of 88 ± 17 ppm lasting 1.36 hours. The T_0 for the model was found as BJD 2458907.1 ± 0.3. Given this depth and our measurement of the stellar radius, the planet candidate would have a radius of 0.74 $R_\oplus$. The planet would be located at 0.019 au with an equilibrium temperature of 1565 K, found using the same method as for planet b. The transit model overlaps with the known planet transit and reduces the depth for planet b to 674 ± 38 and the corresponding radius to 2.06 ± 0.06 $R_\oplus$. The folded lightcurve for this planet candidate is shown in Figure 4.6 right panel. The 10 minute binned out of transit photometry has a root mean square deviation of 39 ppm, about half of the transit depth.

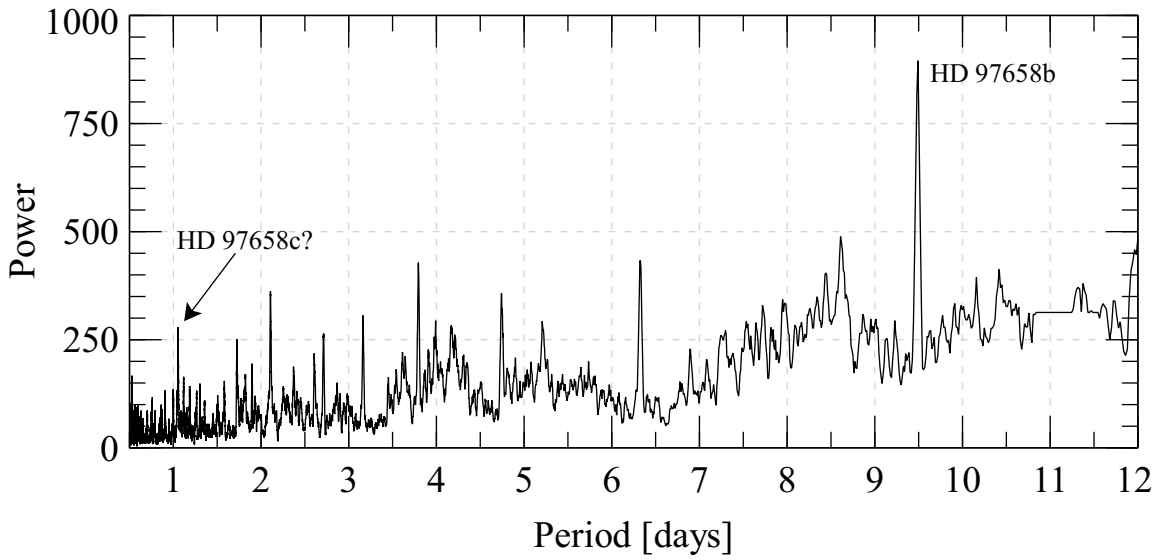

Figure 4.5. The Box Least-Squares periodogram of the TESS lightcurve of HD 97658. The strongest peak coincides with the known planet HD 97658b with a period of $\sim$ 9.5 days. Most of the other peaks are harmonics of HD 97658b, but there is a notable spike at 1.05 days which is explored as a potential planet candidate. There is a peak at $\sim$ 3.8 days which proved insignificant upon further inspection. The other peaks are harmonics of the 9.5 and 1.05 day signals.

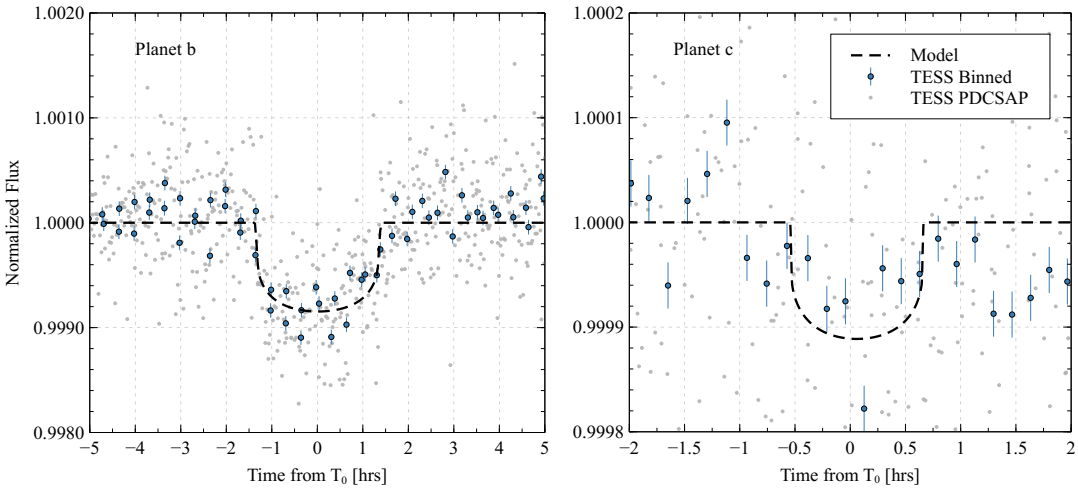

Figure 4.6. All of the TESS photometry is shown as transparent grey points. The folded and 10 minute binned TESS photometry with associated errors are shown as blue points. The transit models from `EXOFASTv2` are the dashed black line. **Left**: The best fit model for planet b with period 9.4896 days. **Right**: The `EXOFASTv2` transit model for the planet candidate "c" identified in Figure 4.5 with period 1.054 days is shown as the blue dashed line. See § 4.4.2 for details. Note that the depth is approximately an order of magnitude less than the left plot.

In attempts to verify this signal with existing data, we searched the RV data for a signal with a period of 1.05 days , but did not find evidence to support it. However, we note that a transiting planet with this period and transit depth would not be massive enough to induce reflex motions detectable with current RV instruments/observations. We compared the Bayesian Information Criterion (BIC), a measure of the goodness of the fit that penalizes over-parameterization, of the single planet model to the two planet model [105]. We find there is a small preference to the two planet model $\Delta BIC \simeq -8$. However, we still present this signal as only a candidate due to the low strength of the transit signal and lack of RV corroboration.

While beyond the scope of this paper, we propose that further investigation of this candidate would benefit from including archival time series over much longer time baselines than the TESS Sector 22 data presented here. In particular, enabling transit timing variation analysis in the orbital fit for planet b in the model could provide additional independent evidence for the putative companion "c".

4.4.3 Star and Planet Properties from Transit Observables

Seager & Mallén-Ornelas [107] demonstrated that combining the transit depth ΔF, duration τ and period P derived from the exoplanet transit lightcurve analysis yield the stellar density. Thus, with a direct determination of the stellar radius through interferometry, we can then directly obtain the stellar mass. This method has been applied to 55 Cnc [31] and HD 219134 [76], for which the joint likelihood of the stellar mass and radius ($\mathcal{L}_{MR_\star} = \mathcal{L}_{MR\star}(\rho_\star, R_\star)$)

is expressed through the probability density function (PDF) of the density and radius [see Eq. (2) of 76]. The PDF of the radius is itself expressed as a function of the PDF of the observables $\theta_{\rm LD}$ (angular diameter) and d (distance), considered as Gaussian.

This yields the PDF of the planetary mass and radius, that depends on ΔF, P, the semi-amplitude of the RV measurement K, and $\mathcal{L}_{MR_\star}$. Importantly, this method also allows computation of the correlation between parameters. This prevents, for example, determining absurd planetary densities that would not correspond to a realistic planetary mass.

Using this technique, and considering only planet b, we obtain $\rho_\star$=3.1 ± 0.3 g cm^{-3} which yields $M_\star = 0.85 \pm 0.08$ M$_\odot$, with a correlation of Corr($R_\star$,$M_\star$)=0.41. This low correlation is due to the high uncertainty on the stellar density. This direct determination of the mass is higher but consistent with those obtained with the different stellar evolutionary models.

Applying the stellar mass derived from the transit model, the interferometrically derived stellar radius, transit model, and the RV semi-amplitude we find the planetary mass $M_{\rm p}$=8.3±1.1 M$_\oplus$ and radius $R_{\rm p}$=2.12±0.06 R$_\oplus$, with the corresponding density $\rho_{\rm p}$=4.8±0.7 g cm^{-3}. These measurements are in good agreement with those found from the `EXOFASTv2` analysis. We note that the correlation between the planet's mass and radius is very low (Corr($R_{\rm p}$, $M_{\rm p}$) = 0.09). This is explained by Corr($R_\star$,$M_\star$), which is already low, and the high uncertainty on the transit and RV measurements parameters. Observations with higher precision are needed to reduce these uncertainties and increase the correlation between the parameters.

4.4.4 Conclusion

In this work we use the GSU CHARA interferometric array to obtain a highly precise measurement of the angular diameter of HD 97658. We combine measurements from both the infrared Classic instrument as well as the optical PAVO and VEGA instruments for more complete coverage of the UV plane, which helps ensure a well defined angular diameter. We also combine photometric measurements from a panoply of sources to find bolometric flux with SED fitting. These two measurements allow an estimation of temperature independent of distance measurements.

We provide the most direct measurement of the star's radius which paired with the Gaia parallax produce a ∼1% uncertainty in the physical radius and a ∼ 0.5% uncertainty in effective temperature. Previous works exploring the properties of HD 97658 were able to obtain estimates of the stellar radius and temperatures which are in good agreement with the measurements performed in this work. Because of this we cannot report substantially different composition and properties of HD 97658 b, but we can provide greater certainty in the previous results.

Follow-up observations of HD 97658 with JWST will allow a more precise and accurate measurement of the transit depth. This is a particularly interesting measurement to pin down as current best measurements of the transit depth are accurate to only ∼ 5%, which complicates more accurate analysis of the planet. These follow up observations would provide further exciting insight into this nearby super-Earth planet. We also eagerly await the Magdalena Ridge Observatory interferometer which will enable observations of fainter targets and baseline bootstrapping which will ease optimal sampling of the UV plane [30].

Table 4.3. Summarized Properties of the HD 97658 System

Property	Value	Source
Measured Stellar Properties		
Parallax [mas]	46.412±0.022	[46, 78]
Distance [pc]	21.546 ± 0.011	[46, 78]
[Fe/H] [dex]	-0.23 ± 0.03	[56]
$\theta_{\rm UD\text{-}R}$ [mas]	0.296 ± 0.004	§4.3.1 Interferometry
$\theta_{\rm LD}$ [mas]	0.314 ± 0.004	§4.3.1 Interferometry
Linear Limb Darkening $\mu_{\rm R}$	0.629 ± 0.014	§4.3.1 [97, 58]
$R_\star$ [$R_\odot$]	0.728 ± 0.008	§4.3.1 Interferometry, Parallax
$F_{\rm Bol}$ [erg s^{-1} cm^{-2}]	$F_{\rm bol}$	§4.3.2 SED Templates
$T_{\rm eff}$[K]	5212 ± 43	§4.3.2 Interferometry, SED
$L_\star$ [$L_\odot$]	0.351 ± 0.007	§4.3.2 $F_{\rm Bol}$, Parallax
Isochrone Properties — § 4.4.1		
Age [Gyr]	$3.9^{+2.6}_{-2.03}$	Combined Isochrone Models
$M_\star$ [$M_\odot$][a]	$0.773^{+0.015}_{-0.018}$	Combined Isochrone Models
`EXOFASTv2` Model Derived Properties — § 4.4.2		
Transit Depth [ppm]	712±38	`EXOFASTv2`
Period [days]	9.4897116 ± 0.0000008	`EXOFASTv2`
T_0 [BJD]	2458904.9366 ± 0.0008	`EXOFASTv2`
$R_{\rm p}/R_\star$	0.0267±0.0007	`EXOFASTv2`
Inclination [deg]	$89.05^{+0.41}_{-0.24}$	`EXOFASTv2`
Impact Parameter	$0.39^{+0.11}_{-0.18}$	`EXOFASTv2`
Eccentricity	$0.05^{+0.04}_{-0.03}$	`EXOFASTv2`
$M_\star$ [$M_\odot$][a]	0.75 ± 0.02	`EXOFASTv2`, MIST
$M_{\rm p}$ [$M_\oplus$][a]	7.5±0.9	`EXOFASTv2`, MIST, K
RV Semi-Amplitude K [m/s]	2.8 ± 0.3	`EXOFASTv2`, RVs from [36]
$a/R_\star$	24.2 ± 0.7	`EXOFASTv2`
$R_{\rm p}$ [$R_\oplus$]	2.12±0.06	Transit Depth, Interferometric $R_\star$
$\rho_{\rm p}$ [g cm^{-3}]	3.7 ± 0.5	Transit Derived $R_{\rm p}$, $M_{\rm p}$
$T_{\rm Eq}$[K]	751 ± 12	`EXOFASTv2`, $a/R_\star$, $T_{\rm eff}$
Stellar and Planetary Properties from Transit Observables — § 4.4.3		
$\rho_\star$ [g cm^{-3}]	3.1 ± 0.3	Transit Observed Properties
$M_\star$ [$M_\odot$][a]	0.85 ± 0.08	Interferometric $R_\star$, Transit Derived $\rho_\star$
$\log(g)$ [cgs]	4.64±0.04	Interferometric $R_\star$, Transit Derived $\rho_\star$
Corr($R_\star$, $M_\star$)	0.41	
$M_{\rm p}$ [$M_\oplus$][a]	8.3±1.1	Transit Derived $M_\star(\rho_\star, R_\star)$ and K
$\rho_{\rm p}$ [g cm^{-3}]	4.8 ± 0.7	Transit Derived $M_{\rm p}$, $R_{\rm p}$
Corr($R_{\rm p}$, $M_{\rm p}$)	0.09	

[a]The table reflects the computed mass of the star and planet with two different methods. See § 4.4 for more details.

Chapter 5.
LIGERS Survey Methods

5.1 Observational Methods

The observations for this survey were carried out between 2008 and 2021 at the Georgia State University CHARA Array. A summary of the observations is presented in Table B.1.

All data taken in this survey were obtained using the near-IR Classic beam combiner [117]. The Classic beam combiner uses only two of the six telescopes, and operates in either the H or K' bandpass. With the largest baseline and shortest operational wavelength, the theoretical angular resolution of the interferometer is $\theta = \dfrac{\lambda}{2B} \simeq 0.5$ mas.

Astronomical interferometry measures visibilities (V). These visibilities quantify the contrast of the dark and bright portions of the interference fringe pattern created when the optical path-length of the telescopes has been equalized. The power of the dark and light parts of the fringe pattern are integrated and time averaged and reported as a single visibility for each observation of a star.

The observation sequence used is one target star with different calibration stars observed before and after (in a sequence of calibrator 1 - science target - calibrator 2). Such a sequence is typically referred to as a bracket.

The data recorded at the time of observing contains instrumental and atmospheric noise. The calibrator stars provide a measurement of this noise and allow us to measure and correct these effects on the science target. This is possible because the calibrators are of a known, and preferably unresolved, size. Stars with a known size have predictable visibilities; the offset from which the observed and predicted visibilities differ allow correction of the science target.

Calibrator stars for this work were gathered from the JMMC Stellar Diameter Catalog version 2[1] [25, 38]. I restrict our choice of calibrator stars to stars within $\sim 15\,\mathrm{deg}$ of the target star. Stars further away may travel through substantially different pockets of air (in regard to coherence length and turbulence) which can complicate the estimation of atmospheric effects. I also eliminate stars of known multiplicity or rapid rotation ($V \sin i \gtrsim 100$ km/s). A final selection preference is given to stars with comparable color and brightness. A summary of the calibrators used in this research is presented in Table B.3.

Classic observations consist of approximately 2.5 minutes of integration in either bandpass with shutter sequences on either side. The raw Classic data are reduced with the *REDFLUOR* package to produce instrumental visibilities. The instrumental visibilities are then organized and calibrated with *CALIBIR*.

I chose for this work to use the mean power spectrum with bootstrap error estimation as the visibilty estimator[2]. This technique for computing the visibilities produces more realistic uncertainties than fitting various distributions directly to the visibilities and also produces usable results from lower signal-to-noise data. I also used the linear fit calibration method which incorporates all observations of each calibrator in measuring the atmospheric and instrumental effects rather than just the nearest two calibrators. The differences in the

[1] `http://www.jmmc.fr/catalogue_jsdc.htm`

[2] `https://www.chara.gsu.edu/tutorials/classic-data-reduction`

visibility estimations, calibration, and its effects on the fit will be discussed in the following section § 5.2.

5.2 Data Reduction and Calibration

Throughout the process of reducing the fringe scans and calibrating the raw visibilities numerous non-trivial choices are made in handling the data. The two programs used to accomplish the task of reduction and calibration are respectively *REDFLUOR* and *CALIBIR*. In this section, I will explain the choices made for the M dwarf survey.

After the observations have been concluded, the beam combiner produces a file containing all of the raw scans from the camera. Depending on the camera and observational settings, some saturation may be present in the data. The solution is to truncate the signals when saturation appears. As the Classic beam combiner has two separate output channels due to the design of the interferometer, the truncation point may differ depending on the quality of the beam alignment. If the difference in saturation point for the two outputs is small, I adopt the shorter scan length for both outputs as the truncation point. If the difference is much larger, then the rest of the analysis for that observation uses the output with the longest non-saturated scan length.

The saturation cleaned data are then scrubbed of scans where the fringe has been lost. This occurs due to target loss, tip-tilt alignment issues, poor atmospheric conditions, loss of delay to equalize the optical path length, or vibrations in the telescope and optics. Large amounts of bad or empty scans can indicate poor data quality and may increase the visibility uncertainty or require removing the observation altogether.

Before calculating the visibilities, the two outputs are scrutinized for signal quality throughout the observation. Occasionally, the alignment of one or both of the outputs will drift and the signal to noise ratio will consequently decline. Experiences over time with the CHARA Array indicate the the first output of the Classic instrument typically maintains the highest throughput and data quality, though where the throughput is good for both signals the difference signal is used to estimate visibilities.

Now the visibility is measured from the remaining cleaned scans. The scans themselves are a time domain signal which theoretically contain the visibilities. However, the fringe signal is buried behind numerous error sources. The predominant error sources come from scintillation, detector noise, and photon noise. As is frequently the case with time domain signal analysis, the problem is easier to solve in the frequency domain. The utility of the frequency domain problem is that as the noise sources are uncorrelated with the fringe signal, they simply can be subtracted from the power spectrum before computing the fringe power. The noise estimation comes from the off-star shutter sequences and dark sequence. The shutter sequences give a measurement of the power spectrum from the detector in the absence of the fringe, which should only be the noise sources. After subtracting the noise from the power spectrum, a low pass filter is applied to suppress DC noise in the background estimation and the top-hat filtered fringe power is integrated yielding the visibility.

The mathematics and theory of what the interferometer produces and what is calculated has already been discussed, but as with all measurements, there is some degree of freedom in what number is finally reported. Historically, the preferred method of calculating visibilities has shifted. Early results of CHARA, such as Berger et al. [11], had a preference for reporting

the mean and standard deviation of the measured visibility distribution from the scans. This choice implies Gaussian behavior in the errors, which is a strong assumption in the complex system of the interferometer. Larger surveys later on used the log-normal distribution to measure the nominal value and error, though this method makes similar assumptions about the data [18].

I report the mean and standard deviation determined via bootstrapping of the data scans. In the context of this survey, the most important difference in the mean power spectrum (PS) estimator is its agnostic approach to the underlying distribution of the data[3]. The mean power spectrum method generates 1000 realizations of the data scans through bootstrap sampling with replacement and measures the visibility from the mean power spectrum of the synthesized scan sequence.

Figure 5.1 shows one night of observations taken on GJ 752A. The data have been reduced and calibrated using the same settings in *REDFLUOR* and *CALIBIR*, with the only difference being the choice of visibility estimator. The two sets of visibilities have a systematic offset, but are all within 2σ tension of each other. Notably, the fit statistic for the Mean PS fit is better than that of the Log Normal. This is due to the more robust estimation of the noise via the power spectrum bootstrapping. The resultant uniform disk diameter fits initially appear inconsistent with each other, but the uncertainty in the fit is underestimated. Once the complete set of observations are added, the inter-night scatter increases the uncertainty in the fit and improves the consistency.

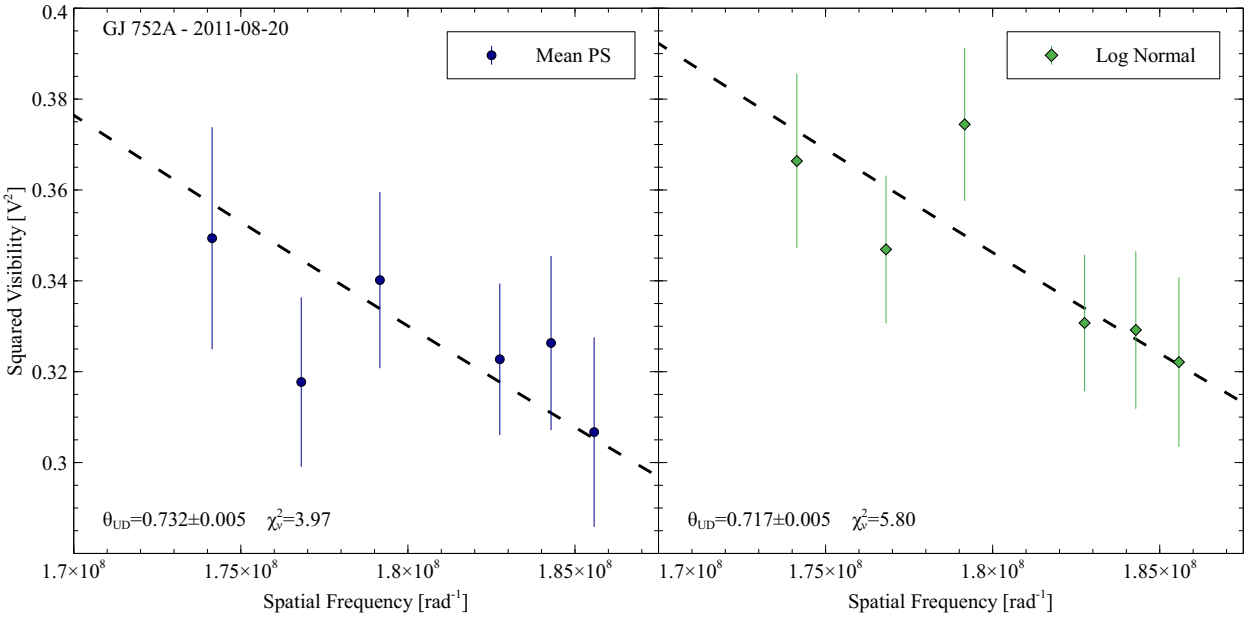

Figure 5.1. Reduction of one night of observations of GJ 752A using two different visibility estimators. Left is the Mean PS estimator and right is the Log Normal estimator.

The final data reduction step before model fitting is to calibrate the visibilities to remove

[3]The full motivation and details of the changes made to *REDFLUOR* is available in the appropriate technical report `https://www.chara.gsu.edu/files/chara_technical_reports/tr98.pdf`

instrumental and atmospheric systematic effects. The observation sequence has calibrator stars observed before and after the science target. The calibrator stars are of known size, ideally unresolved, which translates to having known visibilities. *CALIBIR* fits a trendline to the calibrators to estimate the systematic offset in the visibilities at the time the target was observed. The proportionality of the predicted calibrator visibility to the known visibility is a measure of the transfer function of the atmosphere and optical system. This scaling factor is then applied to the target to correct it. During this process we also calibrate our calibrators against each other. This provides a test to the goodness of the calibrator and is useful in determining potential binary or rotationally oblate calibrators.

Chapter 6.
LIGERS Survey Results

The LIGERS survey represents the largest single survey of low-mass stellar angular diameters in a decade. Within the survey targets, there are stars in the survey representing spectral sub-classes which have never before been measured via interferometry. Interferometrically measured angular diameters provide important benchmarks for establishing empirical relationships to stellar properties as well as putting critical tests on stellar evolutionary models. M dwarfs are the most common type of star in the universe. As such, accurate measurements and techniques for inferring M dwarf stellar parameters are critical. This chapter presents the analysis and results pertaining solely to the interferometric survey.

6.1 Angular Diameter Fitting

As was discussed in § 2.3, there is a relationship which can be used to extract the angular diameter of the star from the visibilities. As this survey deals only with stars with circular cross sections, the calibrated squared visibilities V^2 can be fit to the 1-dimensional profile of the 2-dimensional Fourier pair of the uniform or limb darkened disk. The resulting profile, Eq. 2.15, is a function of the projected baseline B, observational wavelength λ, and most importantly the angular size of the object, θ [54].

My fitting process begins with the uniform disk diameter, $\theta_{\rm UD}$, and then iterating on the limb-darkened disk, $\theta_{\rm LD}$. For each star, we combine all of the night's data into a combined dataset. We then bootstrap many thousands of realizations of the data and find the optimized uniform disk diameter using the *Scipy* least squares solver [65].

In order to fit the limb-darkened diameter, first I estimate the limb darkening coefficient μ_λ using the Limb Darkening Toolkit (LDTK) [97, 58]. I provide LDTK with samples of effective temperature, surface gravity, and metal abundance taken on normal distributions.

The stellar effective temperatures are computed from the bolometric flux using the uniform disk diameter with the modified form of the Stefan Boltzmann Law shown in Eq. 6.1. In the modified equation, the angular diameter is in units of milli-arcseconds and the bolometric flux in units of 10^{-8} erg s^{-1} cm^{-2} . Where possible, we adopt the bolometric flux measured from flux calibrated spectro-photometry in Mann et al. [83]. The uncertainties on the fluxes were inflated by 2% in quadrature to account for the floor in zero-point and filter profile calibration [15, 84]. For stars that do not have measurements in [83], I apply the same paper's bolometric correction relation to literature photometry and derive the absolute bolometric magnitude of the star. From there, the bolometric flux and luminosity are derived using the Gaia parallax. The adopted value and source of the bolometric flux are shown in Table 6.1

$$T_{\rm eff} = 2341 \cdot \left(\frac{F_{\rm bol}}{\theta^2}\right)^{1/4} \ {\rm K}, \tag{6.1}$$

The surface gravity, $g = GM/R^2$, values were found using the mass estimate from the Mass-Radius relationship developed in Mann et al. [83] and the physical radius derived from the parallax and uniform disk diameter. I assumed a 10% uncertainty on the estimated masses, which correlates to an uncertainty of 0.05 dex for $log(g)$.

I adopted a uniform estimation of 0.03 ± 0.01 for total metal abundance Z. I then inflate the uncertainty in the modeled μ_λ by a factor of 5, as the uncertainty on the resultant distributions of μ seemed unrealistic compared to Claret & Bloemen [28]. As the angular diameter's dependence on μ is fairly small for this range of limb darkening coefficient [54], these approximations and error inflation bear no large effect on the fit of the limb darkened diameter.

Using the sampled limb darkening coefficients I then fit the data for the limb-darkened diameter in the same way as the uniform disk diameter. We iterate the fitting process for the limb-darkened diameter due to the temperature dependence of the limb darkening coefficient. We scale the uncertainties to force the reduced chi-square to unity. This carries the assumption that there is no better model for the visibilities than the uniform or limb-darkened disk. We inspect the fringes and power spectrum to rule out binarity and rapid rotation, this assumption is reasonable. The final results of the fitting process are presented in Table 6.1. All plots of the final fits for the survey stars are shown in Figure 6.1.

Finally, we use the Gaia EDR3 parallaxes to compute the physical radius of the survey stars [44, 43, 45, 79]. Using simple trigonometry, the linear radius is $R = 107.5 \cdot \theta/p$, where θ and p, the parallax, are in units of milli-arcseconds. The radius is computed using the angular diameter and parallax sampled on normal distributions after the parallax is corrected for zero-point bias [78].

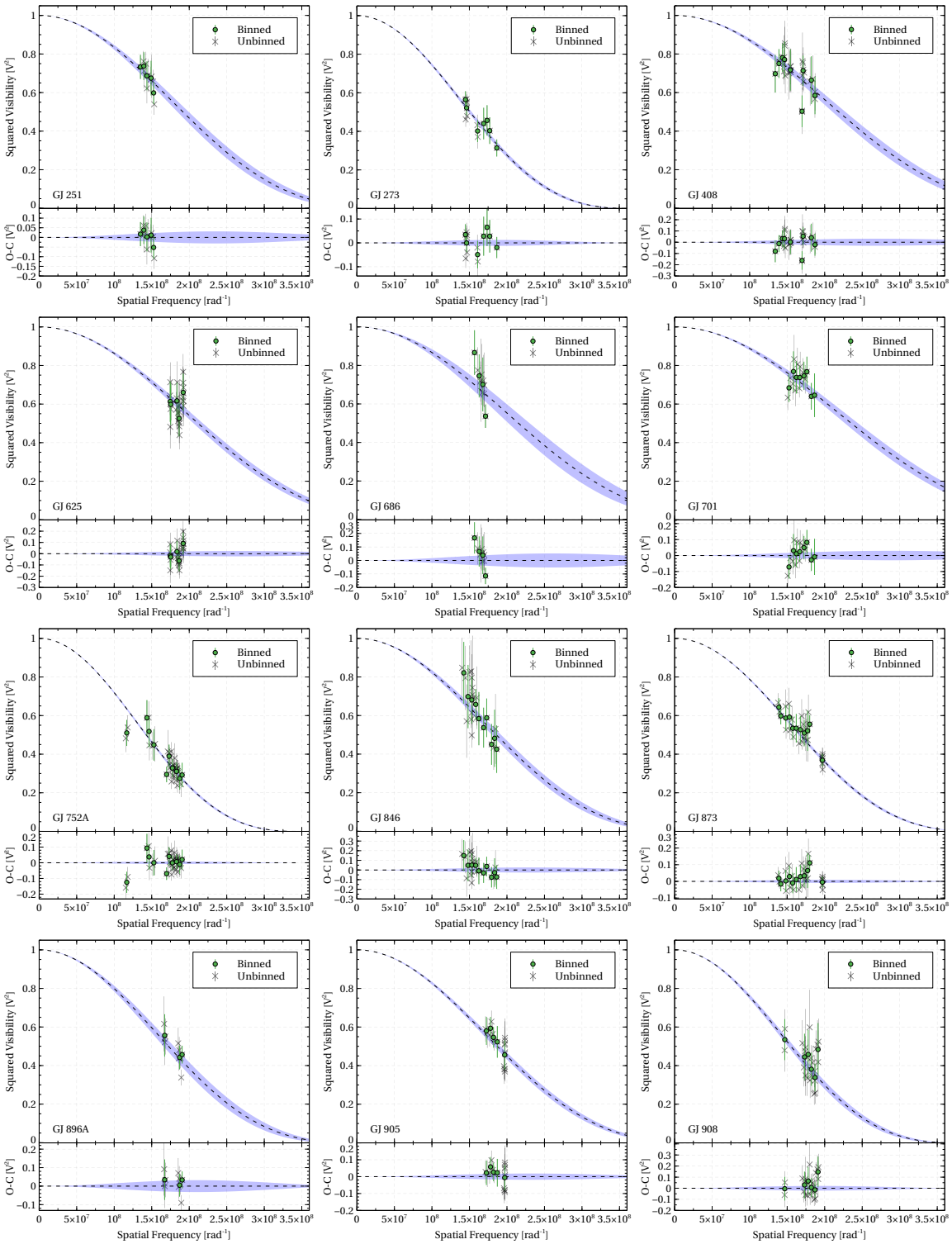

Figure 6.1. Squared visibility curves for limb darkened disks for the surveyed stars. The calibrated visibilities are shown as semi-transparent Xs. These are averaged into bins of width 5×10^6 [rad^{-1}] and overplotted as solid green circles. The best fit model is shown as a black dashed line with the blue band representing the area covered by $\pm 1\sigma$ in $\theta_{\rm LD}$. The 1σ uncertainties are also shown. Bottom panel shows the residual from the model.

Table 6.1. Summary of survey results.

Star	θ_{UD} [mas]	θ_{LD} [mas]	μ_λ	Radius [$R_\odot$]	T_{eff} [K]	L $L_\odot$	Parallax [mas] [mas]	F_{bol} $\times 10^{-8}$ [erg s^{-1} cm^{-2}]	N	χ^2_ν
GJ 49[2]	0.509 ± 0.019	0.519 ± 0.019	0.257 ± 0.011	0.550 ± 0.020	3649 ± 75	0.0213 ± 0.0006	101.391±0.017	1.59±0.06[1]	17	8.75
GJ 169[2]	0.546±0.023	0.560±0.024	0.304±0.008	0.675±0.029	4127±91	0.1191±0.0012	89.018±0.023	3.02±0.06	15	16.80
GJ 251	0.553±0.021	0.563±0.022	0.210±0.007	0.337±0.013	3545±71	0.01621±0.00014	179.015±0.028	1.67±0.05	10	4.41
GJ 273	0.707±0.013	0.720±0.013	0.2372±0.0013	0.292±0.005	3291±28	0.01070±0.00009	264.09±0.04	2.40±0.05	13	4.473
GJ 408	0.485±0.019	0.493±0.019	0.196±0.006	0.357±0.014	3603±79	0.0196±0.0007	148.153±0.025	1.38±0.06 [1]	26	11.13
GJ 625	0.501±0.014	0.509±0.015	0.2307±0.0019	0.357±0.011	3350±55	0.01442±0.00015	154.322±0.016	1.09±0.03	26	5.68
GJ 686	0.49±0.03	0.50±0.03	0.266±0.015	0.440±0.029	3602±123	0.029±0.004	122.525±0.018	1.42±0.04	10	4.73
GJ 701	0.450±0.017	0.460±0.017	0.290±0.027	0.382±0.014	3953±78	0.03190±0.00026	129.178±0.026	1.72±0.04	13	4.01
GJ 752A	0.743±0.007	0.759±0.007	0.265±0.004	0.482±0.017	3542±18	0.0330±0.0023	169.021±0.024	3.02±0.06	24	9.10
GJ 846	0.570±0.018	0.584±0.019	0.292±0.015	0.663±0.022	3544±63	0.0584±0.0005	94.52±0.05	1.79±0.05	22	14.57
GJ 873	0.634±0.007	0.647±0.007	0.2531±0.0017	0.351±0.004	3269±31	0.01263±0.00025	197.9143±0.022	1.59±0.05[1]	29	4.46
GJ 896A	0.616±0.024	0.626±0.025	0.228±0.006	0.422±0.017	3324±69	0.01942±0.00041	159.61±0.03	1.59±0.05	10	8.21
GJ 905	0.566±0.013	0.579±0.013	0.268±0.011	0.196±0.004	2872±37	0.00235±0.00006	316.43±0.04	0.76±0.03	17	5.71
GJ 908	0.684±0.018	0.696±0.018	0.2180±0.0020	0.441±0.011	3479±41	0.02626±0.00021	169.176±0.028	2.36±0.06	22	17.48

Prior to this work several of these stars had angular diameters estimated from the spectrophotometric survey of M dwarfs by Mann et al. [83]. Mann et al. [83] estimate the angular diameter using the modified form of the Stefan-Boltzmann law after flux calibrating the measurements of the spectral energy distributions. Mann et al. showed that this estimation of the angular diameter produced results with typical uncertainties of 3–4%. Two other interferometric studies have also measured diameters of LIGERS targets: Berger et al. [11] measured the diameter of GJ 752 A; and Rabus et al. [100] measured the diameter of GJ 273. All of the LIGERS stars with comparison measurements are shown in Figure 6.2

Where there are overlaps in measurements, generally the LIGERS survey sees agreement. The LIGERS diameter of GJ 273 and Rabus' measurement are equivalent. The larger discrepancy between Berger et al. [11] and my measurement of GJ 752A is tempered by the uncertainty in Berger's measurement. The tension between these two measurements is less than 2σ. All but two stars (GJ 701 and GJ 908) agree within 2σ of Mann's diameters. Mann estimated GJ 701's angular diameter as 0.5518 ± 0.0253 mas, which has 3.5σ tension with the LIGERS measurement. This level of discrepancy is surprising given the expected accuracy of the other Mann estimated diameters. Follow up on more and longer baselines would provide further insight, as the observations only sampled to $V^2 \sim 0.8$. However, the data appear good and internally consistent. Mann's measurement of GJ 908 is comparatively in closer agreement with the LIGERS survey. The Mann diameter of GJ 908, 0.6336 ± 0.0211 mas has a tension of 2.2σ. The observations of GJ 908 star had some nights in poor seeing which may have contributed to the discrepancy.

6.2 An Anomalous Detection

In the course of the survey, we uncovered two stars with behavior incongruous with a single star solution. As was discussed in § 2.3, the van Cittert-Zernike theorem allows transforming *any* arbitrary distribution of light on the sky to the corresponding visibility distribution in the UV plane. Any change to the shape or number of stars produces different visibility patterns. After careful reduction and analysis, the data weakly favor a binary star model for GJ 49.

GJ 49 is an early M dwarf (M1.5V [3]). In 2019, GJ 49 was found to be the host of a super-Earth planet [98]. Super-Earths are a type of planet with radii of 1–4 $R_\oplus$ and masses of 1–10 $M_\oplus$ [21]. As is discussed further in § 4, super-Earths are interesting as they do not exist within the solar system and must be contextualized solely as exoplanets. The importance of a well constrained stellar diameter is invaluable for characterizing the super-Earth.

Unfortunately, the interferometric data are not consistent with a single star for GJ 49. Unlike the visbility curves of single stars which quickly decay after the first null, binary star visibility curves null multiple times with lobe spacing indicative of the separation between the sources. Figure 6.3 shows visibility curves for lab fringes for synthetic stars at various separations [59].

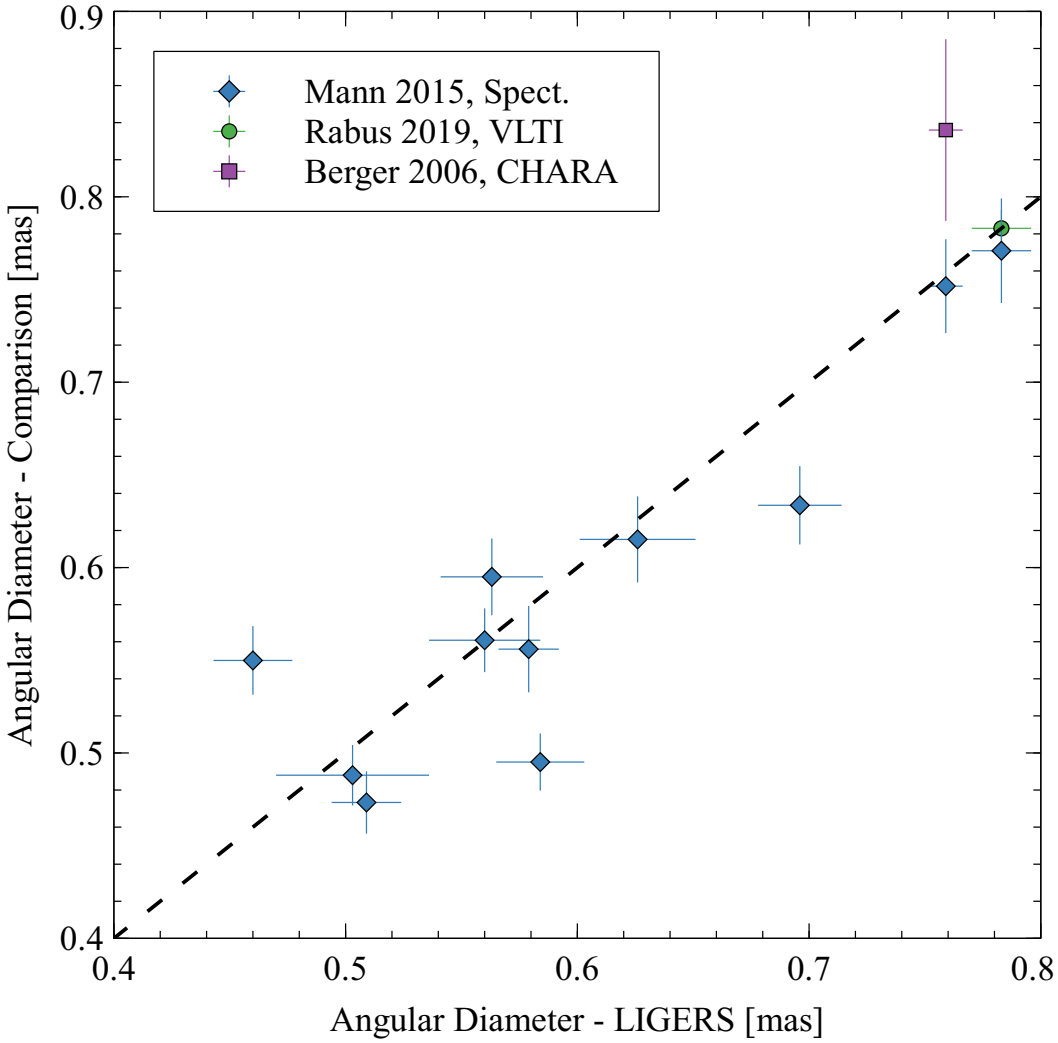

Figure 6.2. Comparison of LIGERS survey stars to previous measurements. The x-axis is the LIGERS measured diameter and the y-axis is the comparison diameter. The uncertainties in either direction are shown. Mann et al. [83] measurements are shown as blue diamonds. The Berger et al. [11] measurement of GJ 752A is shown as a purple square. The Rabus et al. [100] measurement of GJ 273 is shown as a green circle. A one-to-one scale is shown as a dashed black line.

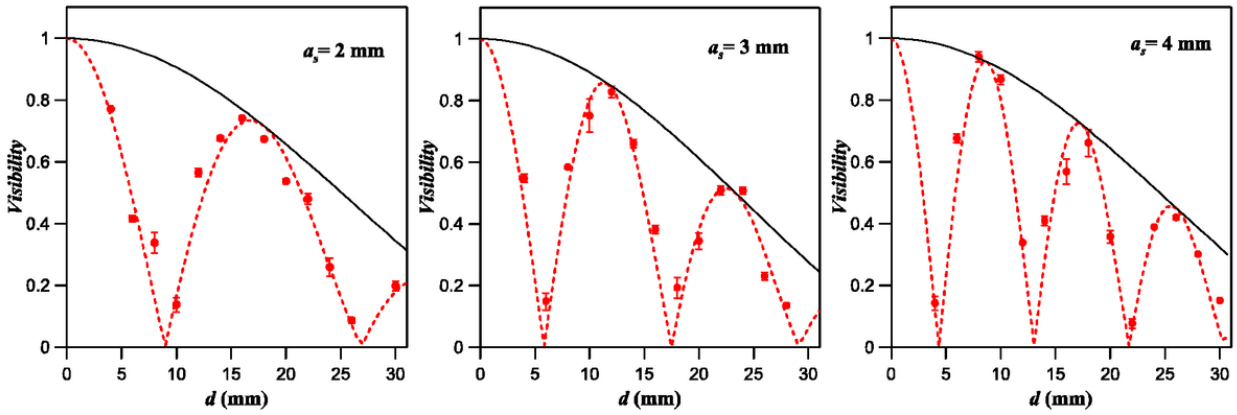

Figure 6.3. The visibility curves for single circular sources and two circular sources of various separations [60]. The solid black curve is the single source model. The dashed red curve is the binary model. Observed visibilities and errors are shown as red points. The x-axis is the separation between the two optical fibers, which is analogous to the telescope separation. Note that as the sources are further separated, the lobes squeeze together.

The data and single star fit for GJ 49 is shown in Figure 6.4. Visually, the single star fit shows a substantial disagreement with the observations. I compared a single and binary star model using the JMMC LITPro [115] interferometric data fitting software. The p-value of an F-test on the two models was inconclusive, but weakly favored the binary model *p=0.12*. The conclusion of binarity is strengthened by the observations on UT 2014-10-12. On that night, GJ 49 was observed with two different baselines. When the baselines were switched, the visibilities drastically changed (shown at spatial frequency $\sim 1.8\times10^8$). This is consistent with a binary model having different cross sectional distributions of light depending on the position angle. It is possible that the exoplanet may actually be a false positive detection due to a hitherto unresolved binary companion.

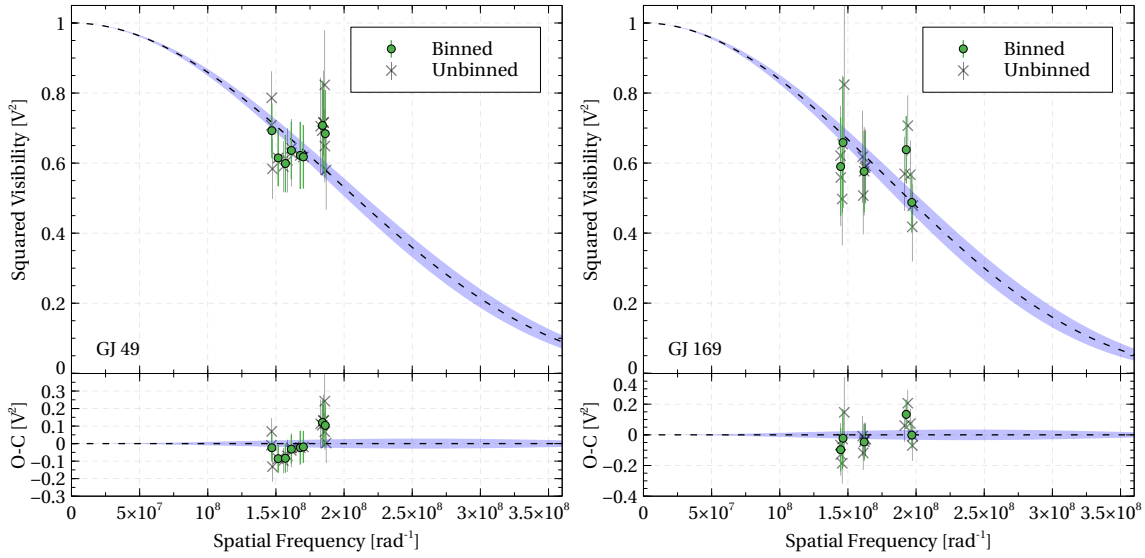

Figure 6.4. Squared visibility curve for GJ 49, left,and GJ 169, right. The calibrated visibilities are shown as semi-transparent Xs. These are averaged by spatial frequency in bins of width 5×10^6 [rad^{-1}] and overplotted as solid green circles. The best fit model is shown as a black dashed line with the blue band representing the area covered by $\pm 1\sigma$ in $\theta_{\rm LD}$. The 1σ uncertainties are also shown. Bottom panel shows the residual from the model.

Also shown in Figure 6.4 is the visibility curve for GJ 169. While not as storied as GJ 49, GJ 169 is another early M dwarf (M0.5V). The same fit and statistical tests were performed, but are less supportive of a stellar companion. This star is presented here for completeness, but is not included in the remainder of the analyses.

While this work is primarily concerned with the single stars, it is worth appreciating the rich scientific history of exploring binary star systems with long baseline optical interferometry. The power of the interferometer allows resolving close-in binaries and determining precise astrometric motions [103] as well as stellar parameters. The MIRC-X beam combiner in particular excels at binary science, even capable of surveying galactic Cephied variables for multiplicity [47]. Despite having enough data to derive an angular diameter which is consistent with surface brightness relation predictions, we would require more data to confidently classify GJ 49 and 169. As such, these stars have been removed from the survey to prevent adulterating the other high quality measurements.

6.3 Applications of Measured M Dwarf Diameters

Aside from providing high quality direct measurements of M dwarf angular diameters, bolometric fluxes, and effective temperatures the LIGERS survey will play a vital role in constraining evolutionary models. Evolutionary models systematically underestimate the stellar radius and overestimate the effective temperature. The LIGERS diameters are useful benchmarks in stellar models.

Figures 6.5, 6.6, and 6.7 show the LIGERS survey stars augmented with all stars with measured diameters less than $0.7\,{\rm R}_\odot$. The three models used are the Parsec, MIST, and

YaPSI models [19, 35, 113]. The summary of the properties of these stars is shown in Table D.1. Notably, the YaPSI models do not even probe the smallest stars studied. The Parsec and MIST models also diverge for the lowest of masses. The results from the LIGERS survey provide measurements to constrain the behavior of the stellar models for low mass stars and will help harmonize the predictions of observed stellar parameters. To compare the three models, Figure 6.8 shows the ensembles isochrones ran with solar iron abundance. For this solar abundance, the MIST provided isochrones do not probe the

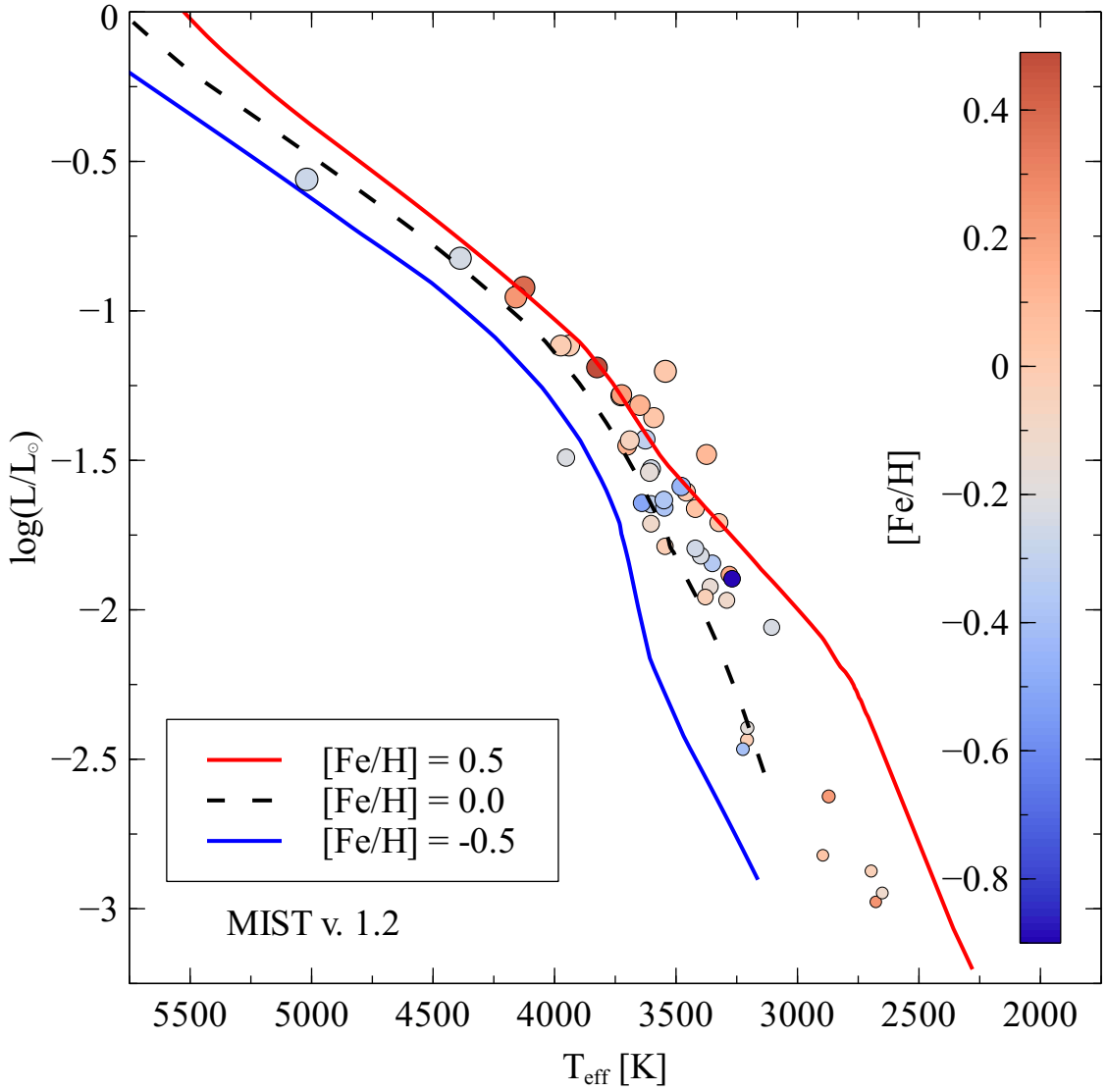

Figure 6.5. Hertzsprung-Russel diagram for MIST v. 1.2 isochrones with [Fe/H] of -0.5, 0, and 0.5. The solar iron abundance model is shown as a a dashed black line, the super-solar iron abundance model is shown as the red line above the black dashed line, and the sub-solar iron abundance is shown as the blue line below the black dashed line. The surveyed stars are shown with marker size proportional to the radius and shaded according to the iron abundance.

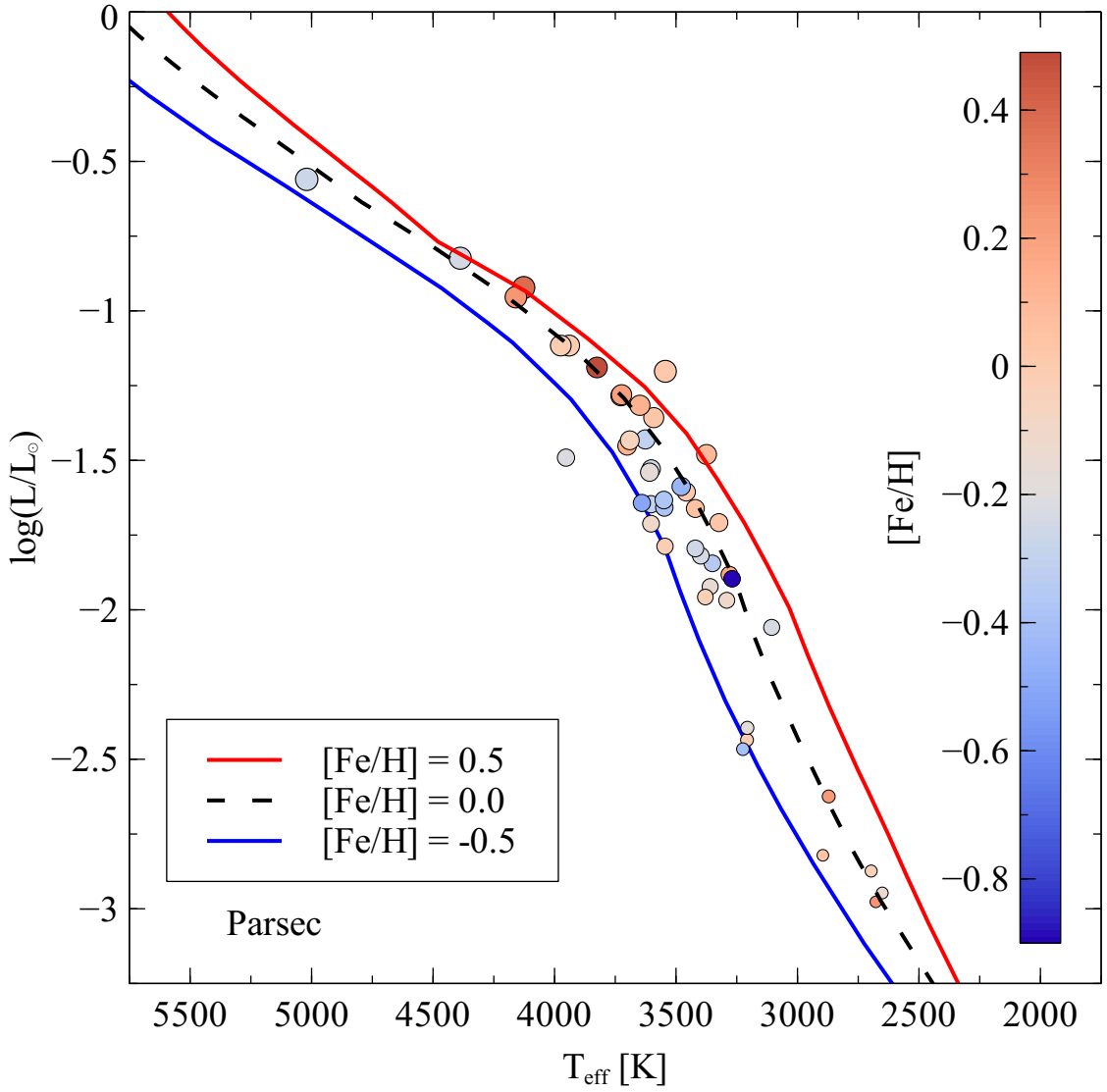

Figure 6.6. Hertzsprung-Russel diagram for Parsec isochrones with [Fe/H] of -0.5, 0, and 0.5. The solar iron abundance model is shown as a a dashed black line, the super-solar iron abundance model is shown as the red line above the black dashed line, and the sub-solar iron abundance is shown as the blue line below the black dashed line. The surveyed stars are shown with marker size proportional to the radius and shaded according to the iron abundance.

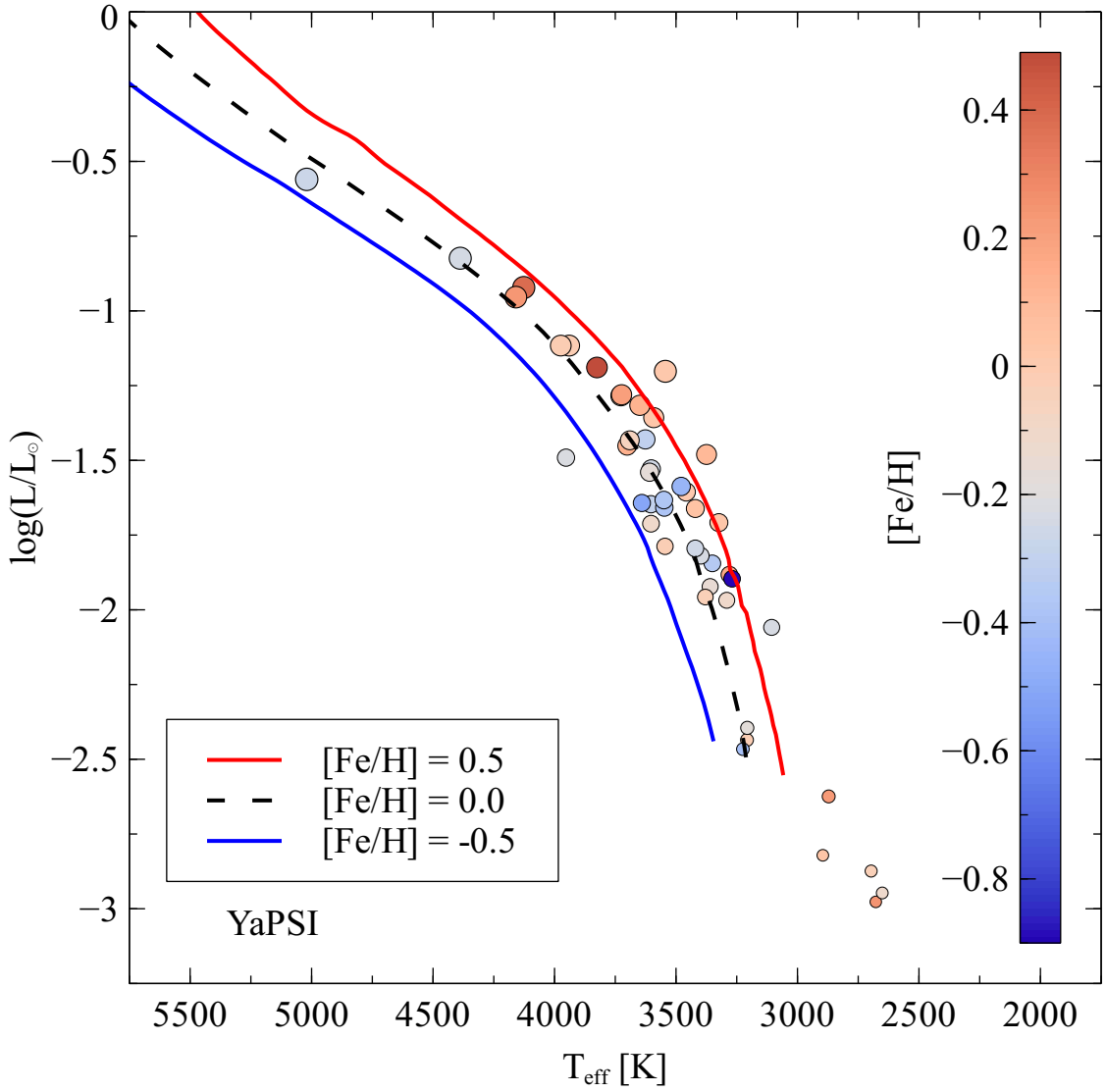

Figure 6.7. Hertzsprung-Russel diagram for YaPSI isochrones with [Fe/H] of -0.5, 0, and 0.5. The solar iron abundance model is shown as a a dashed black line, the super-solar iron abundance model is shown as the red line above the black dashed line, and the sub-solar iron abundance is shown as the blue line below the black dashed line. The surveyed stars are shown with marker size proportional to the radius and shaded according to the iron abundance.

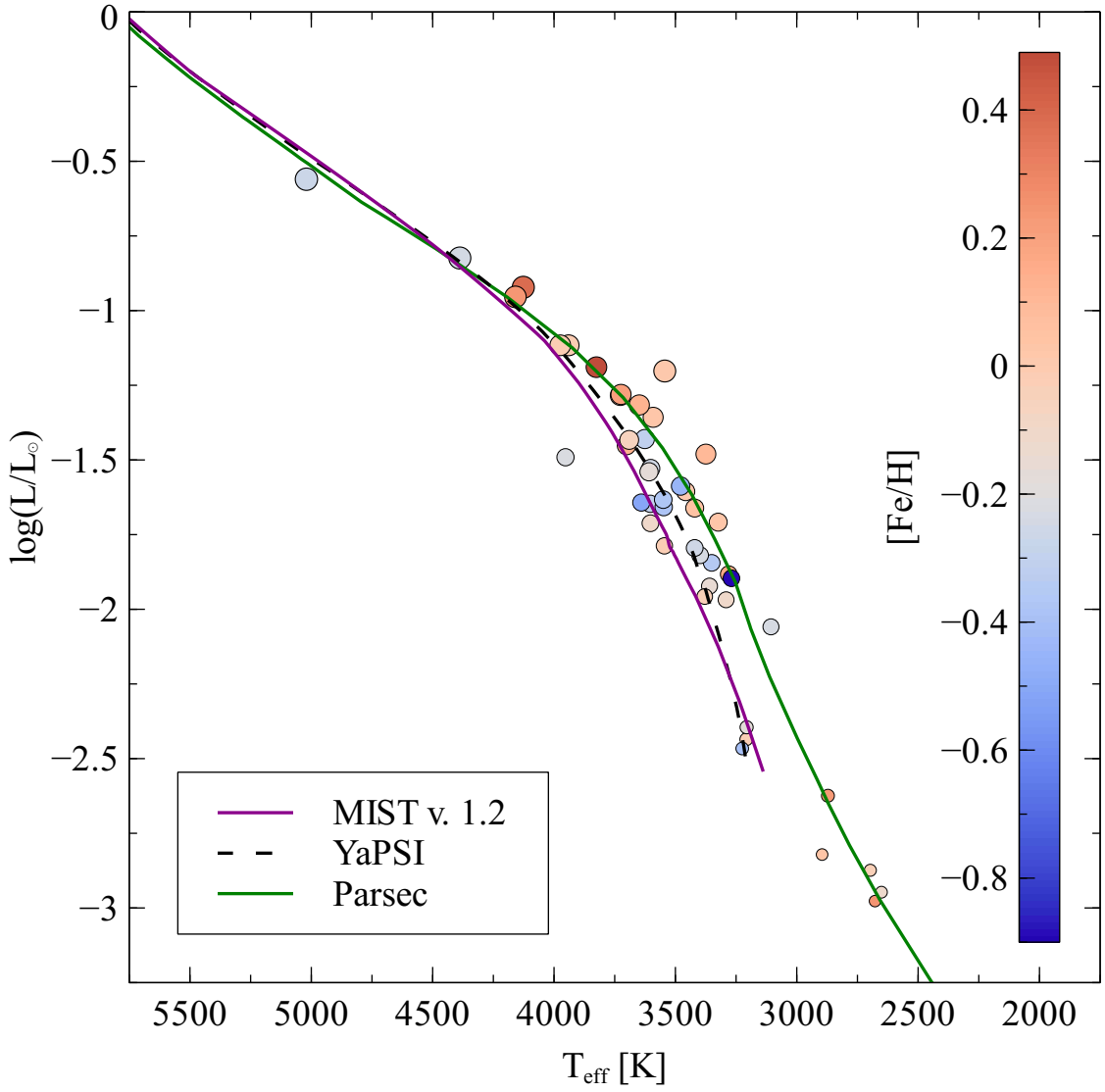

Figure 6.8. The three model isochrones ran with solar iron abundance compared to the survey sample. The smallest mass ran for the solar iron abundance model with the MIST models was $0.15\,M_\odot$, and as such does not go as cool and faint as the Parsec model, which reaches $0.1\,M_\odot$.

Chapter 7.
Surface Brightness Relations

7.1 Introduction

The second major result in this thesis is the development of new suface brightness color relations with complementing existing measurements of M dwarf angular diameters. Surface brightness relationships use easy to measure and readily available photometric magnitudes to predict stellar angular diameters. As color indices, the difference between the magnitudes in two filters, of a star are specific to each spectral class, this provides an invaluable tool for characterizing distant stars where interferometry or other measurement methods are not available.

It is worth iterating that directly measuring a stellar diameter is difficult and can only be done for a select number of stars. The three main techniques for directly probing the diameter are lunar occultation, double line eclipsing binary stars, and, of course, interferometry. While the constraints of interferometry were previously discussed in § 3, it is interesting to explore the constraints and productivity of eclipsing binaries and occultations as the motivation for surface brightness relationships.

Lunar occultation measures the stellar diameter by observing the star's brightness as the moon passes in front of the star. If the angular diameter of the star is large enough ($\gtrsim 2$ mas [33]), the star will gradually fade out. The time to full occultation paired with the angular speed of the moon provides a measure of the stars angular diameter. This is complicated by Fresnel diffraction against the lunar limb. Instead, it is possible to measure the intensity of the fringe pattern created by the diffraction and compare that to the intensity of the star before its occultation to measure the diameter. Despite the geometric constraints, lunar occultation has measured diameters for over 300 stars [1].

Observations of double lined eclipsing binaries (DEBs) also provide a direct model-free measurement of the stellar angular diameter. The requirement for the inclination angle to be very close to 90° greatly limits the number of systems that this technique can study. It is also necessary that the reflex motions from the orbit be great enough to produce measurable Doppler shifts for both stars. DEBs are of particular interest because they also provide a measure of the stellar masses as well as the diameters. The DEBcat has recorded 288 binary systems (576 individual stars) with well constrained masses and diameters [112]. Typical uncertainties on the diameters in this catalog are $\sim 2\%$.

Where the above techniques are not possible (i.e. most stars), surface brightness relations can predict stellar sizes using broadband photometry. Photometric magnitudes measure the energy emitted from a star over a discrete range of wavelengths. The difference of two different magnitudes is referred to as a color index and gives a unique characterization of a stars differential energy emission.

Wesselink [128] derived the relationship between the flux in a given filter, F_λ, is given by the effective temperature of the star, T, and the bolometric correction, BC_λ, for that filter:

$$F_\lambda = \log(T) + 0.1 BC_\lambda \tag{7.1}$$

The bolometric magnitude, M_b, of a star is found from the magnitude in a given filter,

m_λ, to the bolometric correction:

$$M_b = m_\lambda + BC_\lambda \rightarrow m_\lambda = M_b - BC_\lambda \tag{7.2}$$

The bolometric magnitude can also be expressed as:

$$M_b = -2.5 \log\left(\frac{L}{L_\odot}\right) + 4.74 \tag{7.3}$$

Where L, is the luminosity of the star, and $4.74 = M_{b,\odot}$. Substituting this into the distance modulus gives:

$$m_\lambda = M_b - BC_\lambda + 5\log(d/[pc]) - 5 \tag{7.4}$$

$$= -2.5 \log\left(\frac{L}{L_\odot}\right) + 4.74 - BC_\lambda + 5\log(d/[pc]) - 5 \tag{7.5}$$

As the Stefan-Boltzmann relationship provides a direct relationship between the luminosity and the temperature and radius, this can be substituted into Eq. 7.3 to yield:

$$= -2.5 \log\left(\frac{4\pi R^2 T^4 \sigma}{4\pi R_\odot^2 T_\odot^4 \sigma}\right) + 4.74 - BC_\lambda + 5\log(d/[pc]) - 5 \tag{7.6}$$

Employing the properties of logarithms allows the above to be rewritten as:

$$= 5\log\left(\frac{d}{R[pc]}\right) - 10\log(T) + [5\log(R_\odot) + 10\log(T_\odot) - 0.26] - BC_\lambda \tag{7.7}$$

As $\theta = 2R/d$, the above can be rewritten to include the angular diameter:

$$= -5\log(\theta) - 10\log(T) + \left[5\log(R_\odot) + 10\log(T_\odot) - 0.26 + 5\log\left(\frac{2[pc]}{R_\odot}\right)\right] - BC_\lambda \tag{7.8}$$

Now substituting in Eq. 7.1, the effective temperature of the star can be eliminated. Also, at this time, all the constants inside the square brackets will be collapsed into a constant C:

$$m_\lambda = -5\log(\theta) - 10F_\lambda + C - BC_\lambda + BC_\lambda \tag{7.9}$$

Finally, reworking this to express the flux in the given filter as a function of angular diameter and magnitude in the filter:

$$F_\lambda = -0.5\log(\theta) - 0.1 m_\lambda + C \tag{7.10}$$

$$= -0.5\log(\theta) - 0.1 m_\lambda + 4.2207 \tag{7.11}$$

Where C has been evaluated using the nominal solar values and IAU definitions.

The final step is to equate this expression of the flux to that from the Barnes-Evans relation, Eq. 7.12 [10]:

$$F_\lambda = \sum_i (m_X - m_Y)^i \cdot a_i \tag{7.12}$$

Where m_X and m_Y are the magnitudes in two filters. This relationship was developed by relating the bolometric flux of a star from the Stefan-Boltzmann relationship to the observed flux as defined by the magnitude system. Solving the expression after the substitution for $\log(\theta)$ gives the fit for surface brightness relations used in this chapter:

$$\log(\theta) = \sum_i (m_X - m_Y)^i \cdot a_i - 0.2 m_X \tag{7.13}$$

a_i here are numerical constants, which I fit for in this analysis. Barnes & Evans [10] originally used only two coefficients (i.e. a linear relationship) to connect the color index and the flux, though any number of terms may be included. Boyajian et al. [17], for example, found that a quadratic term was necessary when considering giants in some filters. Some filters showed statistically significant improvement when considering cubic or quartic terms.

7.2 Results

For the surface brightness relations, I augmented the LIGERS stars with all published K and M dwarfs with physical radii less than 0.7 $R_\odot$. The limb darkened diameter measurements were sourced from the JMMC measured diameter catalog [39]. After applying the cut on diameter, 46 stars with high quality diameter measurements remained. The average uncertainty in angular diameter for the selection of stars is 2.2% with a max uncertainty of 6.6%. The uncertainty in angular diameter is the predominant source of scatter in the surface brightness relations as the photometric uncertainties are typically $\sim 1\%$.

There exist dozens of different photometric systems each with their advantages and applications. For this work, I chose to use the Johnson *V*, Gaia *G*, Johnson-Cousins R_C and I_C, and 2MASS *J, H,* and K_S. The Johnson and Johnson-Cousins filters are some of the most ubiquitous and widely used standard filters. It was necessary in some cases to convert Johnson *R* and *I* filters to the Johnson-Cousins equivalents [81]. The Gaia *G* was chosen as it is frequently used in microlensing studies, though its inclusion posed some concerns. As all of the stars selected are nearby, there is a very real potential for saturation with the space-based Gaia telescope. Though the release notes for the Gaia data releases have addressed this, in the course of this work, I took extra care to handle Gaia saturation. Lastly, the 2MASS magnitudes are included because the inclusion of an infrared bandpass greatly improves the quality of the surface brightness relations. Unfortunately, much like Gaia, these stars frequently encounter saturation issues. There exist well characterized color transformations from Johnson *J, H, K* magnitudes to 2MASS magnitudes, which circumvents the problem [22]. Table 7.1 summarizes the chosen filters' effective wavelength and filter width.

The majority of the photometry used came from Mann et al. [83]. Mann cataloged flux calibrated spectrophotometry in the optical and infrared from SNIFS and SpeX instruments for 183 M stars. These spectra were then integrated with the desired filter profiles to generate synthetic photometry with exquisite precision. Accounting for zero-point correction and filter profile uncertainties, the resultant fluxes are thought to be accurate at the 2% level. About $2/3^{\text{rds}}$ of the stars used in this study have synthetic photometry available. The uncertainties for the synthetic magnitude ranged from 0.02–0.03 mag.

As was acknowledged by Mann, the synthetic Gaia photometry may have a systematic offset depending on how the telescope behaves once calibrated *in-situ*. Indeed, I observed

Table 7.1. Basic information for the photometric filters used for the development of surface brightness relations. All information was gathered from the SVO Filter Profile Service[1]

Filter	$\lambda_{\rm eff}$ [nm]	$\Delta\lambda$ [nm]
V	551	88
G	585	437
R_C	635	107
I_C	880	289
J	1235	215
H	1662	261
K_S	2152	278

an average discrepancy between the catalog Gaia magnitudes and the synthetic, averaging a difference of 0.3 mag. After correcting for Gaia's saturation effects for bright stars ($2 < G < 8$) [102], the offset persisted. Notably, the difference between the synthetic and measured was always positive, indicating that Gaia measured these stars as *brighter*. To correct for systematic effects, the difference between the synthetic and Gaia photometry was fit with a simple power law and the correction was added to the synthetic Gaia magnitudes. Additional terms were added to the fit until the reduced chi-square, $\chi^2_{\nu=31} = 7.66$, was minimized. I suggest a quadratic transformation from the Mann, et al. Gaia magnitudes of:

$$G_{\rm real} = 0.0006G^2_{\rm Mann} + 0.9638G_{\rm Mann} - 0.0251 \tag{7.14}$$

For the remainder of the stars for which we do not have synthetic photometry, I sourced literature photometry from a multitude of sources. The full set of data used for the surface brightness relations is available in Table E.1.

The fitting process for the surface brightness relations begins by sampling the photometry and the angular diameters on a normal distribution with the reported uncertainties. The zero-point angular diameter is then computed as:

$$\log(\theta_{m_x=0}) = \log(\,\theta_{\rm LD}) + 0.2m_x \tag{7.15}$$

Where m_x is the apparent magnitude in the shorter wavelength of the color index. Then polynomials of the form:

$$\log(\theta_{m_x=0}) = \sum_i (m_x - m_y)^i \cdot a_i \tag{7.16}$$

are fit to the zero-point angular diameters as a function of the color index $(m_x - m_y)$ and coefficients a_i. To determine the appropriateness of additional terms, the Akaike information criterion (AIC) was computed until the criterion reached a minimum value [2]. The AIC when corrected for small sample size is defined as:

$$AIC = \chi^2 + 2p + \frac{2p(p+1)}{(N-p-1)} \tag{7.17}$$

where χ^2 is the sum of squared residuals divided by the squared uncertainties, p is the number of fit parameters, and N is the number of data points. The AIC statistic is lower when the

fit and data are in better agreement, but penalizes over-fitting. The coefficients of each fit and the fit statistics are summarized in Table 7.2. The data and best fit relation for the twelve different color indices chosen are shown in Figures 7.1, 7.2, and 7.3.

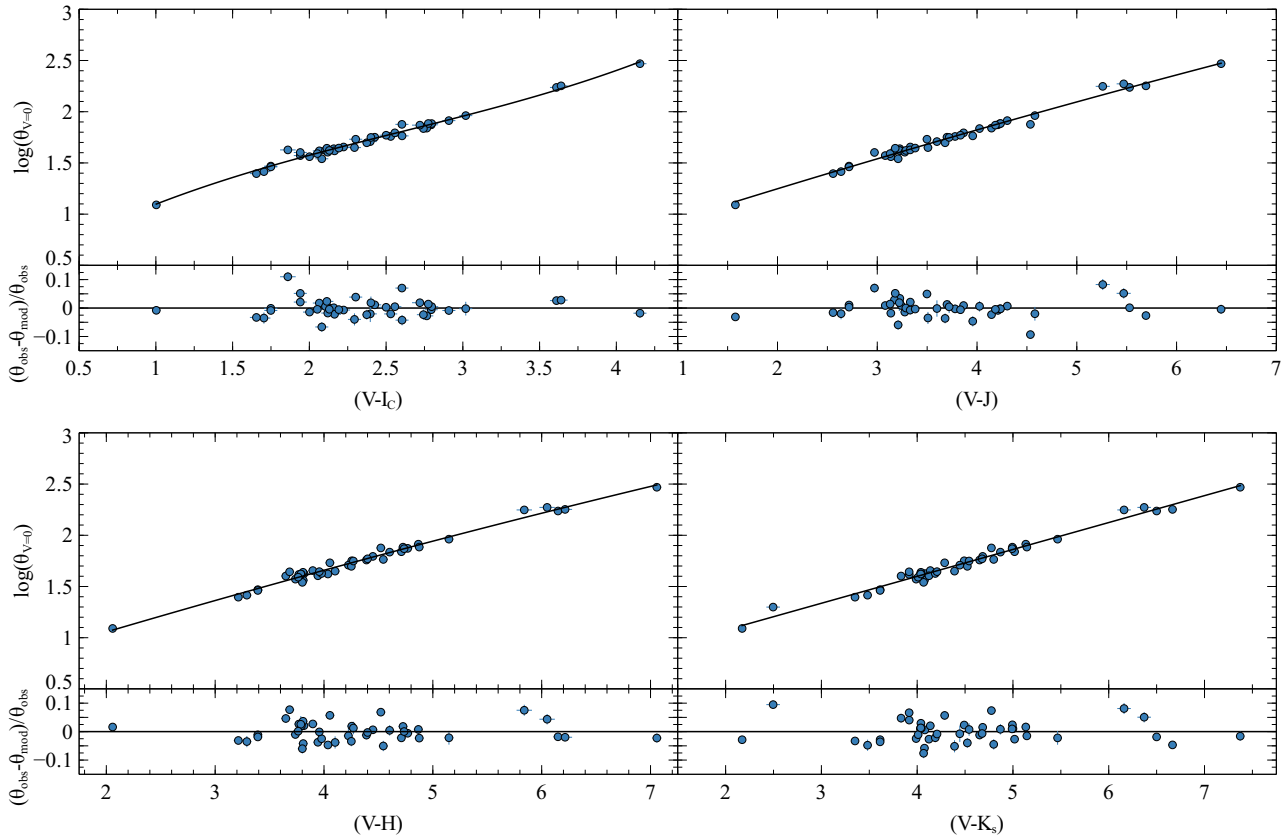

Figure 7.1. Surface brightness color relations for four color indices. All relations use V as the reference wavelength. Top left: $(V - I_C)$, top right: $(V - J)$, bottom left: $(V - H)$, and bottom right: $(V - K_S)$. The observed data zero-magnitude diameters are shown as blue points with vertical and horizontal errors, though the errors are often smaller than the marker size. The best fit polynomial model is shown as a solid black line over the color range of the avaialable data.

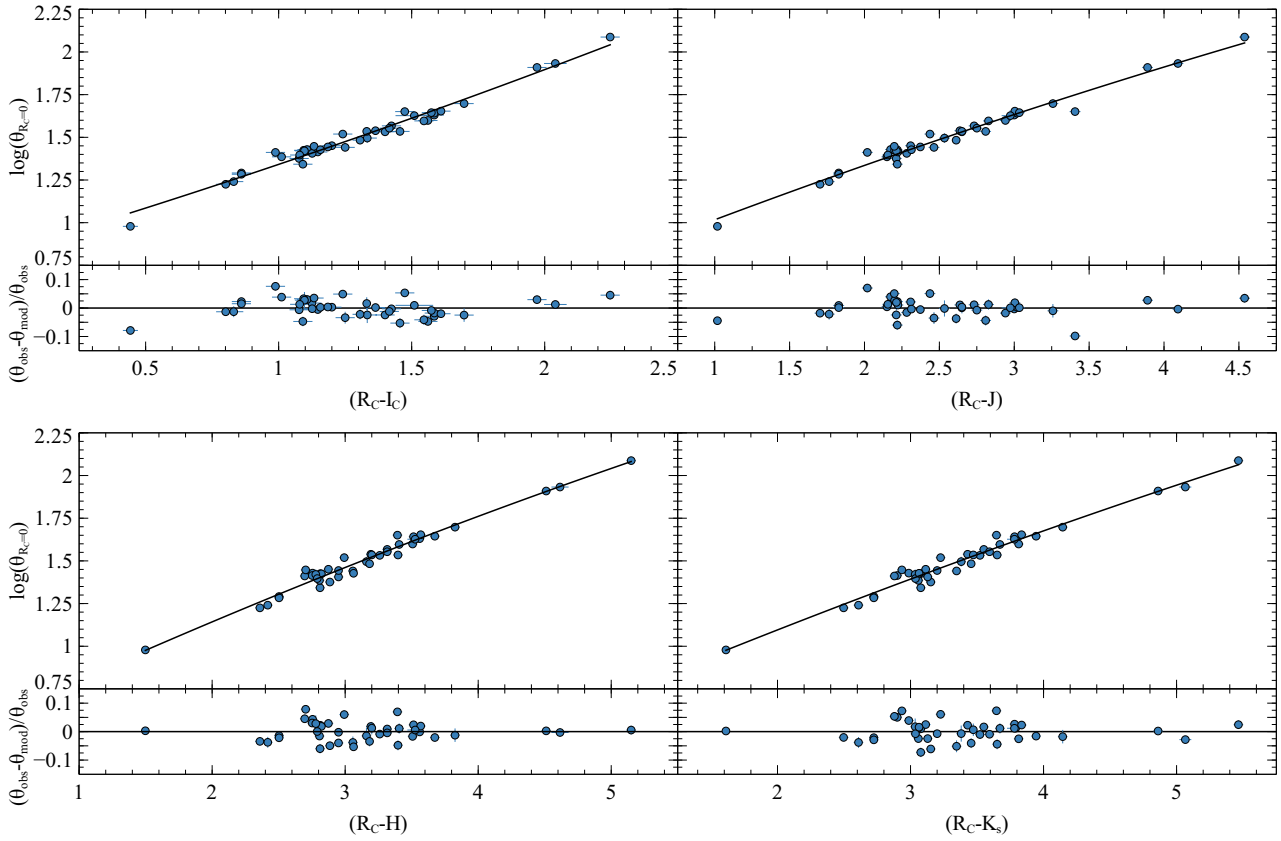

Figure 7.2. Surface brightness color relations for four color indices. All relations use R_C as the reference wavelength. Top left: $(R_C - I_C)$, top right: $(R_C - J)$, bottom left: $(R_C - H)$, and bottom right: $(R_C - K_S)$. The observed data zero-magnitude diameters are shown as blue points with vertical and horizontal errors, though the errors are often smaller than the marker size. The best fit polynomial model is shown as a solid black line over the color range of the avaialable data.

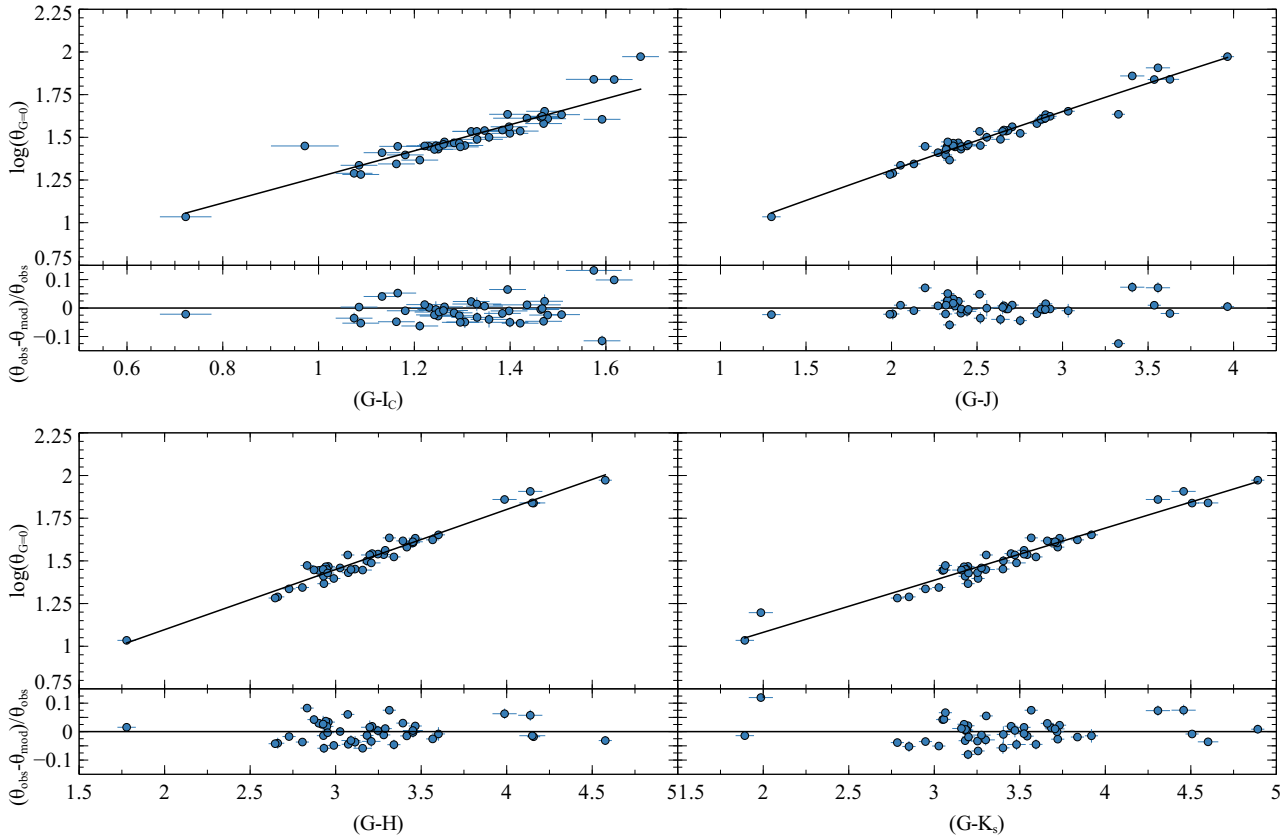

Figure 7.3. Surface brightness color relations for four color indices. All relations use G as the reference wavelength. Top left: $(G - I_C)$, top right: $(G - J)$, bottom left: $(G - H)$, and bottom right: $(G - K_S)$. The observed data zero-magnitude diameters are shown as blue points with vertical and horizontal errors, though the errors are often smaller than the marker size. The best fit polynomial model is shown as a solid black line over the color range of the avaialable data.

Table 7.2. The coefficients for twelve different surface brightness relationships are shown here. The order of the polynomial was determined as described in § 7.2. The range denotes the strictly inclusive extent of the color index for which the relationship is good. These models should not be extrapolated outside the range. For all of these relations, the first (i.e. shortest wavelength) filter in the index is used as the zero-magnitude reference filter.

Color Index	Range	a_0	σ_{a_0}	a_1	σ_{a_1}	a_2	σ_{a_2}	a_3	σ_{a_3}	RMS [dex]	RMS [%]	χ^2_ν	N
$(V - I_C)$	[0.82–4.15]	0.36	0.08	0.91	0.10	-0.21	0.04	0.027	0.006	0.03	4.91	7.0	43
$(V - J)$	[1.48–6.45]	0.635	0.023	0.316	0.012	-0.0048	0.0015	···	···	0.03	5.10	9.2	45
$(V - H)$	[1.89–7.06]	0.409	0.029	0.335	0.013	-0.0057	0.0015	···	···	0.03	6.18	8.2	45
$(V - K_S)$	[1.94–7.37]	0.548	0.010	0.2627	0.0022	···	···	···	···	0.04	7.01	14.2	46
$(G - I_C)$	[0.64–1.57]	0.504	0.043	0.764	0.033	···	···	···	···	0.06	9.07	24.6	43
$(G - J)$	[1.29–3.81]	0.426	0.025	0.496	0.021	-0.027	0.004	···	···	0.03	6.03	10.5	45
$(G - H)$	[1.7–4.42]	0.400	0.011	0.354	0.004	···	···	···	···	0.03	6.46	14.1	45
$(G - K_S)$	[1.75–4.74]	0.471	0.015	0.31	0.06	···	···	···	···	0.04	7.44	18.6	46
$(R_C - I_C)$	[0.37–2.25]	0.844	0.025	0.47	0.04	0.029	0.014	···	···	0.03	5.82	16.1	42
$(R_C - J)$	[1.02–4.54]	0.679	0.021	0.349	0.015	-0.0101	0.0028	···	···	0.03	5.69	13.7	42
$(R_C - H)$	[1.44–5.15]	0.448	0.029	0.366	0.018	-0.0095	0.0028	···	···	0.03	5.83	22.2	42
$(R_C - K_S)$	[1.49–5.46]	0.456	0.028	0.335	0.016	-0.0075	0.0022	···	···	0.03	6.18	17.0	42

The surface brightness relations demonstrate the ability to accurately predict angular diameters for stars based on the most ubiquitous photometric systems. On average, the relationships developed allow predicting angular diameters with 6% accuracy. Notably, the relationship for $(G - I_C)$ has larger dispersion than the others. This is likely because of the narrow color range and substantial wavelength overlap of the filters.

I compare the $(V - I_C)$ model shown in Figure 7.4 to models developed by Kervella et al. [68] and Boyajian et al. [17]. The early work of Kervella et al. [68] included many angular diameters measured at the CHARA Array, as well as other interferometers, in the development of their surface brightness relations. These relationships were developed with 42 stars over a $(V - I_C)$ range of -0.02–2.78 mag. The Boyajian et al. [17] added new M dwarfs to Kervella, et al. , but also imposed a 5% angular diameter uncertainty constraint and as such used 34 stars over the same color range. Looking at the overlap in color, there is a scatter of 5.6% when applying the Kervella, et al. relation for the $(V - I_C)$ index to the dataset used in this work compared to the 4.8% of my model. The inclusion of the reddest stars in the sample necessitated cubic terms in the surface brightness relation.

Boyajian et al. [17] developed the first surface brightness relationships which included a substantial number of main sequence K and M dwarfs. This work was an important extension and improvement to the prior work of Kervella, et al. which inlcuded only three M dwarfs, compared to Boyajian, et al. with over twenty. Boyajian's model like mine contains a cubic term and has a scatter of 5.7%. As was noted by Kervella et al. [68], surface brightness relations should not be extrapolated much beyond the color range used in the calibration. As interferometric surveys such as this thesis are carried out, new surface brightness relations must be developed to predict diameters for the reddest stars. This is evident when erroneously extrapolating the Boyajian, et al. model to the most red stars used in Figure 7.4. Figures 7.5, 7.6, and 7.7 compare models from Kervella et al. [68] and Boyajian et al. [17] for the other indices using the Johnson V. The models developed here represent an extension 1.5 mag redder for $(V - I_C)$, 2.5 mag for $(V - J)$, 2 mag for $(V - H)$, and 2.5 mag for $(V - K_S)$.

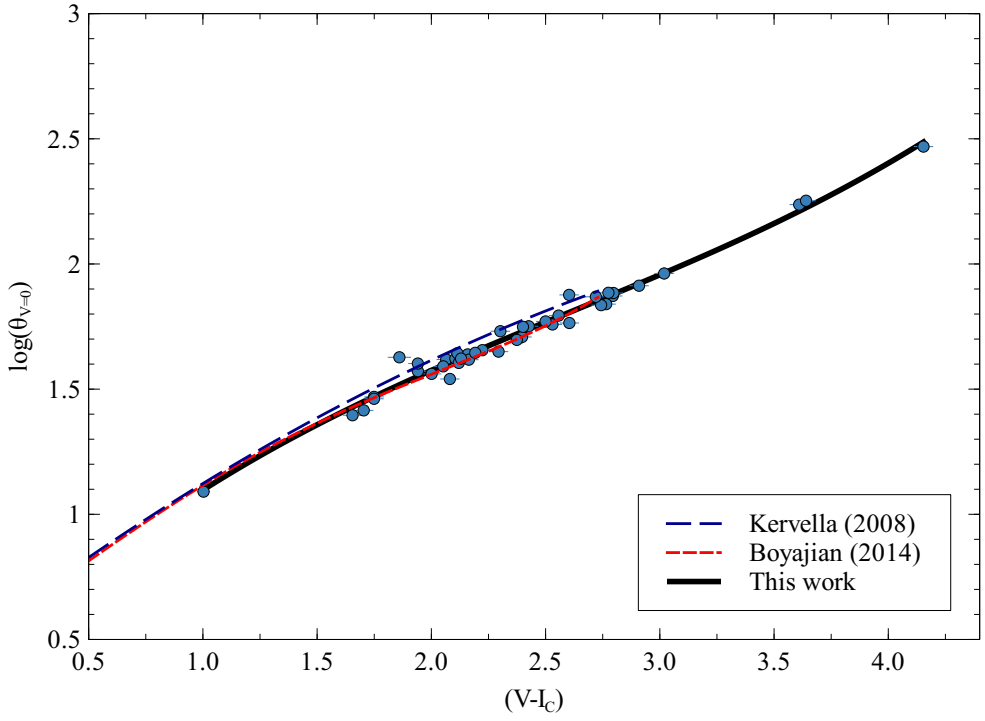

Figure 7.4. Comparison of three different surface brightness relations for the $(V - I_C)$ color index. The relation developed in this work is shown as a solid black line, the Boyajian et al. [17] mopdel is shown as a red dashed line, and Kervella et al. [68] is shown as a large dashed blue line.

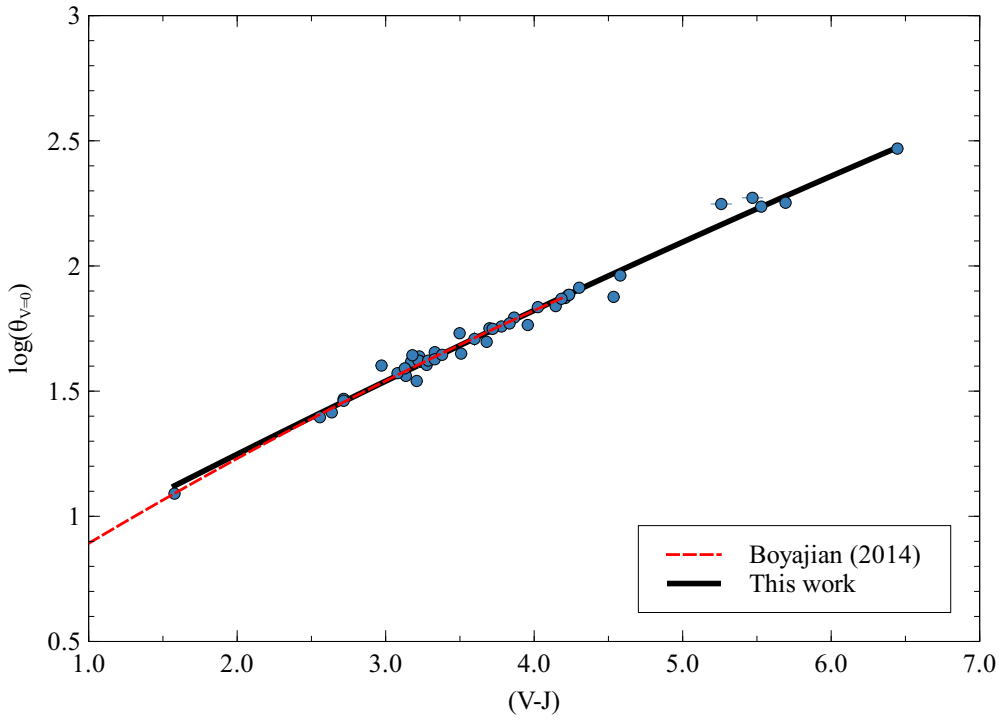

Figure 7.5. Comparison of two different surface brightness relations for the $(V - J)$ color index. The relation developed in this work is shown as a solid black line and the Boyajian et al. [17] model is shown as a red dashed small dashed line.

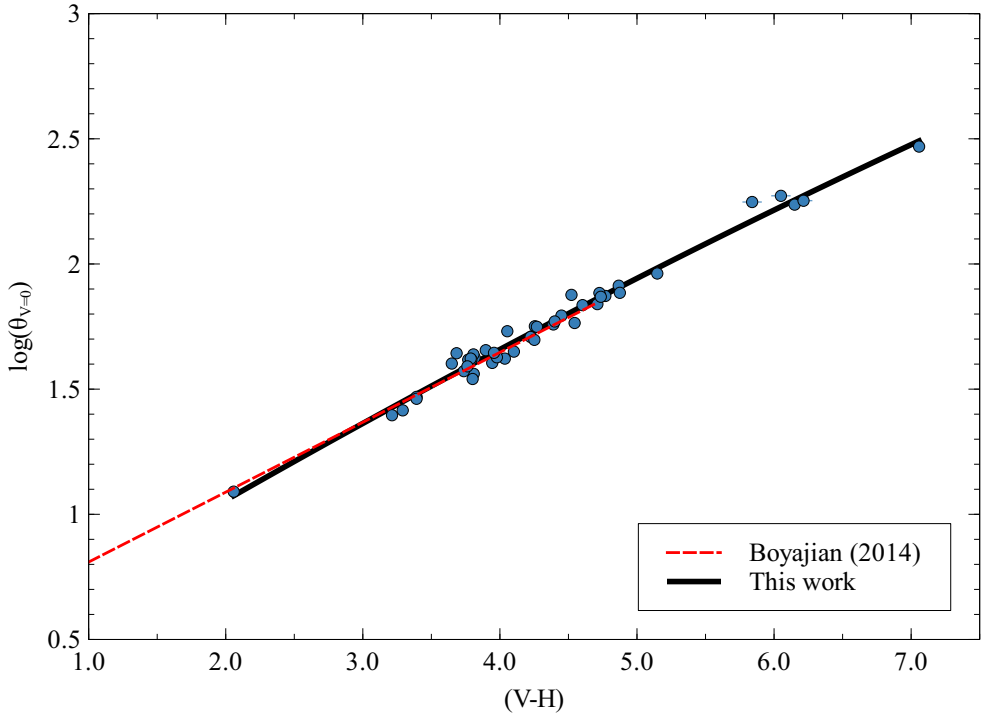

Figure 7.6. Comparison of two different surface brightness relations for the $(V - H)$ color index. The relation developed in this work is shown as a solid black line, the Boyajian et al. [17] model is shown as a red dashed small dashed line.

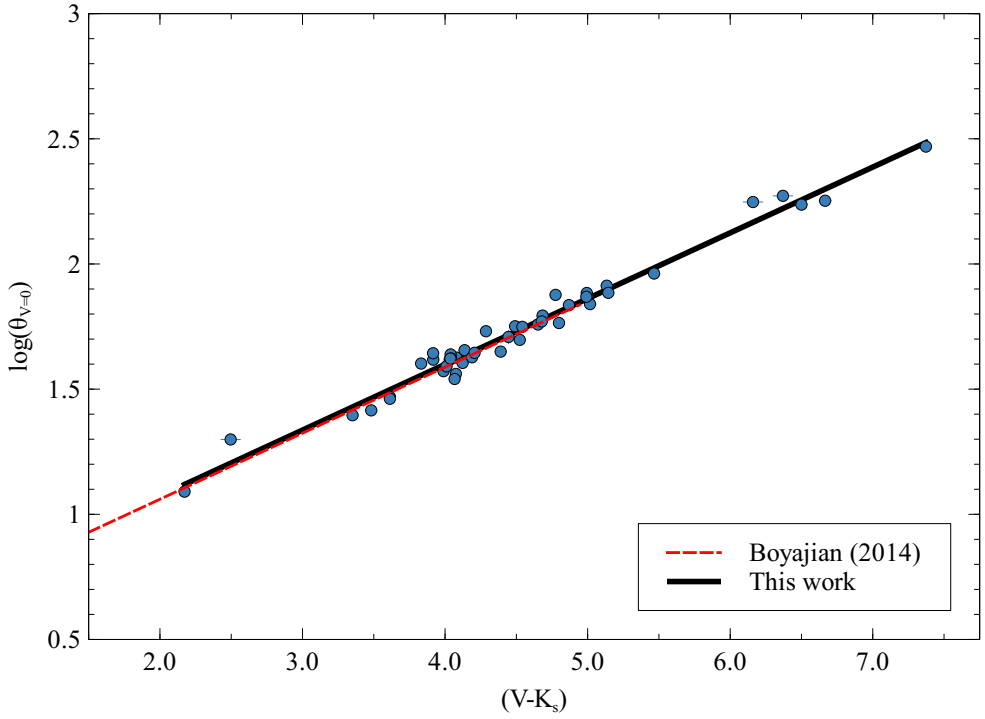

Figure 7.7. Comparison of two different surface brightness relations for the $(V - K_S)$ color index. The relation developed in this work is shown as a solid black line, the Boyajian et al. [17] is shown as a red dashed small dashed line.

Previous works developing surface brightness relations note the importance of separating main sequence stars from evolved stars [68, 17, 104]. Though evolved stars and main sequence stars may overlap in their color index, the underlying physics and nature of energy transport within the star differ and as such must be separated. Salsi et al. [104] generated a series of relationships in the $(V - K_S)$ index for both M dwarfs and giants. As can be seen in Figure 7.8, the slopes of the relations diverge for giants and dwarfs. The surface brightness relations developed in this work extend the $(V - K_S)$ relationship 0.5 mag redder and several magnitudes bluer than the work of Salsi et al. [104], an important step for estimating the sizes of the smallest M dwarfs.

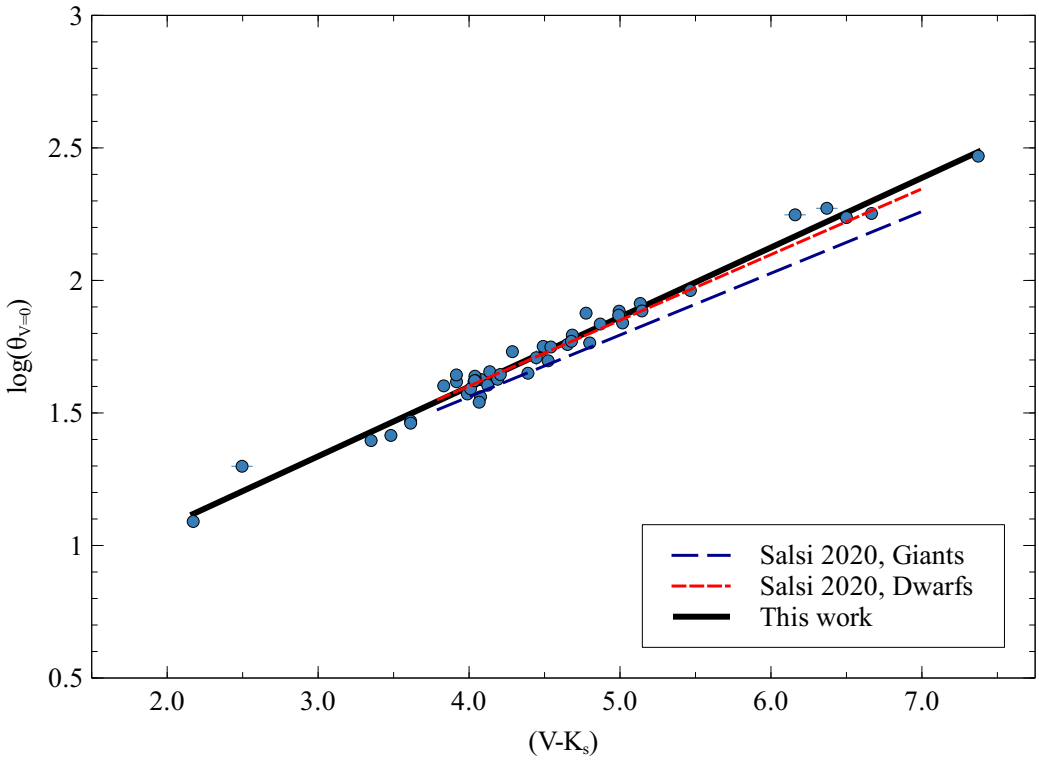

Figure 7.8. Comparison of surface brightness relations from Salsi et al. [104] for M dwarfs and giants. The relation developed in this work is shown as a black line, the giant relation is shown as a blue dotted line and the dwarf relationship is shown as a red dashed line.

Chapter 8.
Conclusion

An underlying thread throughout this work is the significant role that interferometry plays in the fundamental parameters of stars, but also in exoplanet science. Interferometry gives access to one of the most intrinsic properties of the star: its radius. The stellar radius is the key to estimating some of the most important properties of exoplanets and their host stars.

The hunt for an Earth sized planet with an Earth-like climate is limited by the difficulty of inferring planetary properties in relation to the host star. In this thesis, I measured the angular diameters of 14 M dwarfs using the CHARA interferometric array. Earth sized planets are most likely to be detected around M dwarf stars, due to the relative size of the planet to the star. The great precision of the survey measurements will help in this search.

In the process of the survey, my collaborators and I also made a highly precise measurement of the angular diameter of HD 97658. This star was of particular interest as it is a super-Earth planet host. We were also able to test the agreement between two of the visibile light beam combiners at the CHARA Array. The results our study of HD 97658 are direct measurements of two of the most fundamental properties of a star: its radius and bolometric flux. We also produced estimations of the stellar effective temperature and physical radius. All of these properties combine allowed us to further constrain the properties of its host star.

The surface brightness color relations are likely the most widely useful product from this research. While the angular diameters themselves are useful benchmarks and invaluable in characterizing the individual systems, the surface brightness relations allow astronomers in a breadth of sub-fields to accurately estimate stellar diameters. In particular, exoplanets detected from gravitational lensing benefit from a robust and accurate diameter estimation method. The relations developed in this work extend to redder (lower mass) stars than any previously developed.

Previous studies have implicated the interplay of stellar magnetic activity and convection on the discrepancy between observed and predicted stellar radii. The stars measured in this survey will allow further exploration of the lowest mass regime in evolutionary models and hopefully harmonize the predictions with observations.

The completion of this thesis and this survey is a great accomplishment for me as well as for the interferometry group at LSU. We are providing the wider astronomy community with the largest single publication of M dwarf diameters in over a decade and a variety of surface brightness relations for exploring stellar systems much further away. We hope that these results may one day help characterize an Earth-like exoplanet continuing interferometry's great history with exoplanet science.

Appendix A.
Summary of Baselines Available at the CHARA Array

The available baselines have been taken from the GSU CHARA web page. The resolution has been derived with Eq. 2.2 assuming operation in the H band. It is possible to characterize stellar diameters below this resolution; the resolution limit produces square visibilities of $V^2 \simeq 0.5$.

Table A.1. All possible baselines and the corresponding resolutions in the H band for the CHARA array.

Baseline	**Length [m]**	**Resolution [mas]**
E1-S1	330.66	0.52
W1-E1	313.53	0.55
E1-S2	302.33	0.57
E2-S1	278.76	0.62
W1-S1	278.5	0.62
W1-E2	251.34	0.69
W1-S2	249.39	0.69
E2-S2	248.13	0.7
W2-E1	221.82	0.78
W2-S1	210.97	0.82
W2-S2	177.45	0.97
W2-E2	156.27	1.1
W2-W1	107.92	1.6
E2-E1	65.88	2.62
S2-S1	34.07	5.06

Appendix B.
LIGERS Survey Observation Log and Calibrator Stars

Table B.1. Summary of observations of the stars in this survey. See Table A.1 for a description of the available baselines as well as the maximum baseline for the chosen telescopes. Each bracket corresponds to one target data point taken before data sanitation. Further details of the observations and data are in § 5.1.

Target	UT Date	Calibrators	Baseline	Bandpass	Brackets
GJ49	2014-08-18	HD3801, HD6795	E1-W1	H	5
	2014-10-12	HD6795, HD3801	E1-W1	H	2
	2014-10-12	HD6795, HD3801	S1-E1	H	6
	2019-11-25	HD4841, HD7284	E1-W1	H	1
	2019-11-25	HD4841, HD7284	E1-W1	K'	2
	2021-08-22	HD4841, HD7284	S1-W1	H	1
	2021-09-03	HD4841, HD7284	S2-E1	H	2
GJ169	2013-08-22	HD27429, HD28677, HD31362	E1-S1	H	5
	2013-10-02	HD27429, HD28677	E2-S1	H	5
	2021-03-07	HD28527	S2-W1	H	1
	2021-08-25	HD27533, HD26571	S1-W1	H	4
	2021-09-02	HD27309, HD26571	E1-S2	H	1
GJ251	2008-09-17	HD52711	E1-S1	K'	1
	2017-12-02	HD47100, HD56124	E1-W1	K'	4
	2018-01-24	HD56124	E1-S1	K'	5
GJ273	2009-12-01	HD57006, HD60111	E1-W1	K'	8
	2010-04-08	HD60111	E1-S1	H	3
	2017-10-29	HD52913, HD65900	E1-S1	H	3
	2019-11-25	HD52913	E1-W1	H	1
GJ408	2014-03-19	HD96418, HD97658	E1-W1	H	4
	2014-03-21	HD96418, HD97658	E1-W1	H	2
	2014-04-21	HD96418, HD97658	E1-W1	H	3
	2014-04-24	HD96418, HD97658	S2-E1	H	5
	2017-12-01	HD96738, HD95242	E1-S1	K'	2
	2018-01-23	HD95242, HD96738	E1-W1	K'	5
	2018-01-24	HD95242, HD96738	E1-W1	K'	5
GJ625	2010-06-28	HD149650	E1-W1	H	4
	2010-06-29	HD149105, HD149650	E1-W1	H	2
	2011-08-16	HD149105, HD149650	E1-S1	H	8
	2011-08-19	HD149105, HD149650	E1-W1	H	4
	2011-08-20	HD149105, HD149650	E1-W1	H	6
	2011-08-21	HD149105	E1-W1	H	2
GJ686	2014-04-21	HD158806, HD159063	E1-S2	H	3

Table continued

Target	UT Date	Calibrators	Baseline	Bandpass	Brackets
	2014-08-13	HD159063	E1-S2	H	5
	2021-08-22	HD157740	S1-W1	H	3
GJ701	2014-04-21	HD161606, HD165610	S2-E1	H	1
	2014-04-24	HD161606, HD165610	S2-E1	H	6
	2014-08-13	HD163976, HD165610	S2-E1	H	4
	2014-08-16	HD163976, HD165610	E1-W1	H	2
GJ752A	2011-08-17	HD176095, HD180482	E1-S1	H	1
	2011-08-17	HD176095, HD180482	E1-S1	H	1
	2011-08-18	HD180482, HD182101	E1-S1	H	5
	2011-08-19	HD176095, HD182101	E1-W1	H	6
	2011-08-20	HD176095, HD180482	E1-W1	H	6
	2019-04-15	HD179491, HD180945	E1-S1	K'	2
	2020-08-25	HD180945	E2-S1	H	3
	2021-05-05	HD179491, HD180945	S1-W1	K'	2
	2021-09-02	HD180482	E1-S1	H	1
GJ846	2013-08-18	HD205924, HD207202	S1-W1	H	2
	2013-08-20	HD205924, HD207202	S1-E1	H	4
	2013-08-21	HD205924, HD207202	S1-E1	H	6
	2020-08-23	HD205924, HD208632	E1-W1	K'	2
	2020-08-25	HD205924, HD208632, HD208703	E2-S1	H	3
	2021-08-26	HD208632, HD209875	S1-W1	H	3
	2021-08-27	HD208632, HD209875	S1-E1	H	3
	2021-09-02	HD208632, HD209875	S2-E1	H	1
GJ873	2008-10-24	HD218470	E1-W1	K'	3
	2010-09-17	HD218470	E1-W1	H-750 Hz	3
	2010-09-17	HD2123360	E1-W1	H-1000 Hz	5
	2010-09-18	HD213660, HD211211	E1-W1	H	5
	2010-09-20	HD211211	E1-S1	H	8
	2014-08-15	HD218949,SAO34852	E1W1	H	6
GJ896A	2011-10-03	HD221627, HD220952	E1-S1	H	6
	2014-08-14	HD221627, HD220952	E1-S2	H	4
GJ905	2012-08-23	HD222556, HD222642	E1-S1	H	5
	2012-08-24	HD222556, HD222642	E1-W1	H	6
	2013-08-21	HD220885, HD222304	E1-W1	H	1
	2014-10-13	HD219306, HD218525	E1-S1	H	5
GJ908	2010-06-30	HD221356	S1-E1	H	3
	2010-09-18	HD221356	E1-W1	H	7
	2010-09-19	HD216735, HD221356	E1-S1	H	10
	2019-11-25	HD223438	E1-W1	K'	2

Table B.3. Summary of calibrators used in this work. These properties are taken from the JMMC Stellar Diameter Catalog v. II. The full catalog is available in Vizier table II/346/jsdc_v2. The uniform disk diameter is estimated from surface brightness relationships. The full description of calibrators is described in § 5.1. Note that the K magnitude listed here is 2MASS K_S and not the K' of CHARA.

Star	**Spectral Type**	***V Mag***	***H Mag***	K_S **Mag**	$\theta_{\mathbf{UD}}$
HD3801	F8	7	5.7	5.6	0.3184±0.0086
HD4841	B5Ia	6.9	5.4	5.2	0.2589±0.0078
HD6795	F2	6.7	5.6	5.6	0.3146±0.0086
HD7284	F5	7.2	6	5.9	0.2698±0.0062
HD17309	K0III	7.2	5	4.9	0.5121±0.0111
HD26571	B8III	6.1	5.6	5.6	0.2409±0.007
HD27309	A0sp	5.3	5.6	5.6	0.2365±0.0066
HD27429	F2Vn	6.1	5.2	5.2	0.3722±0.0089
HD27533	F8	7.1	5.7	5.6	0.3192±0.0078
HD28527	A6IV	4.8	4.7	4.4	0.441±0.0341
HD28677	F4V	6	5.2	5.1	0.3748±0.0089
HD31362	F0	6.3	5.5	5.4	0.326±0.0079
HD47100	B8III	5.3	5.5	5.4	0.2432±0.0075
HD50296	G	10.8	9.2	9.2	0.0664±0.0015
HD52913	A3Vs	6	5.6	5.6	0.2645±0.0073
HD52711	G0V	5.9	4.6	4.5	0.5271±0.0476
HD56124	G0	6.9	5.5	5.4	0.3528±0.0082
HD57006	F8IV	5.9	4.8	4.7	0.4837±0.016
HD60111	F0/2IV/V	5.6	5	4.8	0.4229±0.0247
HD65900	A1V	5.7	5.7	5.6	0.2462±0.0067
HD95242	K1III	7.3	4.8	4.7	0.5743±0.0127
HD96418	F8IV	6.9	5.6	5.6	0.3174±0.0087
HD96738	A0IV	5.7	5.4	5.4	0.2685±0.0074
HD97658	K1V	7.8	5.8	5.7	0.3531±0.0078
HD143549	B3III	7.7	8	8	0.058±0.0023
HD146254	A0III	6.1	5.7	5.7	0.2405±0.0066
HD149105	G0V	7	5.6	5.5	0.3412±0.0097
HD149650	A2V	5.9	5.8	5.8	0.2364±0.0064
HD149013	F8V	7	5.8	5.8	0.2921±0.009
HD153229	F3IV/V	6.5	5.6	5.6	0.3076±0.0095
HD157740	A3V	5.8	5.6	5.5	0.2758±0.0074
HD157935	F5III	6.6	5.7	5.7	0.2988±0.0069
HD158806	F6IV	6.9	5.7	5.7	0.3029±0.0071
HD159063	G0V	7	5.8	5.7	0.3012±0.007
HD161606	A8V	8.6	7.7	7.7	0.1136±0.0033
HD163976	F8III	7.4	6	6	0.2692±0.0063

Table continued

Star	**Spectral Type**	***V Mag***	***H Mag***	K_S **Mag**	$\theta_{\mathbf{UD}}$
HD165610	F5/6V	7	5.8	5.8	0.2918±0.0078
HD176095	F5IV	6.2	5.2	5	0.3972±0.01
HD179491	F8	7.5	5.6	5.5	0.3438±0.0084
HD180482	A1V	5.6	5.3	5.2	0.3002±0.0087
HD180945	F5V	7.2	6.1	6	0.2583±0.0062
HD182101	F6V	6.3	5.3	5.2	0.3756±0.0087
HD205924	A9IV-Vn	5.7	5.1	5	0.3775±0.01
HD207202	G8III/IV	7.6	5.4	5.3	0.4194±0.0093
HD208632	F5/6+K(III)	7.1	6	5.9	0.2741±0.0069
HD208703	F2V	6.3	5.5	5.4	0.3314±0.0089
HD209875	F6V	7.2	6	5.9	0.271±0.0063
HD211211	A2Vnn	5.7	5.7	5.7	0.2489±0.0069
HD213660	A6V	5.9	5.3	5.3	0.3227±0.0084
HD216106	G0	6.8	5.4	5.3	0.3713±0.0086
HD216735	A1V	4.9	5	4.8	0.322±0.0299
HD218172	F8IV	7.3	5.9	5.9	0.2869±0.0068
HD218470	F5V	5.7	4.7	4.6	0.487±0.0348
HD218525	A2IV	6.5	6.1	6	0.219±0.0059
HD218949	G5	7.2	5.7	5.6	0.3445±0.0079
HD219306	F5	7.5	6.2	6.1	0.2427±0.0059
HD220885	B9III	5.8	5.7	5.7	0.2216±0.006
HD220952	K1IV	7.9	5.7	5.6	0.378±0.0102
HD221356	F7V	6.5	5.3	5.2	0.3861±0.0097
HD221627	G1IV	6.8	5.4	5.3	0.383±0.0087
HD222304	B9Ve	5.4	5.4	5.4	0.2565±0.0073
HD222556	F5	6.9	5.7	5.6	0.3075±0.0075
HD222603	A7V	4.5	4.2	4.1	0.5392±0.0542
HD222642	F0	7	6.4	6.3	0.21±0.0052
HD223438	A3III	5.8	5.3	5.3	0.3009±0.0082

Appendix C.
Copyright Information

The first page of Ellis, et al. "Directly Determined Properties of HD 97658 from Interferometric Observations" 2021 AJ *162* 118 follows[1]. I assert that I am the first author of this article. The article was published with the following agreement:

When you transfer the copyright in your article to IOP, we grant back to you certain rights, including the right to include all or part of the Final Published Version of the article within any thesis or dissertation.[2]

[1]The article as published is available at `https://doi.org/10.3847/1538-3881/ac141a`

[2]The full license agreement is available at `https://journals.aas.org/article-charges-and-copyright/`

The Astronomical Journal, 162:118 (9pp), 2021 September https://doi.org/10.3847/1538-3881/ac141a

Directly Determined Properties of HD 97658 from Interferometric Observations

Tyler G. Ellis[1], Tabetha Boyajian[1], Kaspar von Braun[2], Roxanne Ligi[3], Denis Mourard[4], Diana Dragomir[5], Gail H. Schaefer[6], and Christopher D. Farrington[6]
[1] Louisiana State University 202 Nicholson Hall Baton Rouge, LA 70803; telli17@lsu.edu
[2] Lowell Observatory 1400 W. Mars Hill Road Flagstaff, AZ 86001, USA
[3] INAF-Osservatorio Astronomico di Brera Via E. Bianchi 46 I-23807 Merate, Italy
[4] Université Côte d'Azur, Observatoire de la Côte d'Azur, CNRS, Laboratoire Lagrange, Parc Valrose, F-06108 Nice Cedex, France
[5] Department of Physics and Astronomy, University of New Mexico, 1919 Lomas Blvd NE, Albuquerque, NM 87131, USA
[6] The CHARA Array of Georgia State University, Mount Wilson, CA 91023, USA
Received 2021 April 28; revised 2021 July 12; accepted 2021 July 12; published 2021 August 25

Abstract

We conducted interferometric observations with the CHARA Array of transiting super-Earth host HD 97658 and measured its limb-darkened angular diameter to be $\theta_{\rm LD} = 0.314 \pm 0.004$ mas. The combination of the angular diameter with the Gaia EDR3 parallax value with zero-point correction ($\pi = 46.412 \pm 0.022$ mas, $d = 21.546 \pm 0.011$ pc) yields a physical radius of $R_\star = 0.728 \pm 0.008\ R_\odot$. We also measured the bolometric flux of the star to be $F_{\rm bol} = 2.42 \pm 0.05 \times 10^{-8}$ erg s^{-1} cm^{-2}, which, together with angular size, allows a measurement of the effective temperature $T_{\rm eff} = 5212 \pm 43$ K. Our directly determined physical stellar properties are in good agreement with previous estimates derived from spectroscopy. We used our measurements in combination with stellar evolutionary models and properties of the transit of HD 97658 b to determine the mass and age of HD 97658 as well as constrain the properties of the planet. Our results and our analysis of the TESS light curve on the planet (TOI-1821) corroborate previous studies of this system with tighter uncertainties.

Unified Astronomy Thesaurus concepts: Fundamental parameters of stars (555); Interferometry (808); Exoplanets (498); Late-type stars (909)

1. Introduction

Interferometric observations of stars provide a unique opportunity to directly measure one of the most fundamental parameters of the star: its radius. Interferometry achieves the resolution of an extremely large telescope by combining the light from one or multiple pairs of telescopes across a variety of separations, or baselines. In particular, optical/near-infrared interferometry requires baselines of only tens of meters to achieve resolutions of milliarcseconds (mas). Direct measurements of stellar radii at great precision will in turn reduce uncertainty in other derived stellar parameters (e.g., effective temperature, surface gravity, or density). Direct observations of stellar radii have highlighted a systematic discrepancy between evolutionary models and reality. Boyajian et al. (2012) have shown that stellar evolutionary models underestimate radii by ∼5% and overestimate temperatures by ∼3% for K and M dwarfs.

Observations with interferometric arrays play an important role in understanding as well as refining exoplanet system properties. In order to understand the properties of the exoplanet, the properties of the star must first be well constrained. In particular, transiting exoplanets provide a measure of the planet's radius, but this measurement is in units of the host star's radius. Any uncertainty or bias in stellar radius will propagate into estimates of the planet's equilibrium temperature, density, habitability, and composition. Interferometry gives a direct measurement of the stellar radius with little or no dependence on stellar models. This technique has been used in the literature to refine the properties of several important systems, such as 55 Cancri, which hosts five radial-velocity exoplanets including another transiting super-Earth (von Braun et al. 2011), and transiting exoplanet host star GJ 436, where evolutionary models underestimated the stellar radius by ∼11% (von Braun et al. 2012). There have also been multiple interferometric surveys of large numbers of exoplanet host stars such as Baines et al. (2008). The field of interferometry has also seen incredible developments in the field of imaging and astrometry with the ESO GRAVITY project (Gravity Collaboration et al. 2017). In 2019, the GRAVITY collaboration announced the first spectrum of an exoplanet observed with interferometry and refined the astrometric position with 100μas precision (Gravity Collaboration et al. 2019).

The exoplanet host star HD 97658 is of particular interest in this regard as it is the home of a transiting super-Earth (Howard et al. 2011; Dragomir et al. 2013). HD 97658 is a bright, $m_V = 7.78$ mag K1 dwarf with a moderately low iron content of [Fe/H] = −0.23 dex, which was discovered to have a Neptunian mass exoplanet by the NASA Eta-Earth Keck-HIRES radial-velocity survey (Howard et al. 2011). Follow-up time series observations with the Spitzer and MOST space telescopes detected a transit whose depth indicated an estimated planetary radius of a few Earth radii (Dragomir et al. 2013; van Grootel et al. 2014). These properties together make HD 97658b a so-called super-Earth (planets with radii of 1–4 $R_\oplus$ and masses of 1–10 $M_\oplus$; Bryan et al. 2019). Super-Earths can take the form of water worlds with a smothering dense atmosphere or rocky behemoths with minimal atmospheres, both often consistent within the uncertainties of planetary mass and radius (Dragomir et al. 2013). Super-Earths captivate planetary scientists as they are the most populous of observed exoplanets (30%–50% of Sun-like stars host one or more super-Earths; Bryan et al. 2019); however, they do not exist within our own solar system and must be studied solely as exoplanets.

We are interested in refining the properties of HD 97658b by directly measuring the host star's properties. In Section 2, we describe the interferometric observations of HD 97658. In Section 3, we report the resulting directly measured angular diameter, bolometric flux. In Section 4, we model and measure the mass of the star. We then derive updated properties of

Appendix D.
Stellar Properties of Literature Stars

Table D.1. Stellar properties used in this study to highlight the need for model improvements.

Star	$\log(L/\,\mathrm{L}_\odot)$	$\sigma_{\log(L)}$	$T_{\rm eff}$ [K]	σ_T	$R_\star$	σ_R	[Fe/H]	$\sigma_{\rm [Fe/H]}$	Ref. [Fe/H]
GJ1	-1.643	0.013	3640	51	0.379	0.002	-0.51	0.08	[55]
GJ33	-0.56	0.013	5020	66	0.693	0.003	-0.27	0.05	[118]
GJ65A	-2.874	0.012	2697	88	0.167	0.006	-0.03	0.2	[67]
GJ65B	-2.947	0.012	2651	93	0.159	0.006	-0.12	0.2	[67]
GJ15A	-1.647	0.009	3603	21	0.384	0.002	-0.3	0.08	[83]
GJ176	-1.451	0.011	3701	85	0.456	0.021	0.14	0.08	[83]
GJ205	-1.189	0.009	3825	21	0.577	0.002	0.49	0.08	[83]
GJ251	-1.788	0.014	3545	71	0.337	0.013	-0.02	0.08	[83]
GJ273	-1.968	0.009	3291	28	0.292	0.004	-0.11	0.08	[83]
GJ338A	-1.116	0.009	3940	37	0.592	0.009	-0.01	0.08	[83]
GJ338B	-1.116	0.009	3974	43	0.582	0.011	-0.01	0.08	[83]
GJ380	-0.954	0.009	4159	26	0.64	0.004	0.24	0.08	[83]
GJ406	-2.977	0.025	2678	47	0.15	0.005	0.25	0.08	[83]
GJ408	-1.712	0.017	3603	79	0.357	0.014	-0.11	0.16	[106]
GJ411	-1.658	0.009	3548	25	0.391	0.004	-0.38	0.08	[83]
GJ412A	-1.633	0.009	3550	43	0.402	0.008	-0.37	0.08	[83]
GJ436	-1.606	0.018	3458	58	0.437	0.014	0.01	0.08	[83]
GJ447	-2.435	0.014	3208	86	0.196	0.011	-0.02	0.08	[83]
GJ526	-1.43	0.009	3626	35	0.487	0.007	-0.31	0.08	[83]
GJ551	-2.821	0.012	2896	38	0.154	0.001	0.04	0.25	[73]
GJ581	-1.922	0.011	3359	31	0.322	0.005	-0.15	0.08	[83]
GJ625	-1.845	0.014	3350	55	0.354	0.011	-0.35	0.08	[83]
GJ628	-1.957	0.011	3379	40	0.306	0.006	-0.03	0.08	[83]
GJ649	-1.357	0.01	3592	47	0.54	0.013	0.03	0.08	[83]
GJ674	-1.795	0.013	3421	169	0.36	0.018	-0.257	0.08	[55]
GJ686	-1.529	0.011	3602	123	0.44	0.029	-0.25	0.08	[83]
GJ687	-1.661	0.01	3420	32	0.419	0.006	0.05	0.08	[83]
GJ699	-2.466	0.01	3225	23	0.187	0.001	-0.4	0.08	[83]
GJ701	-1.491	0.011	3953	78	0.382	0.014	-0.22	0.08	[83]
GJ702B	-0.824	0.012	4388	76	0.669	0.008	-0.24	0.05	[23]
GJ725A	-1.819	0.009	3398	24	0.354	0.003	-0.23	0.08	[83]
GJ725B	-2.059	0.011	3106	38	0.322	0.006	-0.23	0.08	[83]
GJ729	-2.395	0.011	3207	54	0.205	0.006	-0.18	0.08	[83]
GJ752A	-1.48	0.009	3542	18	0.531	0.03	0.1	0.08	[83]
GJ809	-1.284	0.011	3727	30	0.545	0.006	-0.06	0.08	[83]
GJ832	-1.54	0.012	3609	61	0.434	0.006	-0.17	0.09	[73]
GJ846	-1.202	0.012	3544	63	0.663	0.022	0.02	0.08	[83]
GJ873	-1.896	0.012	3269	31	0.351	0.004	-0.9	0.16	[106]
GJ876	-1.882	0.011	3280	27	0.353	0.005	0.17	0.08	[83]
GJ880	-1.281	0.009	3724	22	0.548	0.003	0.21	0.08	[83]
GJ887	-1.433	0.009	3690	24	0.469	0.002	-0.06	0.08	[83]
GJ896A	-1.708	0.015	3324	69	0.421	0.017	0.03	0.08	[83]
GJ905	-2.624	0.018	2872	37	0.196	0.004	0.23	0.08	[83]
GJ908	-1.587	0.011	3479	48	0.441	0.011	-0.45	0.08	[83]

Appendix E.
Surface Brightness Relation Data

Table E.1. The complete set of photometry and angular diameters used for the development of surface brightness relations in § 7. Italicized magnitudes denote values obtained via color transformation relationships.

Star	V	σ_V	G	σ_G	R_C	σ_{R_C}	I_C	σ_{I_C}	J	σ_J	H	σ_H	K_S	σ_{K_S}	$\theta_{\rm LD}$	σ_θ	θ Ref	Phot. Refs
GJ15A	8.12	0.03	7.15	0.02	7.12	0.02	5.99	0.03	4.90	0.03	4.30	0.03	4.04	0.03	1.005	0.005	[18]	[83]
GJ169	8.34	0.03	7.63	0.02	7.46	0.02	6.63	0.03	5.7	0.03	5.04	0.03	4.85	0.03	0.56	0.024	This work	[83]
GJ176	9.99	0.03	8.9	0.02	8.95	0.02	7.7	0.03	6.49	0.03	5.89	0.03	5.6	0.03	0.448	0.021	[126]	[83]
GJ205	7.93	0.03	7.04	0.02	7.01	0.02	5.93	0.03	4.8	0.03	4.12	0.03	3.86	0.03	0.943	0.003	[18]	[83]
GJ251	10.07	0.03	8.76	0.02	8.92	0.02	7.46	0.03	6.11	0.03	5.52	0.03	5.27	0.03	0.563	0.022	This work	[83]
GJ273	9.89	0.03	8.48	0.02	8.68	0.02	7.10	0.03	5.68	0.03	5.12	0.03	4.89	0.03	0.783	0.01	This work	[83]
GJ338A	7.65	0.03	6.92	0.02	6.76	0.02	5.90	0.03	4.93	0.03	4.25	0.03	4.03	0.03	0.871	0.014	[18]	[83]
GJ338B	7.65	0.03	6.99	0.02	6.76	0.02	5.90	0.03	4.93	0.03	4.25	0.03	4.03	0.03	0.856	0.016	[18]	[83]
GJ380	6.54	0.03	5.92	0.02	5.68	0.02	4.88	0.03	3.98	0.03	3.33	0.03	3.19	0.03	1.225	0.008	[18]	[83]
GJ406	13.52	0.03	10.88	0.02	11.61	0.02	9.37	0.03	7.07	0.03	6.46	0.03	6.15	0.03	0.582	0.02	[100]	[83]
GJ411	7.5	0.03	6.50	0.02	6.48	0.02	5.28	0.03	4.17	0.03	3.60	0.03	3.36	0.03	1.432	0.013	[18]	[83]
GJ412A	8.78	0.03	7.83	0.02	7.73	0.02	6.62	0.03	5.55	0.03	4.97	0.03	4.74	0.03	0.764	0.016	[18]	[83]
GJ436	10.69	0.03	9.46	0.02	9.56	0.02	8.16	0.03	6.91	0.03	6.30	0.03	6.04	0.03	0.417	0.013	[125]	[83]
GJ447	11.15	0.03	9.48	0.02	9.83	0.02	8.13	0.03	6.57	0.03	6.00	0.03	5.68	0.03	0.54	0.029	[100]	[83]
GJ526	8.48	0.03	7.54	0.02	7.46	0.02	6.32	0.03	5.24	0.03	4.71	0.03	4.56	0.03	0.835	0.013	[18]	[83]
GJ581	10.58	0.03	9.30	0.02	9.45	0.02	8.02	0.03	6.72	0.03	6.13	0.03	5.9	0.03	0.476	0.007	[100]	[83]
GJ625	10.12	0.03	9.03	0.02	9.06	0.02	7.82	0.03	6.63	0.03	6.07	0.03	5.84	0.03	0.509	0.015	This work	[83]
GJ628	10.1	0.03	8.7	0.02	8.89	0.02	7.33	0.03	5.95	0.03	5.39	0.03	5.08	0.03	0.661	0.014	[100]	[83]
GJ649	9.67	0.03	8.72	0.02	8.7	0.02	7.6	0.03	6.5	0.03	5.88	0.03	5.63	0.03	0.484	0.012	[126]	[83]
GJ686	9.60	0.03	8.64	0.02	8.6	0.02	7.5	0.03	6.38	0.03	5.82	0.03	5.56	0.03	0.503	0.033	This work	[83]
GJ687	9.18	0.03	7.94	0.02	8.1	0.02	6.68	0.03	5.35	0.03	4.78	0.03	4.50	0.03	0.859	0.013	[18]	[83]
GJ699	9.53	0.03	8.11	0.02	8.32	0.02	6.73	0.03	5.3	0.03	4.8	0.03	4.53	0.03	0.952	0.005	[18]	[83]
GJ701	9.39	0.03	8.42	0.02	8.4	0.02	7.31	0.03	6.18	0.03	5.59	0.03	5.32	0.03	0.46	0.017	This work	[83]
GJ725A	8.9	0.03	7.77	0.02	7.84	0.02	6.47	0.03	5.2	0.03	4.64	0.03	4.41	0.03	0.937	0.008	[18]	[83]
GJ725B	9.73	0.03	8.43	0.02	8.60	0.02	7.13	0.03	5.2	0.03	5.21	0.03	4.96	0.03	0.851	0.015	[18]	[83]
GJ729	10.53	0.03	9.02	0.02	9.23	0.02	7.62	0.03	6.23	0.03	5.66	0.03	5.39	0.03	0.642	0.02	[100]	[83]
GJ752A	9.14	0.03	8.01	0.02	8.08	0.02	6.74	0.03	5.54	0.03	4.92	0.03	4.7	0.03	0.836	0.049	This work	[83]
GJ809	8.57	0.03	7.68	0.02	7.64	0.02	6.63	0.03	5.49	0.03	4.83	0.03	4.58	0.03	0.722	0.008	[18]	[83]
GJ846	9.18	0.03	8.31	0.02	8.23	0.02	7.24	0.03	6.21	0.03	5.53	0.03	5.35	0.03	0.584	0.019	This work	[83]
GJ876	10.18	0.02	8.77	0.02	8.98	0.02	7.41	0.03	5.95	0.03	5.31	0.03	5.04	0.03	0.705	0.009	[100]	[83]

Table continued

Star	V	σ_V	G	σ_G	R_C	σ_{R_C}	I_C	σ_{I_C}	J	σ_J	H	σ_H	K_S	σ_{K_S}	$\theta_{\rm LD}$	σ_θ	θ Ref	Phot Refs
GJ880	8.67	0.02	7.72	0.02	7.67	0.02	6.55	0.03	5.39	0.03	4.72	0.03	4.54	0.03	0.744	0.004	[18]	[83]
GJ887	7.34	0.02	6.47	0.02	6.37	0.02	5.29	0.03	4.21	0.03	3.58	0.03	3.33	0.03	1.328	0.005	[100]	[83]
GJ896A	10.2	0.02	8.94	0.02	9	0.02	7.45	0.03	6.17	0.03	5.59	0.03	5.33	0.03	0.626	0.025	This work	[83]
GJ905	12.37	0.02	10.24	0.02	10.73	0.02	8.76	0.03	6.84	0.03	6.22	0.03	5.87	0.03	0.579	0.013	This work	[83]
GJ908	9.00	0.02	8.06	0.02	8.02	0.02	6.89	0.03	5.82	0.03	5.32	0.03	5.09	0.03	0.696	0.018	This work	[83]
GJ1	8.56	0.01	7.68	0.05	7.59	0.01	6.43	0.01	5.28	0.02	4.53	0.02	4.52	0.02	0.812	0.005	[100]	[70]
GJ105	5.82	0.02	5.50	0.05	*5.23*	0.02	*4.72*	0.02	*4.01*	0.02	*3.51*	0.02	*3.43*	0.02	1.03	0.007	[18]	[64] [48]
GJ166A	4.43	0.02	4.18	0.05	*3.93*	0.02	*3.50*	0.02	*2.89*	0.02	*2.47*	0.02	*2.38*	0.02	1.504	0.006	[18]	[64] [63]
GJ33	5.76	0.02	5.47	0.05	*5.20*	0.02	*4.76*	0.02	*4.18*	0.02	*3.70*	0.02	*3.59*	0.02	0.868	0.004	[18]	[64] [63]
GJ408	10.02	0.02	8.98	0.05	8.95	0.02	7.65	0.02	6.34	0.02	5.77	0.02	5.5	0.02	0.493	0.019	This work	[70]
GJ49	9.56	0.01	8.67	0.05	···	···	*7.70*	0.05	6.23	0.02	5.58	0.02	5.37	0.02	0.519	0.019	This work	[4] [32]
GJ551	11.05	0.03	8.98	0.05	*9.45*	0.03	*7.41*	0.03	*5.36*	0.02	4.84	0.06	4.38	0.03	1.103	0.007	[100]	[32] [80]
GJ631	5.74	0.02	5.55	0.05	*5.29*	0.02	*4.92*	0.02	*4.26*	0.02	*3.85*	0.02	*3.80*	0.02	0.724	0.011	[18]	[64] [63]
GJ65A	12.57	0.05	10.51	0.05	···	···	···	···	7.1	0.05	6.52	0.05	6.2	0.05	0.573	0.02	[67]	[4] [67]
GJ65B	12.52	0.05	10.82	0.05	···	···	···	···	7.26	0.05	6.68	0.05	6.36	0.05	0.554	0.021	[67]	[4] [67]
GJ674	9.41	0.01	8.34	0.05	8.34	0.01	7.01	0.01	5.69	0.02	5.14	0.01	4.87	0.01	0.737	0.037	[100]	[70]
GJ702B	6.06	0.05	5.54	0.05	···	···	···	···	···	···	···	···	3.57	0.05	1.221	0.015	[18]	[27]
GJ832	8.67	0.01	7.74	0.05	7.67	0.01	6.48	0.01	5.29	0.02	4.72	0.02	4.47	0.02	0.814	0.01	[100]	[70]
GJ873	10.29	0.01	9.01	0.05	9.08	0.05	7.57	0.05	6.11	0.03	5.55	0.03	5.3	0.02	0.647	0.007	This work	[4]
GJ892	5.57	0.02	5.23	0.05	*4.98*	0.02	*4.47*	0.02	*3.80*	0.02	*3.37*	0.02	*3.21*	0.02	1.035	0.021	[18]	[64] [63]
HD103095	6.44	0.02	6.20	0.05	*5.97*	0.02	*6.18*	0.02	*4.83*	0.02	*4.42*	0.02	*4.34*	0.02	0.597	0.004	[66]	[87]
HD189733	7.65	0.03	7.43	0.05	7.13	0.03	6.68	0.03	6.07	0.03	5.59	0.03	5.54	0.03	0.385	0.005	[16]	[70] [32]

Works Cited

[1] Africano, J. L., Cobb, C. L., Dunham, D. W., Evans, D. S., Fekel, F. C., & Vogt, S. S. (1975). Photoelectric measurements of lunar occultations VII: further observational results. *AJ*, *80*, 689–697.

[2] Akaike, H. (1974). A New Look at the Statistical Model Identification. *IEEE Transactions on Automatic Control*, *19*, 716–723.

[3] Alonso-Floriano, F. J., et al. (2015). CARMENES input catalogue of M dwarfs. I. Low-resolution spectroscopy with CAFOS. *AAP*, *577*, A128.

[4] Anderson, E., & Francis, C. (2012). XHIP: An extended hipparcos compilation. *Astronomy Letters*, *38*(5), 331–346.

[5] Angus, R., Morton, T. D., Foreman-Mackey, D., van Saders, J., Curtis, J., Kane, S. R., Bedell, M., Kiman, R., Hogg, D. W., & Brewer, J. (2019). Toward Precise Stellar Ages: Combining Isochrone Fitting with Empirical Gyrochronology. *AJ*, *158*(5), 173.

[6] Anugu, N., et al. (2020). MIRC-X: A Highly Sensitive Six-telescope Interferometric Imager at the CHARA Array. *AJ*, *160*(4), 158.

[7] Baines, E. K., Armstrong, J. T., Schmitt, H. R., Zavala, R. T., Benson, J. A., Hutter, D. J., Tycner, C., & van Belle, G. T. (2018). Fundamental Parameters of 87 Stars from the Navy Precision Optical Interferometer. *AJ*, *155*(1), 30.

[8] Baines, E. K., McAlister, H. A., ten Brummelaar, T. A., Turner, N. H., Sturmann, J., Sturmann, L., Goldfinger, P. J., & Ridgway, S. T. (2008). CHARA Array Measurements of the Angular Diameters of Exoplanet Host Stars. *ApJ*, *680*(1), 728–733.

[9] Barnes, J. R., Jeffers, S. V., Haswell, C. A., Jones, H. R. A., Shulyak, D., Pavlenko, Y. V., & Jenkins, J. S. (2017). Surprisingly different star-spot distributions on the near equal-mass equal-rotation-rate stars in the M dwarf binary GJ 65 AB. *MNRAS*, *471*(1), 811–823.

[10] Barnes, T. G., & Evans, D. S. (1976). Stellar angular diameters and visual surface brightness - I. Late spectral types. *MNRAS*, *174*, 489–502.

[11] Berger, D. H., et al. (2006). First Results from the CHARA Array. IV. The Interferometric Radii of Low-Mass Stars. *ApJ*, *644*(1), 475–483.

[12] Berger, T. A., Huber, D., van Saders, J. L., Gaidos, E., Tayar, J., & Kraus, A. L. (2020). The Gaia-Kepler Stellar Properties Catalog. I. Homogeneous Fundamental Properties for 186,301 Kepler Stars. *AJ*, *159*(6), 280.

[13] Bessell, M. S. (2000). The Hipparcos and Tycho Photometric System Passbands. *PASP*, *112*, 961–965.

[14] Boden, A. F., et al. (1998). An Interferometric Search for Bright Companions to 51 Pegasi. *ApJ*, *504*(1), L39–L42.

[15] Bohlin, R. C., Gordon, K. D., & Tremblay, P. E. (2014). Techniques and Review of Absolute Flux Calibration from the Ultraviolet to the Mid-Infrared. *Publications of the Astronomical Society of the Pacific*, *126*(942), 711.

[16] Boyajian, T., et al. (2015). Stellar diameters and temperatures - VI. High angular resolution measurements of the transiting exoplanet host stars HD 189733 and HD 209458 and implications for models of cool dwarfs. *MNRAS*, *447*(1), 846–857.

[17] Boyajian, T. S., van Belle, G., & von Braun, K. (2014). Stellar Diameters and Temperatures. IV. Predicting Stellar Angular Diameters. *AJ*, *147*(3), 47.

[18] Boyajian, T. S., et al. (2012). Stellar Diameters and Temperatures. II. Main-sequence K- and M-stars. *ApJ*, *757*, 112.

[19] Bressan, A., Marigo, P., Girardi, L., Salasnich, B., Dal Cero, C., Rubele, S., & Nanni, A. (2012). PARSEC: stellar tracks and isochrones with the PAdova and TRieste Stellar Evolution Code. *MNRAS*, *427*(1), 127–145.

[20] Brown, R. H., & Twiss, R. Q. (1956). Correlation between Photons in two Coherent Beams of Light. *Nature*, *177*(4497), 27–29.

[21] Bryan, M. L., Knutson, H. A., Lee, E. J., Fulton, B. J., Batygin, K., Ngo, H., & Meshkat, T. (2019). An Excess of Jupiter Analogs in Super-Earth Systems. *AJ*, *157*(2), 52.

[22] Carpenter, J. M. (2001). Color Transformations for the 2MASS Second Incremental Data Release. *AJ*, *121*(5), 2851–2871.

[23] Casagrande, L., Schönrich, R., Asplund, M., Cassisi, S., Ramírez, I., Meléndez, J., Bensby, T., & Feltzing, S. (2011). New constraints on the chemical evolution of the solar neighbourhood and Galactic disc(s). Improved astrophysical parameters for the Geneva-Copenhagen Survey. *A&A*, *530*, A138.

[24] Chabrier, G., Gallardo, J., & Baraffe, I. (2007). Evolution of low-mass star and brown dwarf eclipsing binaries. *A&A*, *472*(2), L17–L20.

[25] Chelli, A., Duvert, G., Bourgès, L., Mella, G., Lafrasse, S., Bonneau, D., & Chesneau, O. (2016). Pseudomagnitudes and differential surface brightness: Application to the apparent diameter of stars. *AAP*, *589*, A112.

[26] Choi, J., Dotter, A., Conroy, C., Cantiello, M., Paxton, B., & Johnson, B. D. (2016). Mesa Isochrones and Stellar Tracks (MIST). I. Solar-scaled Models. *ApJ*, *823*(2), 102.

[27] Christou, J. C., & Drummond, J. D. (2006). Measurements of Binary Stars, Including Two New Discoveries, with the Lick Observatory Adaptive Optics System. *AJ*, *131*(6), 3100–3108.

[28] Claret, A., & Bloemen, S. (2011). Gravity and limb-darkening coefficients for the Kepler, CoRoT, Spitzer, uvby, UBVRIJHK, and Sloan photometric systems. *AAP*, *529*, A75.

[29] Colavita, M. M., et al. (2009). Keck Interferometer Nuller Data Reduction and On-Sky Performance. *PASP*, *121*(884), 1120.

[30] Creech-Eakman, M. J., et al. (2018). The Magdalena Ridge Observatory interferometer: first light and deployment of the first telescope on the array. In *Proc. SPIE*, vol. 10701 of *Society of Photo-Optical Instrumentation Engineers (SPIE) Conference Series*, (p. 1070106).

[31] Crida, A., Ligi, R., Dorn, C., & Lebreton, Y. (2018). Mass, Radius, and Composition of the Transiting Planet 55 Cnc e: Using Interferometry and Correlations. *ApJ*, *860*, 122.

[32] Cutri, R. M., et al. (2003). VizieR Online Data Catalog: 2MASS All-Sky Catalog of Point Sources (Cutri+ 2003). *VizieR Online Data Catalog*, (p. II/246).

[33] de Vegt, C. (1976). Angular diameters of stars from lunar occultations. *A&A*, *47*, 457–459.

[34] Demory, B. O., et al. (2009). Mass-radius relation of low and very low-mass stars revisited with the VLTI. *A&A*, *505*(1), 205–215.

[35] Dotter, A. (2016). MESA Isochrones and Stellar Tracks (MIST) 0: Methods for the Construction of Stellar Isochrones. *ApJS*, *222*(1), 8.

[36] Dragomir, D., et al. (2013). Most detects transits of hd 97658b, a warm, likely volatile-rich super-earth. *ApJ Letters*, *772*(1), L2.
URL `http://stacks.iop.org/2041-8205/772/i=1/a=L2`

[37] Droege, T. F., Richmond, M. W., Sallman, M. P., & Creager, R. P. (2006). TASS Mark IV Photometric Survey of the Northern Sky. *PASP*, *118*, 1666–1678.

[38] Duvert, G. (2016). VizieR Online Data Catalog: JMDC : JMMC Measured Stellar Diameters Catalogue (Duvert, 2016). *VizieR Online Data Catalog*, *2345*.

[39] Duvert, G. (2016). VizieR Online Data Catalog: JMDC : JMMC Measured Stellar Diameters Catalogue (Duvert, 2016). *VizieR Online Data Catalog*, (p. II/345).

[40] Eastman, J. (2017). EXOFASTv2: Generalized publication-quality exoplanet modeling code.

[41] Eastman, J., Gaudi, B. S., & Agol, E. (2013). EXOFAST: A Fast Exoplanetary Fitting Suite in IDL. *PASP*, *125*(923), 83.

[42] Feiden, G. A., & Chaboyer, B. (2013). Magnetic Inhibition of Convection and the Fundamental Properties of Low-mass Stars. I. Stars with a Radiative Core. *ApJ*, *779*(2), 183.

[43] Gaia Collaboration, Brown, A. G. A., Vallenari, A., Prusti, T., de Bruijne, J. H. J., Mignard, F., Drimmel, R., Babusiaux, C., Bailer-Jones, C. A. L., Bastian, U., & et al. (2016). Gaia Data Release 1. Summary of the astrometric, photometric, and survey properties. *AAP*, *595*, A2.

[44] Gaia Collaboration, Prusti, T., de Bruijne, J. H. J., Brown, A. G. A., Vallenari, A., Babusiaux, C., Bailer-Jones, C. A. L., Bastian, U., Biermann, M., Evans, D. W., & et al. (2016). The Gaia mission. *AAP*, *595*, A1.

[45] Gaia Collaboration, et al. (2018). Gaia Data Release 2. Summary of the contents and survey properties. *AAP*, *616*, A1.

[46] Gaia Collaboration, et al. (2021). Gaia Early Data Release 3. Summary of the contents and survey properties. *A&A*, *649*, A1.

[47] Gallenne, A. and others (2019). Multiplicity of Galactic Cepheids from long-baseline interferometry. IV. New detected companions from MIRC and PIONIER observations. *AAP*, *622*, A164.

[48] Glass, I. S. (1975). Intermediate infrared colours of M-dwarf stars. *MNRAS*, *171*, 19P–23.

[49] Gravity Collaboration, et al. (2017). First light for GRAVITY: Phase referencing optical interferometry for the Very Large Telescope Interferometer. *A&A*, *602*, A94.

[50] Gravity Collaboration, et al. (2019). First direct detection of an exoplanet by optical interferometry. Astrometry and K-band spectroscopy of HR 8799 e. *A&A*, *623*, L11.

[51] Guo, X., et al. (2020). Updated Parameters and a New Transmission Spectrum of HD 97658b. *AJ*, *159*(5), 239.

[52] Hanbury Brown, R. (1956). A Test of a New Type of Stellar Interferometer on Sirius. *Nature*, *178*, 1046–1048.

[53] Hanbury Brown, R., Davis, J., & Allen, L. R. (1974). The Angular Diameters of 32 Stars. *MNRAS*, *167*, 121–136.

[54] Hanbury Brown, R., Davis, J., Lake, R. J., & Thompson, R. J. (1974). The effects of limb darkening on measurements of angular size with an intensity interferometer. *MNRAS*, *167*, 475–484.

[55] Hojjatpanah, S., et al. (2019). Catalog for the ESPRESSO blind radial velocity exoplanet survey. *A&A*, *629*, A80.

[56] Howard, A. W., Johnson, J. A., Marcy, G. W., Fischer, D. A., Wright, J. T., Henry, G. W., Isaacson, H., Valenti, J. A., Anderson, J., & Piskunov, N. E. (2011). The NASA-UC Eta-Earth Program. III. A Super-Earth Orbiting HD 97658 and a Neptune-mass Planet Orbiting Gl 785. *ApJ*, *730*, 10.

[57] Huber, D., et al. (2017). Asteroseismology and Gaia: Testing Scaling Relations Using 2200 Kepler Stars with TGAS Parallaxes. *ApJ*, *844*(2), 102.

[58] Husser, T.-O., Wende-von Berg, S., Dreizler, S., Homeier, D., Reiners, A., Barman, T., & Hauschildt, P. H. (2013). Astrophysics A new extensive library of PHOENIX stellar atmospheres. *Å*, *553*, A6.

[59] Illarramendi, M. A., Arregui, L., Zubia, J., Hueso, R., & Sanchez-Lavega, A. (2017). Teaching stellar interferometry with polymer optical fibers. In X. Liu, & X.-C. Zhang (Eds.) *14th Conference on Education and Training in Optics and Photonics: ETOP 2017*, vol. 10452, (pp. 227 – 235). International Society for Optics and Photonics, SPIE.
URL `https://doi.org/10.1117/12.2266542`

[60] Illarramendi, M. A., Arregui, L., Zubia, J., Hueso, R., & Sanchez-Lavega, A. (2017). Teaching stellar interferometry with polymer optical fibers. In *Society of Photo-Optical Instrumentation Engineers (SPIE) Conference Series*, vol. 10452 of *Society of Photo-Optical Instrumentation Engineers (SPIE) Conference Series*, (p. 1045216).

[61] Ireland, M. J., Mérand, A., ten Brummelaar, T. A., Tuthill, P. G., Schaefer, G. H., Turner, N. H., Sturmann, J., Sturmann, L., & McAlister, H. A. (2008). Sensitive visible interferometry with PAVO. In *Optical and Infrared Interferometry*, vol. 7013, (p. 701324).

[62] Isaacson, H., & Fischer, D. (2010). Chromospheric Activity and Jitter Measurements for 2630 Stars on the California Planet Search. *ApJ*, *725*(1), 875–885.

[63] Johnson, H. L., Mcarthur, J. W., & Mitchell, R. I. (1968). The spectral energy curves of subdwarfs. I. *ApJ*, *152*, 465.

[64] Johnson, H. L., Mitchell, R. I., Iriarte, B., & Wisniewski, W. Z. (1966). UBVRI-JKL Photometry of the Bright Stars. *Communications of the Lunar and Planetary Laboratory*, *4*, 99–110.

[65] Jones, E., Oliphant, T., Peterson, P., et al. (2001). SciPy: Open source scientific tools for Python. [Online].
URL `http://www.scipy.org/`

[66] Karovicova, I., White, T. R., Nordlander, T., Casagrande, L., Ireland, M., Huber, D., & Jofré, P. (2020). Fundamental stellar parameters of benchmark stars from CHARA interferometry. I. Metal-poor stars. *A&A*, *640*, A25.

[67] Kervella, P., Mérand, A., Ledoux, C., Demory, B. O., & Le Bouquin, J. B. (2016). The red dwarf pair GJ65 AB: inflated, spinning twins of Proxima. Fundamental parameters from PIONIER, NACO, and UVES observations. *A&A*, *593*, A127.

[68] Kervella, P., Thévenin, F., Di Folco, E., & Ségransan, D. (2004). The angular sizes of dwarf stars and subgiants. Surface brightness relations calibrated by interferometry. *A&A*, *426*, 297–307.

[69] Kharchenko, N. V. (2001). All-sky compiled catalogue of 2.5 million stars. *Kinematika i Fizika Nebesnykh Tel*, *17*, 409–423.

[70] Koen, C., Kilkenny, D., van Wyk, F., & Marang, F. (2010). UBV(RI)$_C$ JHK observations of Hipparcos-selected nearby stars. *MNRAS*, *403*(4), 1949–1968.

[71] Kotoneva, E., Flynn, C., Chiappini, C., & Matteucci, F. (2002). K dwarfs and the chemical evolution of the solar cylinder. *MNRAS*, *336*, 879–891.

[72] Kovács, G., Zucker, S., & Mazeh, T. (2002). A box-fitting algorithm in the search for periodic transits. *A&A*, *391*, 369–377.

[73] Kuznetsov, M. K., del Burgo, C., Pavlenko, Y. V., & Frith, J. (2019). Characterization of a Sample of Southern M Dwarfs Using Harps and X-shooter Spectra. *ApJ*, *878*(2), 134.

[74] Lachaume, R., Rabus, M., Jordán, A., Brahm, R., Boyajian, T., von Braun, K., & Berger, J.-P. (2019). Towards reliable uncertainties in IR interferometry: the bootstrap for correlated statistical and systematic errors. *MNRAS*, *484*(2), 2656–2673.

[75] Lawson, P. R. (Ed.) (2000). *Principles of Long Baseline Stellar Interferometry*. JPL.

[76] Ligi, R., et al. (2019). From the stellar properties of HD 219134 to the internal compositions of its transiting exoplanets. *A&A*, *631*, A92.

[77] Ligi, R., Creevey, O., Mourard, D., Crida, A., Lagrange, A.-M., Nardetto, N., Perraut, K., Schultheis, M., Tallon-Bosc, I., & ten Brummelaar, T. (2016). Radii, masses, and ages of 18 bright stars using interferometry and new estimations of exoplanetary parameters. *A&A*, *586*, A94.
URL `https://doi.org/10.1051/0004-6361/201527054`

[78] Lindegren, L., et al. (2021). Gaia Early Data Release 3. Parallax bias versus magnitude, colour, and position. *A&A*, *649*, A4.

[79] Lindegren, L., et al. (2021). Gaia Early Data Release 3. Parallax bias versus magnitude, colour, and position. *AAP*, *649*, A4.

[80] Lurie, J. C., Henry, T. J., Jao, W.-C., Quinn, S. N., Winters, J. G., Ianna, P. A., Koerner, D. W., Riedel, A. R., & Subasavage, J. P. (2014). The Solar Neighborhood. XXXIV. a Search for Planets Orbiting Nearby M Dwarfs Using Astrometry. *AJ*, *148*(5), 91.

[81] Mallama, A. (2014). Sloan Magnitudes for the Brightest Stars. *JAAVSO*, *42*(2), 443.

[82] Mamajek, E. E., & Hillenbrand, L. A. (2008). Improved Age Estimation for Solar-Type Dwarfs Using Activity-Rotation Diagnostics. *ApJ*, *687*(2), 1264–1293.

[83] Mann, A. W., Feiden, G. A., Gaidos, E., Boyajian, T., & von Braun, K. (2015). How to Constrain Your M Dwarf: Measuring Effective Temperature, Bolometric Luminosity, Mass, and Radius. *ApJ*, *804*(1), 64.

[84] Mann, A. W., & von Braun, K. (2015). Revised Filter Profiles and Zero Points for Broadband Photometry. *Publications of the Astronomical Society of the Pacific*, *127*(948), 102.

[85] Maxted, P. F. L., Serenelli, A. M., & Southworth, J. (2015). Bayesian mass and age estimates for transiting exoplanet host stars. *A&A*, *575*, A36.

[86] Mayor, M., & Queloz, D. (1995). A Jupiter-mass companion to a solar-type star. *Nature*, *378*(6555), 355–359.

[87] Mendoza v., E. E. (1963). Estudio Espectroscópico y Fotométrico del Cúmulo Estelar en Coma BerenicesEstudio Espectroscópico y Fotométrico del Cúmulo Estelar en Coma BerenicesA Spectroscopic and Photometric Study of the Star Cluster in Coma Berenices;. *Boletin de los Observatorios Tonantzintla y Tacubaya*, *3*, 137–149.

[88] Mermilliod, J.-C. (1994). VizieR Online Data Catalog: UBV Photoelectric Cat: Data 1986-1992 (Mermilliod 1994). *VizieR Online Data Catalog*, *2193*.

[89] Michelson, A. A., & Pease, F. G. (1921). Measurement of the Diameter of α Orionis with the Interferometer. *ApJ*, *53*.

[90] Monnier, J. D., Berger, J.-P., Millan-Gabet, R., & ten Brummelaar, T. A. (2004). The Michigan Infrared Combiner (MIRC): IR imaging with the CHARA Array. In W. A. Traub (Ed.) *New Frontiers in Stellar Interferometry*, vol. 5491 of *Society of Photo-Optical Instrumentation Engineers (SPIE) Conference Series*, (p. 1370).

[91] Mourard, D., et al. (2009). VEGA: Visible spEctroGraph and polArimeter for the CHARA array: principle and performance. *A&A*, *508*(2), 1073–1083.

[92] Mourard, D., et al. (2009). VEGA: Visible spEctroGraph and polArimeter for the CHARA array: principle and performance. *A&A*, *508*, 1073–1083.

[93] Mourard, D., et al. (2011). Spatio-spectral encoding of fringes in optical long-baseline interferometry. Example of the 3T and 4T recombining mode of VEGA/CHARA. *A&A*, *531*, A110.

[94] Mourard, D., et al. (2018). SPICA, a new 6T visible beam combiner for CHARA: science, design and interfaces. In M. J. Creech-Eakman, P. G. Tuthill, & A. Mérand (Eds.) *Optical and Infrared Interferometry and Imaging VI*, vol. 10701 of *Society of Photo-Optical Instrumentation Engineers (SPIE) Conference Series*, (p. 1070120).

[95] Nardetto, N., et al. (2020). Calibrating the surface brightness - color relation for late-type red giants stars in the visible domain using VEGA/CHARA interferometric observations. *A&A*, *639*, A67.

[96] Nordgren, T. E., et al. (1999). Stellar Angular Diameters of Late-Type Giants and Supergiants Measured with the Navy Prototype Optical Interferometer. *AJ*, *118*(6), 3032–3038.

[97] Parviainen, H., & Aigrain, S. (2015). LDTK: Limb Darkening Toolkit. *MNRAS*, *453*(4), 3821–3826.

[98] Perger, M., et al. (2019). Gliese 49: activity evolution and detection of a super-Earth. A HADES and CARMENES collaboration. *AAP*, *624*, A123.

[99] Pickles, A. J. (1998). A Stellar Spectral Flux Library: 1150-25000 Å. *PASP*, *110*, 863–878.

[100] Rabus, M., et al. (2019). A discontinuity in the T_{eff}-radius relation of M-dwarfs. *MNRAS*, *484*(2), 2674–2683.

[101] Ricker, G. R., et al. (2015). Transiting Exoplanet Survey Satellite (TESS). *Journal of Astronomical Telescopes, Instruments, and Systems*, *1*, 014003.

[102] Riello, M., et al. (2021). Gaia Early Data Release 3. Photometric content and validation. *A&A*, *649*, A3.

[103] Roettenbacher, R. M., et al. (2015). Detecting the Companions and Ellipsoidal Variations of RS CVn Primaries. II. o Draconis, a Candidate for Recent Low-mass Companion Ingestion. *ApJ*, *809*(2), 159.

[104] Salsi, A., et al. (2020). Precise calibration of the dependence of surface brightness-colour relations on colour and class for late-type stars. *A&A*, *640*, A2.

[105] Schwarz, G. (1978). Estimating the Dimension of a Model. *The Annals of Statistics*, *6*(2), 461 – 464.
URL `https://doi.org/10.1214/aos/1176344136`

[106] Schweitzer, A., et al. (2019). The CARMENES search for exoplanets around M dwarfs. Different roads to radii and masses of the target stars. *A&A*, *625*, A68.

[107] Seager, S., & Mallén-Ornelas, G. (2003). A Unique Solution of Planet and Star Parameters from an Extrasolar Planet Transit Light Curve. *ApJ*, *585*, 1038–1055.

[108] Ségransan, D., Kervella, P., Forveille, T., & Queloz, D. (2003). First radius measurements of very low mass stars with the VLTI. *A&A*, *397*, L5–L8.

[109] Shao, M., Colavita, M. M., Hines, B. E., Staelin, D. H., Hutter, D. J., Johnston, K. J., Mozurkewich, D., Simon, R. S., Hershey, J. L., Hughes, J. A., & Kaplan, G. H. (1988). The Mark III stellar interferometer. *A&A*, *193*(1-2), 357–371.

[110] Shao, M., et al. (1988). The Mark III stellar interferometer. *AAP*, *193*, 357–371.

[111] Skrutskie, M. F., et al. (2006). The two micron all sky survey (2mass). *The Astronomical Journal*, *131*(2), 1163–1183.
URL `https://doi.org/10.1086%2F498708`

[112] Southworth, J. (2015). DEBCat: A Catalog of Detached Eclipsing Binary Stars. In S. M. Rucinski, G. Torres, & M. Zejda (Eds.) *Living Together: Planets, Host Stars and Binaries*, vol. 496 of *Astronomical Society of the Pacific Conference Series*, (p. 164).

[113] Spada, F., Demarque, P., Kim, Y. C., Boyajian, T. S., & Brewer, J. M. (2017). The Yale-Potsdam Stellar Isochrones. *ApJ*, *838*(2), 161.

[114] Swain, M., et al. (2003). Interferometer Observations of Subparsec-Scale Infrared Emission in the Nucleus of NGC 4151. *ApJ*, *596*(2), L163–L166.

[115] Tallon-Bosc, I., et al. (2008). LITpro: a model fitting software for optical interferometry. In *Society of Photo-Optical Instrumentation Engineers (SPIE) Conference Series*, vol. 7013 of *Society of Photo-Optical Instrumentation Engineers (SPIE) Conference Series*.

[116] Ten Brummelaar, T. A., Sturmann, J., Ridgway, S. T., Sturmann, L., Turner, N. H., McAlister, H. A., Farrington, C. D., Beckmann, U., Weigelt, G., & Shure, M. (2013). The Classic/climb Beam Combiner at the CHARA Array. *Journal of Astronomical Instrumentation*, *2*, 1340004.

[117] ten Brummelaar, T. A., et al. (2005). First Results from the CHARA Array. II. A Description of the Instrument. *ApJ*, *628*, 453–465.

[118] Valenti, J. A., & Fischer, D. A. (2005). Spectroscopic properties of cool stars (SPOCS). i. 1040 f, g, and k dwarfs from keck, lick, and AAT planet search programs. *The Astrophysical Journal Supplement Series*, *159*(1), 141–166.
URL `https://doi.org/10.1086/430500`

[119] van Belle, G. T., Ciardi, D. R., & Boden, A. F. (2007). Measurement of the Surface Gravity of η Bootis. *ApJ*, *657*, 1058–1063.

[120] van Belle, G. T., & van Belle, G. (2005). Establishing Visible Interferometer System Responses: Resolved and Unresolved Calibrators. *PASP*, *117*(837), 1263–1270.

[121] van Grootel, V., et al. (2014). Transit confirmation and improved stellar and planet parameters for the super-earth hd97658b and its host star. *The Astrophysical Journal*, *786*(1), 2.
URL `http://stacks.iop.org/0004-637X/786/i=1/a=2`

[122] van Leeuwen, F. (2007). Validation of the new Hipparcos reduction. *A&A*, *474*, 653–664.

[123] von Braun, K., & Boyajian, T. (2017). *Extrasolar Planets and Their Host Stars*. Springer.

[124] von Braun, K., et al. (2011). 55 Cancri: Stellar Astrophysical Parameters, a Planet in the Habitable Zone, and Implications for the Radius of a Transiting Super-Earth. *ApJ*, *740*(1), 49.

[125] von Braun, K., et al. (2012). The GJ 436 System: Directly Determined Astrophysical Parameters of an M Dwarf and Implications for the Transiting Hot Neptune. *ApJ*, *753*(2), 171.

[126] von Braun, K., et al. (2014). Stellar diameters and temperatures - V. 11 newly characterized exoplanet host stars. *MNRAS*, *438*(3), 2413–2425.

[127] Weiss, A., & Schlattl, H. (2008). GARSTEC -the Garching Stellar Evolution Code. The direct descendant of the legendary Kippenhahn code. *Ap&SS*, *316*, 99–106.

[128] Wesselink, A. J. (1969). Surface brightnesses in the U, B, V system with applications of M_v and dimensions of stars. *MNRAS*, *144*, 297.

[129] Wright, E. L., et al. (2010). The Wide-field Infrared Survey Explorer (WISE): Mission Description and Initial On-orbit Performance. *AJ*, *140*, 1868–1881.

Vita

Tyler Ellis burst forth into this world in the beautiful town of Spokane, Washington. In his youth, Tyler enjoyed exploring the downtown of the city, riding the Looff Carousel and feeding the Garbage Goat in Riverfront Park. Tyler participated in a dual enrollment program and earned his Associate of Arts degree at the Spokane Falls Community College while he finished secondary school.

Tyler moved to Laramie, Wyoming to attend the University of Wyoming to study astronomy and physics under the tutelage of Michael Brotherton. There Tyler found a great appreciation for science communication and outreach. Tyler helped run dozens of telescope viewings and presented at the Harry C Vaughan planetarium.

After the completion of his dual Bachelor of Science degrees in Physics and Astronomy, Tyler spent a year working with Hannah Jang-Condell as a community observer for the Kilodegree Extremely Little Telescope project. Tyler assisted then-graduate student David Kasper with the remote enabling and automation of the Red Buttes Observatory while conducting exoplanet transit observations.

Tyler then moved to Baton Rouge, Louisiana to complete Doctorate of Philosophy in physics at the Louisiana State University. Tyler first studied the Star Doing a Weird Thing KIC 8462852 with Tabetha (Tabby) Boyajian, whom he had met through Hannah. Tyler and Tabby then carried out the LIGERS surver of M dwarfs. Tabby helped Tyler maintain a work life balance throughout his studies, encouraging him to pursue hobbies like baking and coffee roasting. During his time in Baton Rouge, Tyler met the most wonderful dog, Schooner, and has spent much time fixing all of the windowsills and door frames she has chewed up. After graduation Tyler seeks to apply his polished problem solving and research skills in the fields of machine learning and data science.